2019

AC/DC differential bridge based solution-electrode interfacial capacitance biosensor, for field-deployable real-time and low-cost detection of MCLR in drinking water.

Sara Neshani
Iowa State University

AC/DC differential bridge based solution-electrode interfacial capacitance biosensor, for field-deployable real-time and low-cost detection of MCLR in drinking water

by

Sara Neshani

A dissertation submitted to the graduate faculty

in partial fulfillment of the requirements for the degree of

DOCTOR OF PHILOSOPHY

Major: Electrical Engineering (Very Large Scale Integration)

Program of Study Committee:
Nathan M. Neihart, Major Professor
Degang Chen
Randall L. Geiger
Liang Dong
Meng Lu

The student author, whose presentation of the scholarship herein was approved by the program of study committee, is solely responsible for the content of this dissertation. The Graduate College will ensure this dissertation is globally accessible and will not permit alterations after a degree is conferred.

Iowa State University

Ames, Iowa

2019

DEDICATION

Dedicated to my lovely and caring parents, Mohammad and Sima, this dedication is not comparable to all the effort they have gone through and the unconditional love and support they gave to their children. Also to my sister Sonay and brother Roozbeh, remembering all joyful memories we made together through years. To my lifetime best friend and awesome husband, Kasra, I always feel lucky to have him by my side. To my dearest sweetness Kaisan Pasha, my adorable son, I hope this brings a smile on his lovely face when he reads these lines in the future.

TABLE OF CONTENTS

Page

ACKNOWLEDGMENTS

My PhD journey at Iowa State University, was full of best memories, priceless experience and learning that totally turned me into another person. First and foremost, I would like to thank my wonderful adviser Dr. Neihart, he is a perfect teacher not only in technical courses but also life lessons. I specifically thank him to help me understand what the word "precise" actually means, and how technical writing should be done. All the work written in this dissertation would have not been presented here without his continuous advice and technical discussions. I also give my regards to Dr. Neihart's kind family for making our group gatherings so memorable. I want to sincerely thank Dr. Chen, for all very useful discussions about this project with him. His deep and very wide knowledge of technical matters and very smart ideas have always shed a light in my research path. I have learned a lot from him, and cannot thank for all these using simple words.

I had great time doing research and performing experiments, in Coover 1045, interacting closely with Dr. Dong group. I want to thank Dr. Dong not just as my committee member, but for his friendly behavior. Watching his very organized research attitude and active atmosphere he created in his group is a great inspiration for me. As a great professor I give many thanks to Dr. Lu, it was valuable opportunity for me to take his biosensors course and learn most of sensing fundamentals that gave me better insight for my own research. I am very grateful about the precious comments on my work at my preliminary exam from Dr. Geiger, the points he made helped the improvement of our work. I sincerely thank Dr. Huang for accepting to be on my committee for the final exam.

I have had many discussions on my research with Dr. Azahar Ali, and he helped me a lot with developing new surface chemistry, I want to thank him for his time and

efforts. Whenever, I needed a component for my tests or practical advice for the implementations, Lee Harker from electronics and technology group at ECE, helped me with great patience, I want to thank him for the time he spent solving those issues.

I have met and worked with many great friends at the electrical engineering department, Yifei Li, Huanhuan Zhang, Byron Montgomery, Scott Melvin, Jayaprakash Selvaraj, Aditya Suresh and Subhanwitt Roy are my dear friends and colleagues at wireless systems lab, I wish all of them the greatest success. The office, group gathering and conference travel memories are just some of the precious experiences I had with them.

Again and once again I want to thank my family, who gave me the courage and support to build a future and receive quality education far from home. I miss them every second but carry them in my heart everywhere. My darling husband Kasra and sweet Kaisan Pasha I want to tell you two treasures of my life, how I appreciate all your emotional support and going through ups and downs of my graduate life side by my side.

ABSTRACT

Microcystin-LR (MCLR, one of the most toxic and commonly found products of cyanobacteria in freshwater resources, threatens human health and the livestock. WHO has set a standard limit of 1 $\mu g/l$ for the concentration of MCLR in drinking water. The lab-based, specialized water quality monitoring tests for this purpose are not only expensive but also slow and require sample preparation and transportation from distant sites. Therefore, there is a need for a handheld, field-deployable and low-cost biosensor to make frequent water quality monitoring easier.

Many field-deployable biosensors with applications in environmental monitoring and healthcare where concentrations of interest are on the order of $\mu g/l$ and fewer face challenges in achieving high dynamic range and lower detection resolution due to the resultant small fractional change in the transducer characteristics. Additionally, non-faradaic label-free biosensors for MCLR type applications face difficulty in real-time data analysis due to signal drift, non-specific binding of non-target particles and last but not least noise coming from both transducer and readout electronics.

This dissertation is mainly focused on utilizing electronic circuit methods to fill the gap of reading small responses from the bio-transducer with sufficient accuracy and sensitivity. Differential bridge based transduction as sensitivity booster and careful design of amplification unit and real-time signal processing capable of extracting signal information buried in noise are part of the presented work that achieves 8-bit resolution within a 1% full-scale transducer fractional capacitive change.

CHAPTER 1. INTRODUCTION

1.1 Background

Cyanobacteria harmful algal blooms, Fig. 1.1(a), (CyHABs) and their production of numerous potent toxins (i.e., cyanotoxins) threaten global freshwater supplies [2]. Toxic CyHABs have been reported from 57 countries around the world and at least 27 states in the United States [3]. Microcystin-LR (MCLR), Fig. 1.1(b), one of the most toxic and commonly found products of cyanobacteria has been reported as the cause of several incidents of wild and domestic animal poisonings, as well as human injury and deaths. The liver is the primary organ affected by MCLR, but it can also affect the kidneys, colon and neural system [5]. Besides, the accumulation of cyanotoxin variants in the food chain (e.g., lettuce, catfish, milk) is one other long term harmful threat for human health [6]. These harmful toxins are not removed from the drinking water with the current common water refining methods, in light of this, the World Health Organization (WHO) has set a standard limit of $1\ \mu g/l$ for the concentration of MCLR in drinking water [7].

Many states have implemented freshwater HAB monitoring programs, but current water-quality monitoring efforts often require someone to visit each body of water and take physical samples which are then transported back to a laboratory for analysis by either enzyme-linked immunosorbent assay (ELISA) [8] and/or liquid chromatography tandem quadrupole mass spectrometry (LC-MS/MS) [9]. These tests are expensive, ranging from $30-$80 per sample. Moreover, these costs do not include sample collection and preparation, which can dramatically increase the total cost, especially when sampling locations are remote or separated by large distances. Also, these tests require specialized, often expensive equipment and advanced training to perform, making it difficult for non-technical people, such as farmers, to

monitor water bodies (e.g., farm ponds used to water livestock) that may not be otherwise monitored.

For water quality monitoring applications involving toxins like MCLR, the target concentrations are generally very small (less than 1 $\mu g/l$) on the other hand, these applications require frequent and regular daily or weekly monitoring. The general principle for detecting particles like proteins (toxins such as MCLR family are generally considered as protein-like species) or DNA is affinity-based sensing where a capturing antibody is immobilized on a metallic surface (usually gold) to capture the specific analyte in the sample.

Although various biosensing techniques like surface plasmon resonance [10] or quartz crystal microbalance [11] can be employed for affinity probe-target binding, electrochemical biosensors which utilize an electrical signal (voltage or current) to excite the interface are considered superior options for making in-situ tests with reasonable accuracy and lower cost. These systems consist of a bio-functionalized surface with the specific antibody that binds to the target bio-molecule like a toxin in the sample, a transduction unit that translates the chemical phenomena of binding to a quantifiable electrical signal and a read-out interface unit

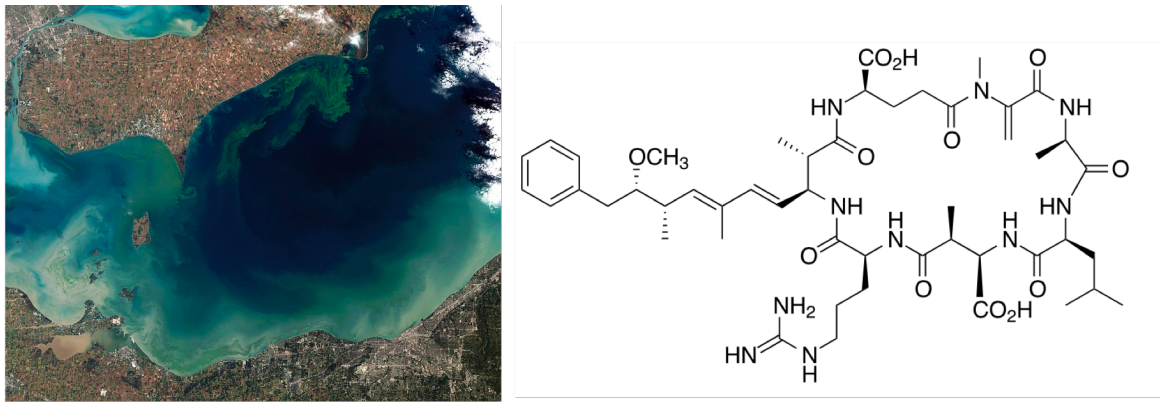

(a) **(b)**

Fig. 1.1 (a) Algal blooms at lake Erie, the growth of Microcystin, October, 2011 [1], (b) MCLR chemical structure [4]

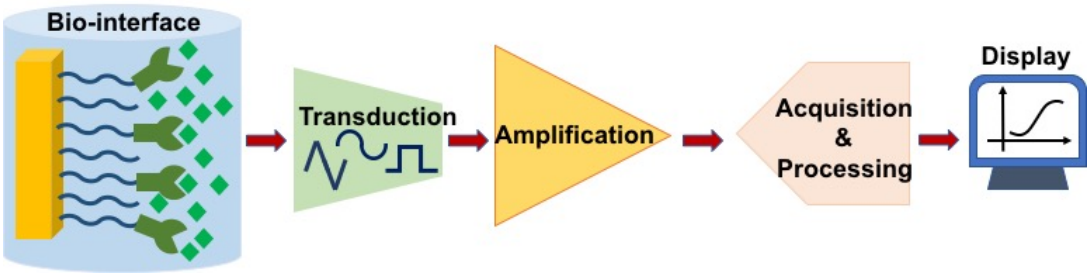

Fig. 1.2 General biosensor system for real-time in-situ measurements (the sample interface is an example of toxin-antibody detection)

that amplifies the translated response and acquires the final data for processing. Fig. 1.2 shows the general schematic for an electrochemical biosensor system. Currently, most of the research on this subject is aiming to develop sensitive label-free test methods with decreased cost per test by optimizing the transducers type, shape, size, and the bio-functional layer immobilization process [12–15]. Moreover, these optimized transducers and functionalization methods, if employed within a handheld simple to operate device, can facilitate frequent monitoring in the field, which, in turn, dramatically reduces the time and cost required per test [16]. Thus, research on the development of electronic handheld real-time and field-deployable biosensor systems for water quality monitoring to interface with the electrochemical transducers is an interesting research topic that addresses an ongoing real-life issue and serves the wellbeing of humans and livestock. However, challenges are associated with the design of such real-time biosensing systems, as very small target concentrations result in weak response signals. This dissertation is mainly focused on utilizing electronic circuit methods to fill the gap of reading small responses from the bio transducer with sufficient accuracy and sensitivity for the specific case of monitoring the MCLR concentration in water resources.

1.2 Outline

The very small full-scale fractional changes with binding even with optimized transducers for MCLR necessitates the development of sensitive read-out interfaces that can

overcome the design challenges and achieve high dynamic range and low detection limit for a field-deployment. This dissertation is approaching this problem step by step to find the most suitable circuit method for the characterization of MCLR concentrations in the field.

Chapter 2 reviews some recent MCLR biosensors and the detection methods. Affinity-based sensing methods provide a faster and cheaper solution; therefore, the most popular measurement methods for affinity-based transducers are studied, and single frequency impedance (capacitive) sensing is utilized for the biosensor design, and a high-level system structure is given based on the explained design challenges.

Chapter 3 explains the capacitive transducer and principle of solution-electrode interfacial capacitance. The electrode functionalization method and characterization that helps to pick the operation frequency in the presented work are also introduced in Chapter 3.

In Chapter 4, we explore the best bridge model that is suitable for non-faradaic capacitive measurement as well as the excitation and bias requirements, ways to alleviate drift, nonspecific binding, noise, and other potential interferences. Utilizing a bridge with an optimized structure for interfacial capacitance measurement, in this way, acts like a secondary transducer that improves sensitivity and overall dynamic range of the biosensor. It is still very important to design a proper readout interface for the amplification of the differential response at the bridge output the details for the design of amplification unit compatible with differential bridge interface is given in Chapter 5. For real-time implementation, it is also necessary to develop a fast and low-cost data acquisition and signal processing method. The amplification, data acquisition, and signal processing unit are designed with the total expected full-scale fractional capacitance change and detection resolution (minimum detectable capacitive change at the transducer corresponding to the minimum detectable MCLR concentration) requirements.

The detailed approach and design trade-offs for the real-time data acquisition and processing unit are presented in Chapters 6. These design details can also be used as a guideline for designing any biosensor amplification and real-time signal acquisition unit. The experimental setup and actual capacitance measurements with gold bio-functionalized electrodes is demonstrated in Chapter 7 as proof of concept.

CHAPTER 2. MEASUREMENT APPROACHES

2.1 Introduction

As mentioned in the previous chapter, detecting the safe limit of MCLR is crucial specifically to prevent direct exposure of humans and animals to highly contaminated water resources. A variety of lab-based methods form the expensive and accurate LC/MS [17-18] to the sensitive ELISA [8], [19] have been used for detecting MCLR and reaching detection levels as low as ng/l. Direct affinity-based immunosensors, however, are superior low-cost and label-free alternatives for the expensive lab-based methods that localize the binding events on a solution-electrode interface. Fig. 2.1 shows the general label-free detection at the interface of an antibody functionalized metal electrode with a solution containing the related analyte. The insulation layer on the electrode surface is to prevent reaction with other particles in the solution and will be further discussed in the capacitive transducer section in Chapter 3. With the label-free immunosensor the goal is to detect a change in the interface characteristic by binding. This chapter will elaborate more on some recent affinity-based MCLR biosensors that offer cheaper and faster detection suitable for field deployment. By discussing the pros and cons of these works, the impedance biosensor concept and measurement techniques is picked as the desired

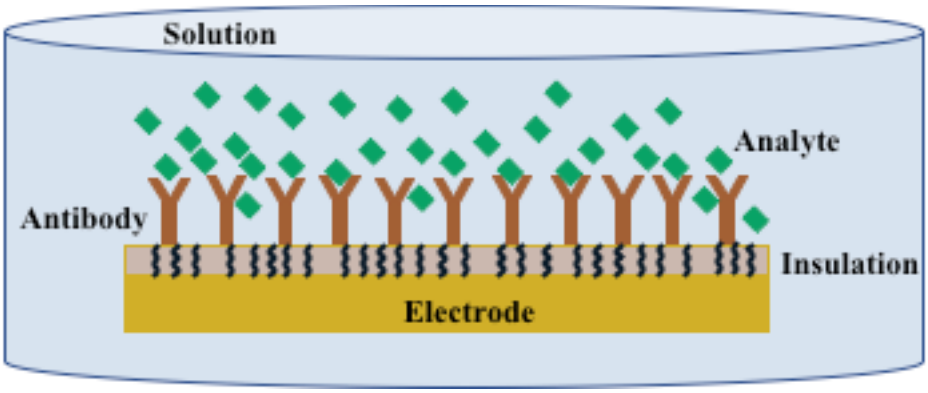

Fig. 2.1 The principle of affinity-based label-free immunosensors, binding events occur at the solution and functionalized electrode interface

solution for the MCLR detection, by exploring the corresponding design challenges, finally, our general proposed idea for the development of handheld MCLR biosensor is given in this chapter.

2.2 Recent Affinity-Based MCLR Biosensors

Research on MCLR detection in recent years has been developed in a direction to make the monitoring process faster, easier, and cheaper. In 2013, Shi et al. developed an automated online optical biosensor for real-time monitoring of MCLR risk in drinking water [20]. The system utilized an indirect competitive detection method, shown in Fig. 2.2, in which various samples containing MCLR are premixed with a certain concentration of fluorescence-labeled anti-MCLR-mAb. Next, this mixture flows through a chip with an immobilized MCLR capture probe. The remaining labeled antibody now binds to the immobilized MCLR; after washing the surface with buffer, a laser beam is turned on to produce the response fluorescence signal incorporating the remaining labeled antibody that is binding to the capture probes. With this method, samples with higher toxin concentration will produce a lower fluorescence signal.

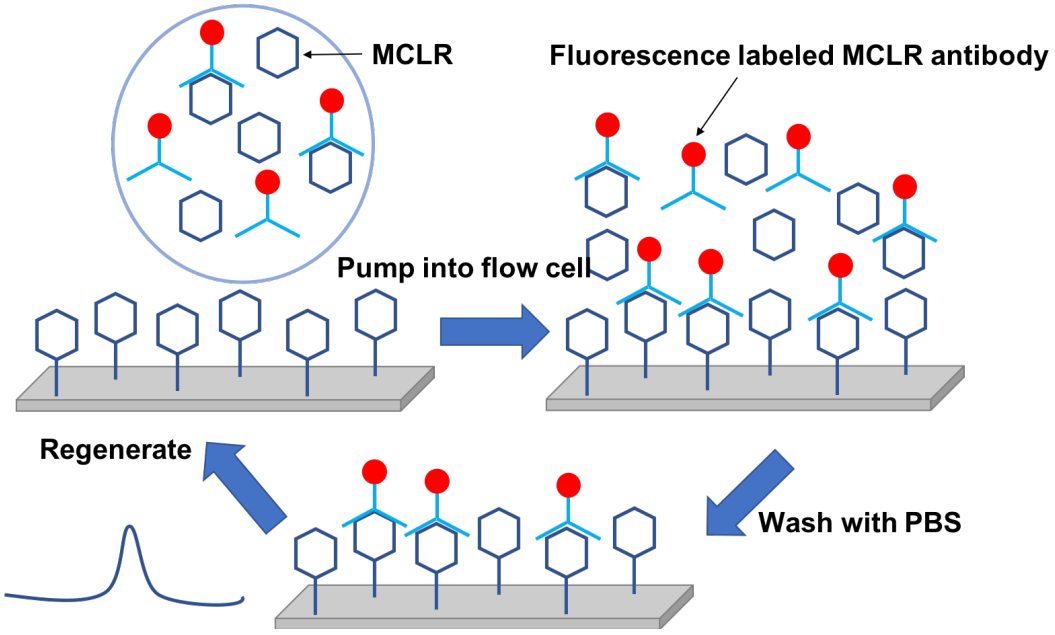

Fig. 2.2 Indirect competitive detection method using fluorescence label [20] (recreated)

The quantified detection ranges for this biosensor, are $0.2\,\mu g/l$ to $4\ \mu g/l$. Although the proposed biosensor can be used in the field, the overall system is not cost-effective. For point-of-care applications, in addition to the smaller size and lower cost, a simple structure with no sample preparation is desirable. Not only do labels complicate the procedure, but it has also been demonstrated that labels alter the binding characteristics of biomolecules, which is a major concern, specifically for protein family [21].

For the case of label-free capacitive transduction, Loyprasert et al. developed a label-free capacitive immunosensor with sensitivity for MCLR concentrations ranging from $10^{-5}\,\mu g/l$ to $10^{0}\ \mu g/l$ [12]. The detection principle is based on immobilization of anti-MCLR-mAb antibody on the surface of gold electrodes with silver nanoparticles added and coated by self-assembled thiourea monolayers. The modification of the gold surface and the capacitances representing the chemical layers on the electrode are shown in Fig. 2.3. The surface of the electrode being blocked for charge transfer, and the overall electrode-solution interface is modeled like a capacitance in series with a solution resistance. Utilizing a Potentiostat lab

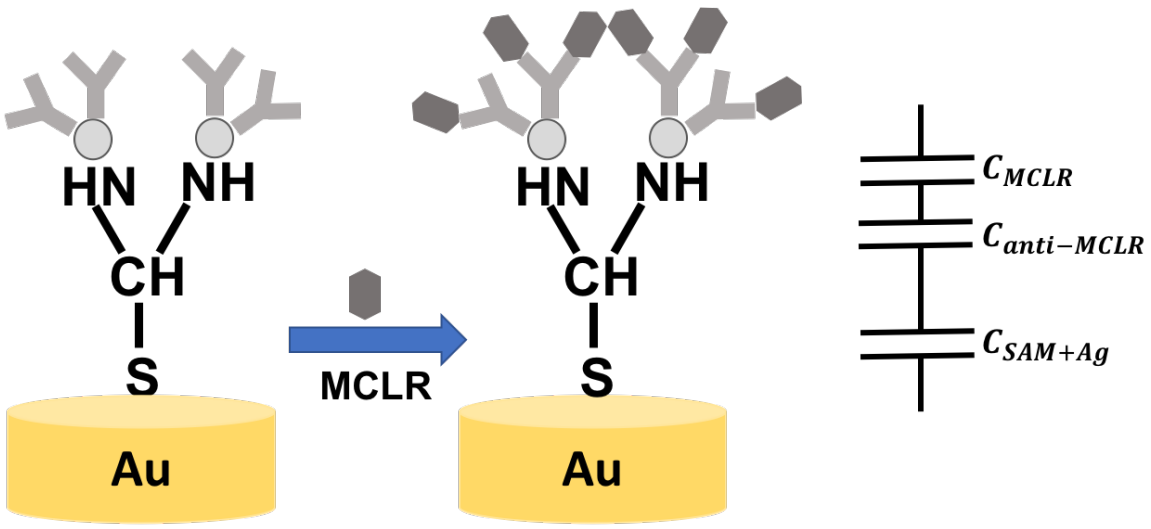

Fig. 2.3 Capacitive immunosensor developed by modifying the surface of gold electrode with self-assembled monolayer, and MCLR antibody, each chemical layer at the gold surface is represented by a capacitance in series with other layers [12] (recreated)

instrument, the interface capacitance and solution resistance are extracted by a rather complicated fitting algorithm. The capacitance decrease is measured with a flow injection setup in [12] after the response signal reaches a stable state with each MCLR sample injection, the electrode is refreshed chemically, and the next MCLR sample is injected. The obtained capacitance change is effectively linear with the log-scale MCLR concentration utilizing transducer with and without nano-gold particles. Although, this approach is label-free and less costly while maintaining high sensitivity but the measurement approach is not simple for field-deployment.

Another label-free optimized transduction approach that utilizes gold electrode modified with polytyramine, gold nanoparticles for easy MCLR detection is reported in [22]. The designed transducer reaches 0.01 pM MCLR concentration sensitivity at lower limit of detection (LoD). But the liquid chromatography coupled to MS/MS detection is employed in [22] for the measurement. This costly method requires lab-grade and complicated measurement tools and of course not suitable for real-time field deployment. Development of an easy to operate, low-cost, small size real-time field-deployable biosensor system for MCLR detection is therefore still an open problem for researchers.

2.3 Non-Faradaic Electrochemical Impedance Measurements

Electrical biosensors are generally categorized into three groups, amperometric, voltammetric and impedance biosensors [16, 21]. The amperometric and voltammetric sensing methods are merely DC excited and based on the response signal type that s measured the sensor is either amperometric or voltammetric [16]. The dynamic range and resolution of these sensors are limited by the capability of the instrumentation to measure tiny current or voltage levels occasionally in the presence of the transient ambient or electrode related drifts. Moreover, these

types of measurements require the addition of electroactive species (redox) to the solution which is an extra step that might also affect the natural binding efficiency [23]. Impedance biosensing, on the other hand, involves a small amplitude AC excitation often accompanied by a DC bias, where the ratio of the excitation voltage to the resultant current is measured. Impedance based biosensors provide an attractive solution to developing inexpensive, portable, and easy-to-use devices for monitoring cyanotoxins [16].

Impedance based biosensors translate an electrochemical change in the reactive characteristic of an electrode-solution interface into a measurable electric signal [21]. A primary design goal is to realize sensors that can achieve dynamic range and sensitivity that is comparable to traditional analytical methods. Electrochemical impedance spectroscopy (EIS) is a standard method, accomplished by exciting the transducer with a small AC voltage within a range of frequencies and study the resultant current magnitude and phase shift with and without target present, in this way the ratio of the voltage to current yields an impedance. By fitting a model to the impedance spectrum, the transducer interface characteristics can be interpreted as familiar electrical elements like capacitance and resistance. For real-time field deployable applications however, single-frequency excitation is generally utilized for lower cost and complexity [24], this method will be discussed in the following section.

Various measurement methods have been developed for label-free non-faradaic impedance characterization that is simpler for field-deployment without the need for a redox probe in the sample. These methods are also performed either with DC or AC excitation. The DC methods mainly characterize the time constant of the electrode-solution by charging the interfacial capacitance. AC methods characterize the interface impedance by exciting the interface with a

small AC signal over some range of frequencies. These techniques are explored in the following.

2.3.1 Step Measurement

Researchers utilize simple series *RC* model for non-faradaic impedance measurements, the ability of an interface at polarized electrode-solution interface to store charge resembles a capacitance, and the associated solution conductivity is represented by resistance in series [25-26]. The reason for this series *RC* modeling and general interface models are explained with more details in Chapter 3. The step method characterizes interfacial capacitance using DC measurements.

For this measurement setup, three types of electrodes are required: the working electrode (WE), that is coated with insulation and antibody and is generally an inert metal such as gold; a reference electrode (Ref), which is generally Ag/AgCl with a well-defined DC voltage; and a large platinum or gold counter electrode (CE) to collect the cell current. The counter electrode

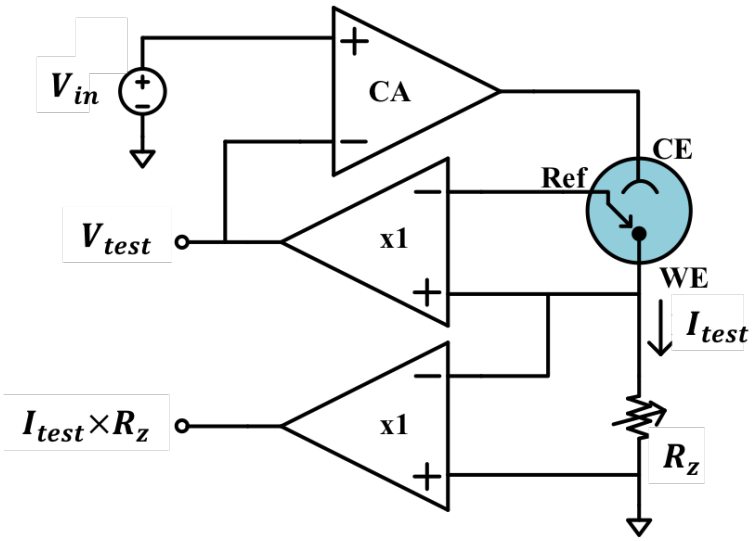

Fig. 2.4 Working principle of Potentiostat device, a control amplifier (CA) compares V_{in} and V_{test}, to have the voltage applied between refernce electrode (Ref) and working electrode (WE) equal to the desired voltage V_{in}. The flowing current (I_{test}) between WE and counter electrode (CE) is measured using a resistor R_z.

surface area is typically much larger than the working electrode. A 50 mV step voltage (V_{in}) is applied between the working and reference electrodes and the resulting current (I_{test}) is collected by the counter electrode. This principle is known as Potentiostat-type measurement [27] and is shown in Fig. 2.4. The control amplifier (CA) is utilized to maintain the voltage between the working and reference electrodes, V_{test}, equal to the applied signal V_{in} [27].

The electrochemical cell current is flowing between the counter and working electrodes, and the current-to-voltage conversion is carried out by the variable resistance, R_z. The interface capacitance, C_{int}, is charged by the application of the potential step with amplitude u, and the cell time-dependent current, $i_{test}(t)$, decays with time after the excitation. The relationship between the exponentially decaying cell current and C_{int} and solution resistance, R_{sol}, is:

$$i_{test}(t) = \frac{u}{R_{sol}} e^{(-t/R_{sol}C_{int})} \tag{2.1}$$

Equation (2.1) indicates that the natural logarithm of the cell current has a linear relationship with the surface capacitance. This parameter can be extracted from current data by the least-square fitting [26]. The quality of the acquired data in this method depends on the time constant of the cell, $R_{sol}C_{int}$, and very high sampling rates may be required to get sufficient samples before the current decays to zero.

In [28, 29], the step method is used for characterizing the capacitive transducer for glucose and Cholera toxin. Fig. 2.5 shows the experimental setup used in [28], which shows a flow injection and lab-grade Potenstiostat along with a high-speed data acquisition unit (Keithley 575) that is required to acquire the current at Potentiostat output with sufficient accuracy. This lab grade characterization with a very high sampling rate, small current at the output, and the required complicated fitting algorithm are not favorable for low cost and simple real-time implementation of data acquisition/processing of a field-deployable biosensor.

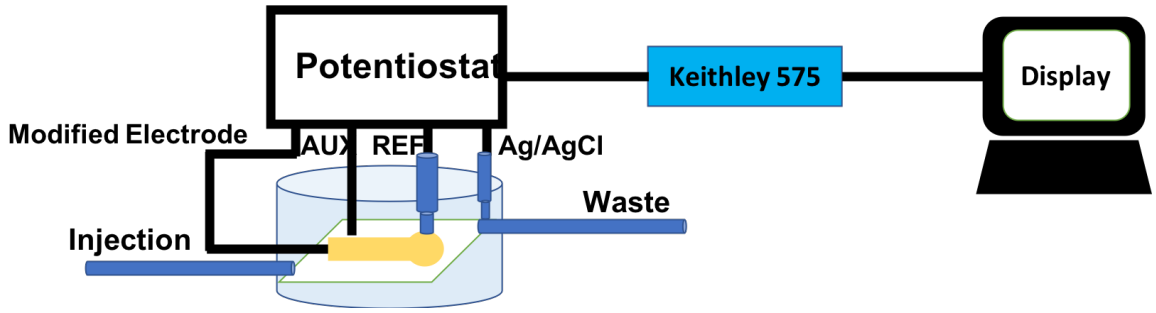

Fig. 2.5 Experimental setup for step measurement used in [28], other than the lab-grade instrument Potentiostat for cell excitation, the very fast data acquisition unit, Keithley 575 is also required to sample the decaying cell current with very high speed, the samples are stored in computer for the post-processing to extract the cell time constant.(recreated)

2.3.2 Electrochemical Impedance Spectroscopy (EIS)

Generally, EIS measurements include a sweep of frequency and obtain an impedance spectrum. A small AC signal is applied between the working and reference electrodes, and the resulting current is measured between the working and counter electrodes using the same setup shown in Fig. 2.4 [13, 30-32]. In this method, the interface models described in the previous section are used to fit the magnitude and phase of the measured impedance and to evaluate the change in the corresponding model element with binding.

As an example, EIS has been used in [13] for measuring the nano-interdigitated capacitive transducers on a polymer substrate. The interface impedance bode plots (magnitude and phase) are obtained at varying electrolyte solution concentrations, these curves are helpful to pick the suitable solution concentration and the frequency range where the interface capacitance in the model for interface, is dominant for the designed transducer. Although the frequency sweep in the EIS method is very useful for characterizing and fitting an interface model for different transducers, it is not efficient for fast real-time measurements. A popular sub-division of EIS measurements for the non-faradaic interface model is single frequency sine wave excitation method [21], which is quicker and not very complicated for real-time implementation.

2.3.3 Single-Frequency Sine Wave Excitation

A less cumbersome and low-cost method for non-faradaic, real-time interface capacitance measurement is single-frequency sine wave excitation. In addition to being faster, single-frequency AC excitation allows the transient response of the biosensor to be acquired, which can be used to monitor the binding phenomena and extract other useful information such as the association and dissociation coefficients [21, 24, 33-35]. The amplitude of the single-frequency sine wave excitation signal should be small (typically less than $50\ mV$), so as not to damage the recognition layer and avoid non-linear distortion due to any nonlinear current-voltage relationships [24]. For single frequency measurements, it is vital to pick the frequency of excitation within the range where C_{int} dominates the impedance spectrum. This frequency range depends on the geometry and makeup of the electrode and also coating layers but is typically less than $15\ kHz$ [21].

Fig. 2.6 shows a general block diagram of a portable single frequency capacitive biosensor. As shown in Fig. 2.6, a chemically functionalized metal (gold) electrode with redox reaction blocking coating and a highly specific antibody, is immersed in a solution containing the target analyte. Two electrodes are generally sufficient for this type of measurement, one as the working electrode, with the chemical functionalization, and the second as the counter electrode.

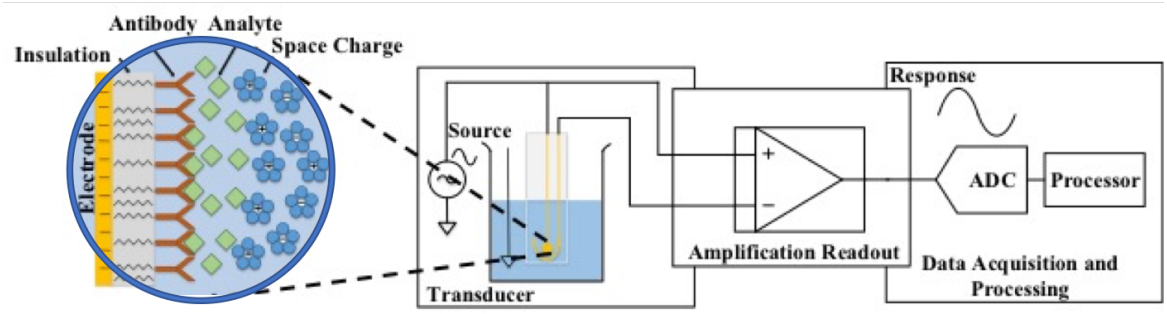

Fig. 2.6 General block diagram of a portable single frequency impedance biosensor, with real-time response amplification and digitization

The single-frequency excitation signal is applied between these two electrodes. The surface area of the electrodes and the frequency of excitation are chosen in such a way that interfacial capacitance at the working electrode in this path is dominant. An amplification unit in the read-out interface system is required immediately after transduction, as well as a proceeding data acquisition and processing unit for real-time operation.

Each segment of the general diagram in Fig. 2.6 can be implemented with various design approaches that are based on the required detection conditions. Although, multiple methods have been reported on the design of more sensitive affinity-based impedance transducers for MCLR, for sensitive, accurate and low-cost sensing of MCLR with single frequency excitation in real-time the proceeding blocks need careful design considering some main design challenges that will be discussed in the following.

2.4 System Overview and Block Diagram

As discussed in the previous section, Loyprasert et al. used the step method for measuring the performance of their transducer for MCLR, and they employed a benchtop lab-grade Potentiostat instrument for readout process. A closer look at their reported results reveals one significant challenge in developing a handheld device to replace their benchtop lab equipment. The baseline transducer capacitance before the toxin injection in [12] is 3,380 nF/cm^2, however, the total capacitance change reported for the entire practical range of concentrations is only about 30 nF/cm^2. This result means that the readout circuitry should be able to effectively detect even a less than 1% fractional change in the transducer capacitance. This challenge is associated not only with MCLR detection but also many biosensors with applications in environmental monitoring and healthcare where concentrations of interest are on the order of $\mu g/l$ and less.

This small fractional change at the same time brings about design challenges to obtain a high dynamic range and lower detection limit. Additionally, non-faradaic label-free biosensors face difficulty in real-time data analysis due to problems such as signal drift, non-specific binding of non-target particles, and noise coming from both transducer and readout electronics. Various electrochemical and circuit techniques can be utilized to reduce the effect of the abovementioned issues and achieve sufficient accuracy while maintaining low cost in point-of-care applications. For example, differential or dual-sensing (two sensors one with recognition element and one without or two electrochemical cells one with and one without analyte) has been introduced in the past to overcome the effect of non-specific binding and drifting response caused by that [21, 24, 36-37]. A chemical approach to alleviating the non-specific binding of proteins according to previously reported literature is bovine serum albumin (BSA) co-immobilized in the recognition layer [24]. DC bias additional to AC applied to the transducer is also said to be effective on reducing the drifting both by establishing a stable interfacial capacitance and at the same time by controlling the leakage oxidation/reduction reaction currents [38-42]. To overcome the challenge electronically, employing differential circuit topologies and modern CMOS technology, reduces the effect of common-mode interferences and noise.

Fig. 2.7 demonstrates the general system-level solution for read-out implementation for a non-faradaic MCLR impedance biosensor proposed in this dissertation. Two primary antibody

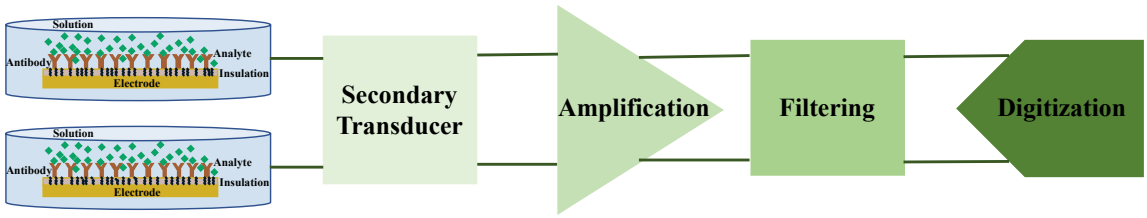

Fig. 2.7 Proposed fully differential structure for a simple impedance MCLR biosensor, the process of designing each block will be given in the following chapters

functionalized transducers such as the ones in Fig. 2.1 are employed in a differential scheme, and a secondary transducer boosts the sensitivity utilizing the differential response from the primary transducers. Having said that, the target concentrations are very small; an amplification unit is added in the fully differential path to elevate response amplitude to quantifiable levels. Employing the single frequency AC excitation gives the option to use a narrow band pass filter to get rid of the out of band noise. A digitization and processing unit proceeds the filtering so that the final detection result can be obtained directly in the field.

Each block in Fig. 2.7 requires specific considerations that are application-driven, and the optimum design for each block is made regarding the target resolution and potential system non-idealities. The following chapters describe the criteria for picking the design parameters and structures of each block, from the transducer type and functionalization method, excitation signals, frequency of operation, secondary transduction circuit to the amplification gain, and common-mode rejection, filtering bandwidth and digitization setup. Many essential design details are given to achieve a specified target dynamic range for a handheld simple to operate biosensor with a very small fractional change in the transducer characteristic upon detection.

2.5 Conclusions

The affinity based impedance biosensor and single-frequency sine wave excitation method, are promising solutions to overcome the challenges of designing a real-time cost-effective and field-deployable MCLR biosensor. The optimized transducers from the literature that are characterized by lab instruments, provide useful information about the design goals and parameters to consider, like the total fractional change the transducer characteristics and practically achievable detection resolution. To design a biosensor prototype that gets similar results in accuracy and sensitivity compared to the recent MCLR literature we the structure

shown in Fig. 2.7. The details regarding the design of each block in Fig 2.7 are given in following chapters. The primary transducers design and the chemical functionalization are explained in Chapter 3. Besides, the important system design factors like the electrode-solution interface electrical model and the specific operation frequency for single-frequency excitation are explored.

CHAPTER 3. ELECTRODE AND DOUBLE LAYER CAPACITANCE

3.1 Introduction

Capacitive transduction is an affinity impedance biosensor and is based on the double layer capacitance theory. This theory states that when a metal polarized electrode is immersed in an electrolyte solution, as shown in Fig. 3.1(a), the charged particles (e.g., solvated ions along with solvent molecules) become oriented towards and adsorbed onto the electrode surface by electrostatic and thermal forces that counterbalance the charge on the electrode surface. However, there is a distance of closest approach to the electrode surface shown in Fig. 3.1(a) with double arrows, called the Stern layer which is roughly as wide as the radius of an ion plus the diameter of the solvent molecule [21, 24-25]. The distribution of non-adsorbed solvated ions from the Stern layer in a 3-dimensional space, toward the bulk of the solution, forms a so-called diffuse layer that can be seen in Fig. 3.1(a). The thickness of, and the total charge contained within, the diffuse layer is dependent on the ionic strength of the solution and the excitation potential of the electrode. A higher ionic concentration will lead to a more compact diffuse layer, and a higher excitation potential leads to shorter diffuse distance.

If the polarized metal electrode is separated from the diffuse layer by a charge-free region, it can be modeled by two serial capacitances, C_{Stern} and C_{Diff}, which results from the Stern layer and the diffuse layer, respectively, as shown in Fig. 3.1(a). The value of C_{Stern}, is dependent on the dielectric properties of the solution and thickness of the Stern layer, and is therefore constant with respect to electrode DC bias and background concentration. The value of C_{Diff}, on the other hand, is dependent on the background concentration and the potential at the Stern boundary with respect to the bulk solution potential [25].

Immobilization of antibody on the insulation coated electrode surface (to mitigate chemical redox reactions) adds series capacitances, $C_{Antibody}$ and C_{Ins}, in series with the Stern layer capacitance, shown in Fig. 3.1(b). Later binding of the analyte to the immobilized antibody, alters the value of $C_{Antibody}$, and pushes the Stern layer further toward the bulk solution, if the makeup of the electrode is such that $C_{Antibody}$, is the smallest, and therefore dominant, interfacial capacitance, the transducer becomes sensitive to binding, shown in Fig. 3.1(c). Binding of the antibody with the analyte, in this case, will appear as a change in the interfacial capacitance that is the primary mechanism of detection in capacitive affinity biosensors [25].

3.2 The electrical Model of The Interface

The theory of double-layer capacitance is utilized for affinity-based impedance biosensor measurements within two categories; Faradaic and non-Faradaic [21]. Faradaic impedance biosensors are based on charge transfer from, and to, the electrode, i.e. redox

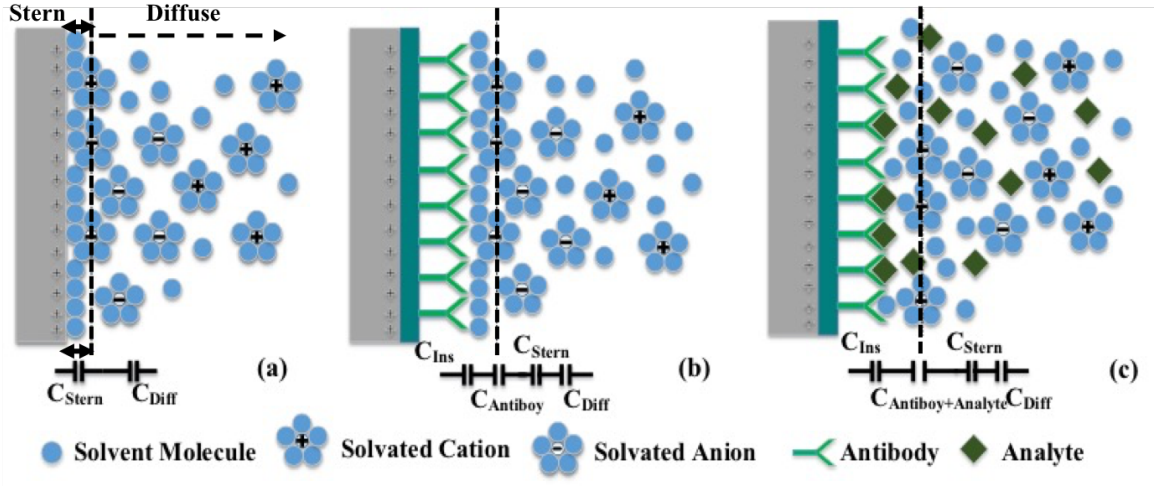

Fig. 3.1 (a) Double layer model at charged bare electrode-solution interface,(b) the coated electrode with antibody and solution interface with the associated capacitances model, (c) relocation of stern and diffuse layers and modified interface capacitance e with antibody-analyte binding

reactions between the solution and working electrode surface. In this process, a metal working electrode (not covered with insulation) coated with antibody is immersed into an electrolyte solution containing electroactive redox species and analyte, and the electrode is then excited with both AC and DC voltages. A reference electrode with a well-defined DC voltage is also immersed into the solution so that by adjusting the DC bias on the metal working electrode, with respect to the reference electrode, sufficient energy is provided for oxidation and reduction reactions to take place at the working electrode surface.

To account for the interactions of the redox probe with the working electrode in a Faradaic process, the interface is modeled as shown in Fig. 3.2 (a). The R_{ct}, represents the charge transfer resistance at the interface. Z_W, is an impedance accounting for the finite diffusivity of redox in the solution, C_{int}, is the equivalent interface capacitance (including C_{Stern}, C_{Diff} and $C_{antibody}$) and R_{sol}, represents the ionic strength of the solution. As analyte or target molecules bind to the immobilized antibody, the chances of the redox probe reacting with the working electrode surface are hindered. As a result, the charge transfer resistance, R_{ct}, increases while C_{int}, decreases. The higher the concentration of the analyte, the larger the increase in R_{ct}. Z_W, is an impedance with a constant 45° phase shift across all frequencies, the absolute value of this impedance is, however, proportional to the reciprocal of the square root of frequency as well as a coefficient that depends on the concentration of redox species and their diffusivity in the solution [25].

The component, C_{int} in Fig. 3.2(a), is used for fitting the impedance spectrum, is not modeled as a pure capacitance. Chemical inhomogeneities and adsorption of ions are the major causes of the interface capacitance often having a phase shift of less than 90° [21]. This effect is modeled with a "constant phase element" instead of a pure capacitance, the impedance of the

constant phase element is formulated as $1/(j\omega C_{int})^m$, ω, is the angular frequency in rad/sec and m is an ideality factor ranging between 0 and 1 [25].

Faradaic biosensors, although reported to produce stronger signals upon detection [24], are less favorable for real-time point of care applications first because they require the addition of redox to the sample, and second, some reports compare Faradaic results to ELISA sensing methods, and show that the use of redox couple in the solution affects the sensing layer and decreases the binding yield [23].

For the non-faradaic capacitive method, the working electrode and solution interface mainly behaves like a capacitance. The working electrode surface is blocked with a thin insulative layer to prevent any faradaic reaction with the electrode before the antibody is immobilized, the non-faradaic interface model is shown in Fig. 3.2(b). By blocking the electrode surface and absence of redox couple, the interface for the non-faradaic capacitive transducer is simply modeled as a series of surface capacitance, C_{int}, and solution resistance R_{sol}. The resistance, R_{leak}, is indicative of the surface block layer resistance and typically has a very high value on the order

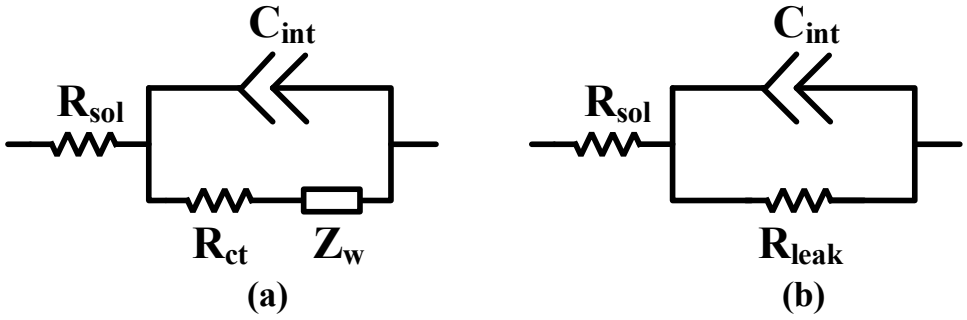

Fig. 3.2 (a) Faradaic interface model; the R_{ct} represents the charge transfer resistance at the interface. Z_W is an impedance accounting for the finite diffusivity of redox in the solution, C_{int} is the equivalent interface capacitance (including C_{Stern}, C_{Diff} and $C_{antibody}$) and R_{sol} represents the ionic strength of the solution , (b) non-faradaic capacitive transducer is simply modeled as series of surface capacitance, C_{int}, and solution resistance R_{sol}, the resistance, R_{leak}, is indicative of the surface block layer resistance

of $G\Omega$ [21, 24]. The binding recognition element in the model, in this case, is mainly the C_{int}, that decreases with binding of analyte to antibody, the electrodes that are chemically modified for non-faradaic measurements, are generally referred to as capacitive transducers.

3.3 Description of the Electrode

The discussed non-faradaic method with capacitive transducers is employed for MCLR biosensor in this work. Patterned gold electrodes, shown in Fig. 3.3(a), are purchased from Pine research instrumentation for experimental validation. Each sensor chip contains a circular working gold electrode with 2 mm diameter, a large gold counter electrode, and a reference electrode. The gold metal is widely used for capacitive transducers because it is an inert metal, and various surface chemistries can be applied to the gold surface for antibody or other probe immobilization [39]. The working electrode and the counter electrode are used in the experimental process, but the on-chip reference electrode is left floating, and an external Ag/AgCl reference electrode is used.

The chemical surface functionalization is carried out at the Iowa state university chemistry department Fig. 3.3(b) shows the chemical functionalization steps of the working electrode.

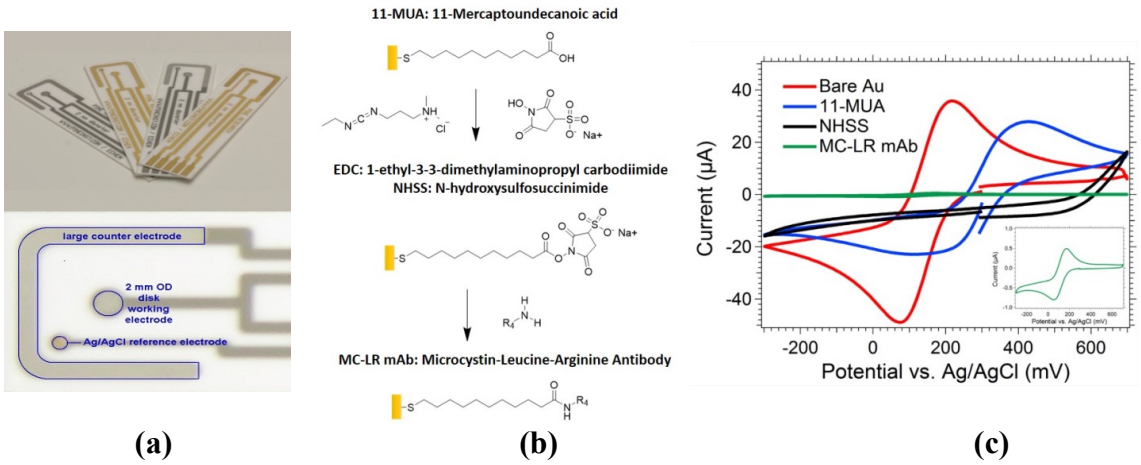

(a) **(b)** **(c)**

Fig. 3.3 (a) Gold patterned electrodes, (b) Functionalization steps, (c) Cyclic voltammetry test after each functionalization step

The first chemical layer on the gold surface is made by incubating the electrode overnight in 11-MUA (11- Mercaptoundecanoic acid) solution that forms the self-assembled monolayer (SAM) a compact layer blocking the gold surface from charge transfer reactions with the outer solution. Next, the EDC-NHHS (EDC: 1-ethyl-3-[3-dimethylaminopropyl]carbodiimide, NHHS: N-hydroxysuccinimide) is applied as a linker between 11-MUA thiol groups to covalently bound the immobilized MCLR antibody (MC-LR mAb) to the SAM layer at the final step. At later stages of the project, the first step of the electrode functionalization is modified, and the 11-MUA: 11- Mercaptoundecanoic acid is replaced with Thioglycolic acid (TGA, HS–CH2–COOH) for better stability and less drift [41]. Another chemical step is also added after the antibody immobilization, which is immersing the functional transducer for an hour in the BSA solution to reduce the potential non-specific binding effect during the actual experiment.

One crucial design specification to be verified for the transducer is the quality of the surface blocking layer and the least leakage which means a very high leakage resistance to avoid faradaic currents and drift. This can be validated using a cyclic voltammetry (CV) test by immersing the functionalized transducer in the buffer solution (Phosphate Buffer Saline (PBS)) containing the redox probe. For the CV test, a cyclic voltage ramp is applied between working and reference electrodes, using the Potentiostat device and with the step measurement method setup, and cell current is measured between working and counter electrodes. The

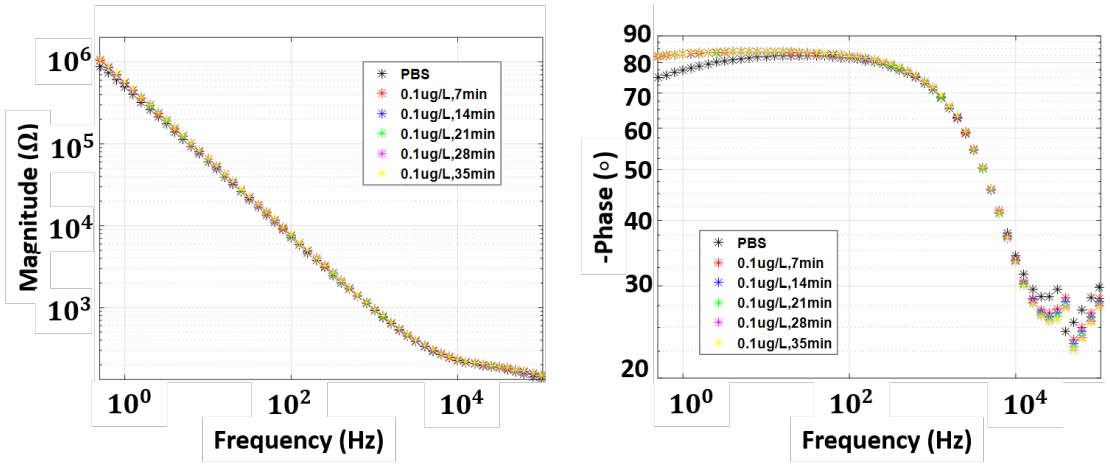

(a) **(b)**

Fig. 3.4 (a) Magnitude and (b) negative phase spectrum for buffer (PBS) and 0. 1µg/l MCLR sample concentration obtained with EIS sweep taken every 7 minutes

measured current plotted against the applied voltage at each functionalization step is shown in Fig. 3.3(c). The peaking in the current decreases at each stage, indicating a considerable interface leakage resistance ($M\Omega$) after the final step. The CV test is carried out once utilizing the lab grade Potentiostat to characterize the functional layer at the working electrode surface.

Single-frequency AC excitation impedance measurement method is the target of the design in this work; therefore, a proper operation frequency needs to be picked by

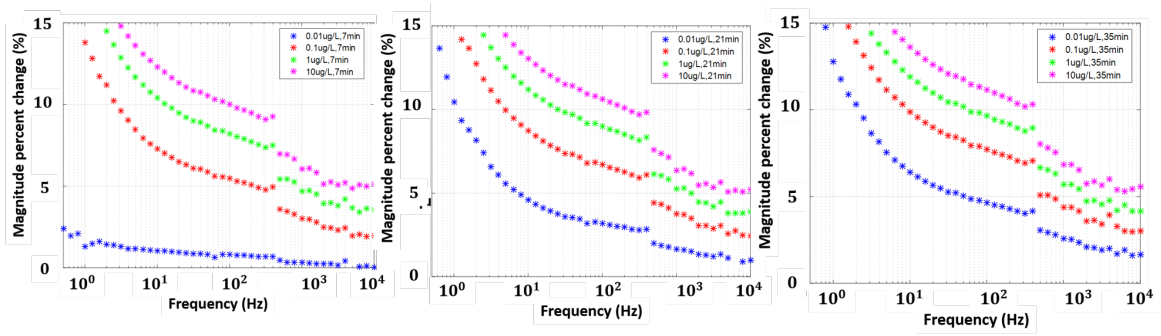

(a) **(b)** **(c)**

Fig. 3.5 Magnitude % change w.r.t buffer for 0. 01µg/l, 0. 1µg/l, 1µg/l and 10µg/l MCLR samples with EIS obtained at (a) 7, (b) 21 and (c) 35minutes

characterizing the functional electrode-solution interface impedance with EIS. A Potentiostat is used again for obtaining the interface impedance spectrum across a range of frequencies swept from sub-Hz to 100 kHz. Several impedance spectrums were obtained for a series of MCLR samples with concentrations: $0.01\mu g/l, 0.1\mu g/l, 1\mu g/l$ and $10\mu g/l$, Fig. 3.4 and Fig. 3.5 show the results of these measurements. The proper frequency of operation for a capacitive transducer lies in the range of impedance spectrum where the capacitance element at the interface is dominant. This range can be found by observing the bode plots for the range where the phase shift is roughly 90°. The results in Fig. 3.4 shows that for our capacitive transducer, this range is approximately from 0 to 4 kHz, at lower frequencies, the capacitance is more stable with lower drifting, but considering the real-time application and sampling rate limitations, the frequency of operation is fixed to roughly 1 kHz. Fig. 3.5 shows that for lower MCLR concentrations, the transducer requires a longer time to show a trackable change with respect to baseline capacitance obtained in the buffer, this time is approximately 10 minutes for the lowest tested MCLR concentration ($0.01\mu g/l$). Fig. 3.5 also shows that the transducer is capable of detecting the varying MCLR concentrations with distinct capacitance levels at each step. The EIS characterization helps the design of the proceeding units of the biosensor, specifically for the critical parameter operation frequency.

3.4 Conclusions

The series *RC*, interface model for non-faradaic measurement of a capacitive transducer is adopted for the design in this work. The primary transducers are gold patterned electrodes modified with SAM, cross linker and MCLR antibody. The transducers are characterized with CV and EIS tests to verify the quality of the chemical surface block with the least potential pinholes, and for obtaining the range of frequencies that the interface recognition capacitance

is dominant in the model. After characterizing the transducer for sensitivity and operational frequency range, a secondary transduction is proposed in this work that incorporates two functional transducers within a “bridge” scheme for differential measurement. The design approach and proposed bridge structure is given in Chapter 4.

CHAPTER 4. BRIDGE STRUCTURE FOR INTERFACIAL CAPACITANCE MEASUREMENTS

4.1 Introduction

When tracking a 1% full-scale change in the interface capacitance, noise, non-specific binding, and drift are among the primary obstacles against achieving lower detection limits for real-time measurements [12, 21, 24, 38]. Sensitive capacitance measurement methods like EIS [21, 32] that was discussed in Chapter 2, although popular for the electrochemical solution-electrode capacitance measurement, are complicated and the ability of these frequency sweep methods for tiny fractional change in the capacitance with interference from the environment like noise, etc., is not quite clear. Considering the simple implementation and field-deployment for capacitance measurement, the commercially available capacitance to digital (C2D) converter ICs are good options like work presented in [43] for the detection of cancer biomarkers. But this readily available C2D ICs, operate over certain range of full-scale capacitance that is not always compatible with the absolute capacitance value of some of the electrochemical capacitive electrode transducers. Macro-electrodes that have tens to hundreds of nF capacitance range like the ones introduced in [12] are not in the range of commercial C2Ds. Therefore, the C2Ds cannot always be used to interface with any random capacitive transducer made for particular application.

Other than the abovementioned methods, sensitive secondary transduction with circuit techniques can be utilized for sensitivity enhancement and overcoming the issues like noise, drift, etc... This chapter focuses on the development of such a secondary transducer employing bridge structure. Here it is shown that the previously reported works on bridge systems for

measuring an unknown actual capacitance or capacitances of a medium do not work for the particular case of electrochemical solution-electrode capacitance.

Other than compatibility with interfacial capacitance requirements, a differential bridge employing two transducers in the bridge opposite legs is proposed here that leads to higher sensitivity and better common-mode noise suppression. The quality of the bridge balancing is very important considering that the bridge is tracking the tiny response signal related to roughly less than couple of percent fractional changes of the capacitive transducers. The bridge structure is analyzed in detail in this chapter, and the effect of an initial imbalance on the dynamic range and minimum detectable capacitance change is characterized.

The proposed bridge structure is both DC and AC excited, and the interface is modeled with series *RC* components; the other networks in the bridge are also designed in such a way that the bridge can be both AC and DC balanced. The response signal at the bridge output is a differential sinusoid, and in the ideal case, the response is zero at the initial balance and any change in the response sinusoidal amplitude and differential phase w.r.t. the excitation source represents a change in the interface impedance. In other words, the acquired data at the bridge output is a complex voltage signal. An analysis of the proposed bridge structure relates the capacitance and resistance change at the interface to the amplitude and differential phase or the real and imaginary parts of the acquired response, with simple algebraic equations. This is a significant advantage for the field deployment because no complex data fitting algorithm is required to extract the capacitive change from the response.

The proposed bridge with fully digital balancing network structures and straight forward balancing algorithm that can be carried out by a simple microcontroller is implemented with all practical implementation detail and guidelines here. The main design specification is

considered an 8-bit detection resolution within a full-scale capacitance change of roughly 1%. The setup for actual experiments and proper placement of the electrodes in the bridge are shown in this chapter, and the effectiveness of the provided configurable DC bias paths for the transducers in drift rate control is experimentally verified. The capacitance measurement reliability is verified after a custom amplification and filtering readout board proceeded by a data acquisition and processing unit employing a simple microcontroller that is interfaced with the bridge. The details for the readout design and capacitance detection with the 8-bit resolution are given in the following chapters.

4.2 Capacitive Bridge Systems

Bridge structures for characterizing unknown impedances can be used as simple secondary transducers before signal amplification leading to higher sensitivity. As previously discussed in Chapter 3, solution-electrode capacitive-based functional transducers, using label-free non-faradaic measurements, are modeled with a series *RC* circuit model. The impedance of an unknown *RC* circuit (C_X and R_X in Fig. 4.1) is classically characterized using either a Schering Bridge, Fig. 4.1(a), or a Wien Bridge, Fig. 4.1(b), with the simple balance condition equations shown at the center of each bridge [44, 45]. Unfortunately, these bridge circuits are

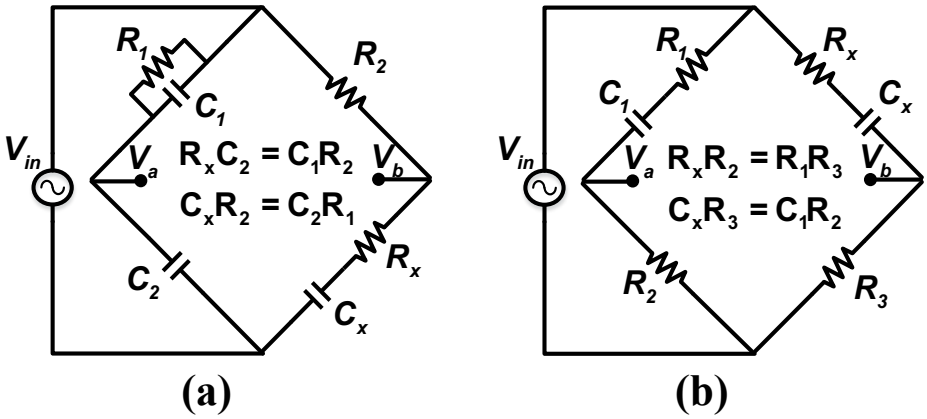

Fig. 4.2 Two common bridge circuits for characterizing the impedance of an unknown RC circuit with the balancing condition equations, (a) the Schering Bridge and (b) the Wien Bridge.

so-called AC bridges, utilizing only AC excitation signals, but the interfacial capacitive electrodes require a stable DC bias voltage as well.

While a DC bias voltage could be applied to the unknown impedance by super-imposing a DC offset onto the AC excitation signal, V_{in}, the presence of the series capacitors ($C_1$and C_2) makes balancing the DC voltages at nodes V_a and V_b impossible. Mismatch in the DC voltages at nodes V_a and V_b means that the bridge structure is not symmetrical around nodes V_a and V_b. In this case, other than potential drift of the unequally biased transducers, given the high proceeding differential gain of the readout circuit, a large amount of common-mode to differential conversion will take place in the response path. The common-mode to differential conversion reduces the overall sensitivity of the sensor and makes the balancing cumbersome.

Other than the classical Schering and Wien bridges, bridge circuit based impedance systems for characterizing the capacitance of a medium are reported in [46-49]. These systems are useful in certain applications, but for electrode-solution interfacial capacitance sensing, some specific modifications are required to make them suitable. One of the major drawbacks of these systems is that they are solely AC driven, but electrochemical capacitive electrodes need to be biased for capacitance establishing. This electrode bias in interfacial capacitance sensing can be used to partially control the real-time DC drift caused by the faradaic leakage currents. Therefore a bridge with both configurable AC and DC excitation is required for the specified applications.

These sensors need to be excited with a very small signal amplitude (less than 50 mV) to avoid non-linear response and damage to the chemical layer on the surface [21, 24]. The

structures in [46] are excited with very large sinusoidal amplitudes. Therefore the sensitivity of these systems for a full-scale fractional capacitance change of 1% is unclear. The bridge architectures reported in [47-49] do not offer solutions to reduce the common-mode interference effects like noise and non-specific binding. Since with the electrochemical capacitive biosensors, a change in capacitance is the goal of detection rather than accurately measuring the medium under test, the effect of possible initial bridge imbalance on the response linearity should be characterized. These issues and the method for the design of a suitable bridge structure for electrochemical solution-electrode interfacial capacitance sensing to be used along with a discrete real-time amplification readout has not been addressed yet.

4.3 Proposed Ideal Series RC Bridge Model and Design

A bridge structure that can overcome the problems associated with the previously reported capacitive bridges and compatible with the solution-electrode based capacitive transducers, can act as secondary transduction before the readout circuitry. Considering the expected very small fractional transducer impedance change sensitivity is one main design

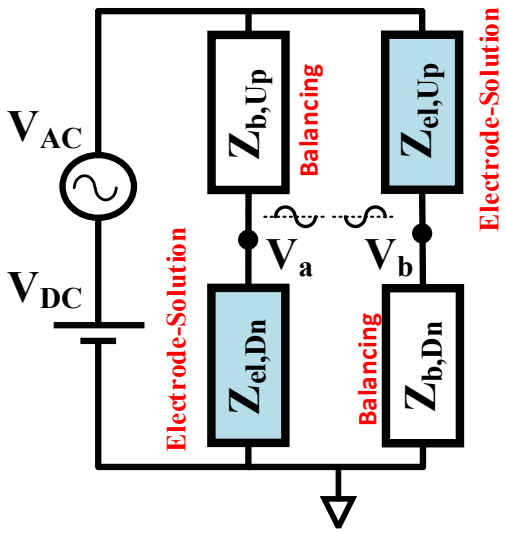

Fig. 4.3 General block diagram of a differential bridge structure for solution-electrode interfacial capacitance sensing

target for such structure. Differential bridge structure like the one shown in Fig. 4.2 can increase the sensitivity if the impedance of both functional transducers, $Z_{el,Up}$ and $Z_{el,Dn}$, change in the same direction. Moreover, all deterministic and common mode interferences stemming from the solution, or electrode, will be canceled at the output. For capacitive measurements, at the solution-electrode interface, a small AC signal is required for impedance sensing, and a specific DC bias is also necessary for establishing the nominal interface capacitance as well as controlling faradic drift. Therefore, Fig. 4.2 needs to be modified with circuit elements considering the above requirements and proper interface model at the frequency of measurement.

The equivalent model in Fig. 3.2(b) at a capacitive dominant frequency, can replace $Z_{el,Up}$ and $Z_{el,Dn}$ blocks in the bridge. With the series, RC part in the interface model, an AC path for the signal is provided. Considering that the large parallel, R_{leak}, forms a DC bias path in the bridge, an extra arrangement is required for the DC bias balancing because the R_{leak} value for each individual transducer is different and depends on the chemical surface coating. To make an independent balancing scheme for the AC and DC signals, the blocks $Z_{b,Up}$ and $Z_{b,Dn}$, should be adjusted accordingly so that they both provide a balanced AC and DC signal to the electrode and toward ground.

The proposed differential bridge with a series RC interface model for the transducers, AC, and DC balancing paths is shown in Fig. 4.3. The resistors, R_d, are responsible for setting the DC bias and should be at least ten times larger than the magnitude of the transducer's impedance at the measurement frequency. The maximum value of R_d is limited by the amount of R_{leak}, R_d should be several orders of magnitude smaller than R_{leak}. A fine-tune variable resistor potentiometer can be included in series with one of the R_d's to compensate for

occasional mismatch. The AC balancing path is formed by the series resistors and capacitors balancing $R_{b,Up}, C_{b,Up}$ and $R_{b,Dn}, C_{b,Dn}$.

For balanced AC output at V_a and V_b the values of $R_{b,Up}, C_{b,Up}$ and $R_{b,Dn}, C_{b,Dn}$ should be matched to $R_{el,Up}, C_{el,Up}$ and $R_{el,Dn}, C_{el,Dn}$, respectively. The value of the DC path resistors R_d needs to be set much higher than $\sqrt{R_{el,Up}^2 + (1/C_{el,Up}^2\omega^2)}$ but much smaller than the corresponding R_{leak} to avoid both loading the AC signal path and electrode impedance.

The response data at the bridge differential output of Fig. 4.3 is the magnitude and differential phase of $V_a - V_b$. Analysis of the bridge output magnitude and phase transfer function would make it feasible to relate the transducer capacitance change to either of the response magnitude and phase, with simple algebra rather than complicated data fitting approaches. Equations (4.1)-(4.3) show the ideal balancing condition for series RC bridge and (4.4) and (4.5) show the transfer function for the bridge differential output magnitude and phase for the case of initially matched impedances with only transducer capacitances changing,

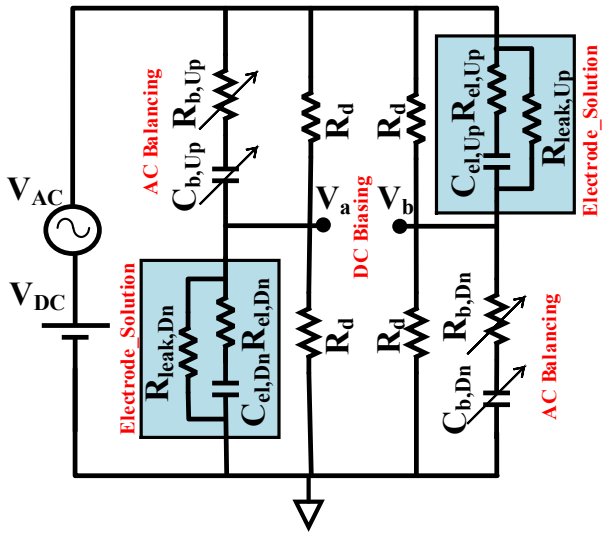

Fig. 4.4 The proposed block diagram of series RC bridge based on the non-faradaic model for solution-electrode interface, with two differentially placed transducers, AC balancing networks and DC biasing path

i.e. $C_{el,Up} = C_{el,Dn} = C_{el} + \Delta C_{el}$, $C_{b,Up} = C_{b,Dn} = C_{el}$ and $R_{el,Up} = R_{el,Dn} = R_{b,Up} = R_{b,Dn} = R_{el}$.

$$C_{el,Up}C_{el,Dn} = C_{b,Up}C_{b,Dn} \tag{4.1}$$

$$R_{el,Up}R_{el,Dn} = R_{b,Up}R_{b,Dn} \tag{4.2}$$

$$R_{b,Up}C_{b,Up} + R_{b,Dn}C_{b,Dn} = R_{el,Up}C_{el,Up} + R_{el,Dn}C_{el,Dn} \tag{4.3}$$

Equation (4.4) shows that with the change in the capacitance of the transducer ΔC_{el} and fixed R_{el} the bridge output magnitude will change linearly with ΔC_{el}. The bridge output differential phase with respect to source ideally remains unchanged with small fractional capacitive change $\Delta C_{el}/C_{el}$. This bridge output transfer function behavior with capacitive change can be used in the practical experiment, to relate the collected voltage data at the bridge output to the transducer's mere capacitive change with binding.

$$|V_a - V_b| = \frac{\frac{|\Delta C_{el}|}{2C_{el}}|V_{AC}|}{\sqrt{1+\omega^2 R_{el}^2 C_{el}^2}} \tag{4.4}$$

$$\angle(V_a - V_b) = -atan(\omega R_{el} C_{el}) - \angle V_{AC} \tag{4.5}$$

Considering (4.4), it can be observed that if $\omega^2 R_{el}^2 C_{el}^2 \ll 1$, the sensitivity of the magnitude to the capacitance (slope) will be higher. Therefore, the makeup of the electrode and the solution conductivity directly affect the response sensitivity. The frequency of excitation and size of the electrode effective surface, in this case, should be picked so that $R_{el} \ll 1/\omega C_{el}$.

Apart from the ideal case, unfortunately, perfect balancing, $|V_a - V_b| = 0$, of the bridge in Fig. 4.3 with discrete resistors and capacitors in the balancing networks, is not always possible mainly due to the finite resolution of the tuning arrays ($R_{b,Up}$, $R_{b,Dn}$, $C_{b,Up}$, and $C_{b,Dn}$) and signal real-time drift. If the signal change rate at the output of the bridge is much faster than the signal drift rate while balancing and actual binding, the drift effect will be minor on

the measurement resolution. But, limitations in the implementation of balancing networks will cause some level of initial imbalance in the bridge that leads to certain performance degradation in dynamic range and detection resolution. The required resolution for the balancing arrays and the bridge's initial imbalance threshold, however, can be decided for specific performance metrics by deriving the bridge transfer function in the presence of mismatches. This analysis will help to determine the resolution of the balancing arrays, and based on the absolute value of the interface impedance, give a rough estimate of the achievable detection resolution.

4.4 Balancing and Mismatch Analysis

Although the ideal transfer functions in (4.4) and (4.5), show a simple relationship between the response magnitude and phase and the fractional capacitance change of the transducer ($\frac{\Delta C_{el}}{C_{el}}$), in practice achieving a perfect ideal balance at the bridge output is not likely due to limited balancing array resolution and drift. The drift rate for the case of non-faradaic capacitive transducers can be controlled by applying a DC bias to the electrode that reduces the potential faradaic leakage currents from the electrode surface. Theoretically, if there is a zero voltage gradient between the electrode and solution, there will be no charge flow from the electrode surface toward the solution. Therefore, in the proposed setup, the solution is also biased at the same DC voltage value that the bio-functional electrode is excited for the drift control. With the proper drift control, the primary non-ideal bridge performance is caused by the balancing array limitations.

Capacitive or resistive mismatches might affect the target measurement dynamic range, sensitivity and/or linearity, which will be shown in this section by deriving the non-ideal bridge transfer functions in the presence of a mismatch. But this non-ideal effect can be controlled by

picking the array resolution in such a way that the initial imbalance does not affect the final performance. This means that mainly the quality of balancing will determine the final achievable detection resolution and dynamic range, using a bridge. Analyzing the response transfer functions with a non-perfect balanced bridge, in this case, is necessary for extracting the capacitance change data in the practical experiment.

The bridge's initial capacitive or resistive mismatch will introduce a decrease in the dynamic range of the bridge output with the target capacitive change or non-linearity in lower detection limits, respectively. These effects are explored theoretically in the following.

4.4.1 Capacitive Mismatch

Eq. (4.6), (4.7) show the non-ideal bridge magnitude and phase transfer functions with merely a capacitance mismatch and all matched impedances while the electrode capacitances change i.e. $C_{el,Up} = C_{el,Dn} = C_{el} + \Delta C_{el}$, $C_{b,Up} = C_{el} + \Delta C, C_{b,Dn} = C_{el}$ and $R_{el,Up} = R_{el,Dn} = R_{b,Up} = R_{b,Dn} = R_{el}, \frac{\Delta C_{el}}{C_{el}} \ll 1$.

$$|V_a - V_b| \approx \frac{\left|\Delta C_{el} - \frac{\Delta C}{2}\right| |V_{AC}|}{2C_{el}\sqrt{1+\omega^2 R_{el}^2 C_{el}^2}} \tag{4.6}$$

$$\angle(V_a - V_b) \approx -atan(\omega R_{el} C_{el}) - \angle V_{AC} \tag{4.7}$$

Considering the balanced bridge except for a mismatch in capacitance $C_{b,Up}$, by an amount ΔC, Fig. 4.4 shows the ideal case (black) and the transfer function of the bridge output magnitude in the presence of an initial capacitive mismatch. The phase transfer function is not shown here because it remains the same with a capacitive mismatch and not a function of the transducer's fractional capacitance change. The typical resistance and capacitance values utilized for this simulation are $C_{el} = 300\ nF$, $R_{el} = 200\ \Omega$ and $\omega = 2\pi \times 1000\ rad/s$. The full scale (FS) fractional capacitance change for the simulation in Fig. 4.4 is considered $\frac{\Delta C_{el}}{C_{el}} =$

1%, and nominal resolution lines (1, 2 and 3 bits) for an 8-bit dynamic range (DR) are drawn for clarity, the studied mismatch levels are $\frac{\Delta C}{C_{el}} = \pm 1\%$. With the capacitive mismatch, the approximate magnitude of the bridge output in (4.6) still changes linearly with a horizontal shift. If the expected electrode capacitance change and the mismatch are in opposing directions (red), the dynamic range will shrink. The resolution lines are shown in Fig. 4.4 indicate that for the example of 1% full-scale transducer capacitance change, if the mismatch is on the same order of magnitude, for higher values of $\frac{\Delta C_{el}}{C_{el}}$, data would be lost due to saturation, despite the linear fashion of the response.

By implementing the balancing capacitance array, in fine and coarse sets and binary waited so that the resolution of the fine capacitance array is equal or smaller than target

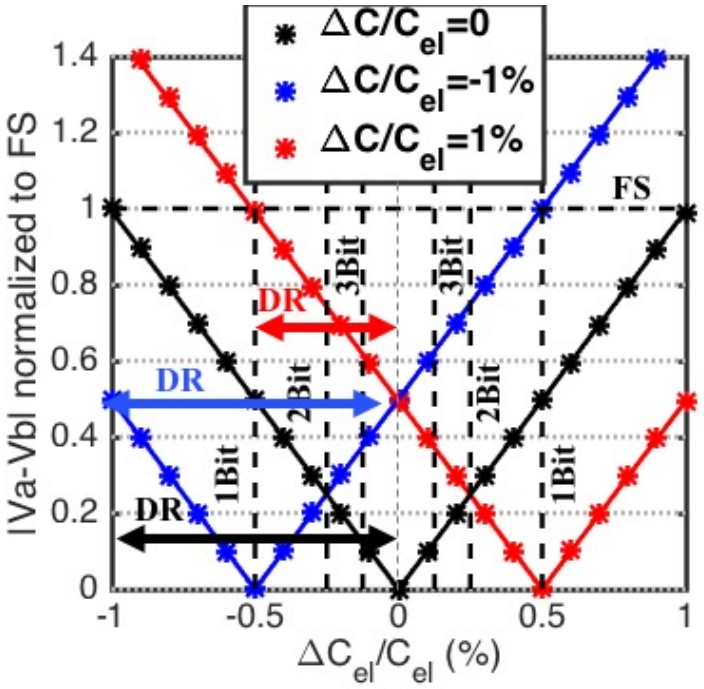

Fig. 4.5 The series RC bridge output magnitude $|V_a - V_b|$, vs fractional capacitance change $\frac{\Delta C_{el}}{C_{el}}$, for an initially perfectly balanced bridge except for capacitive mismatch of $\frac{\Delta C}{C_{el}} = 0, \pm 1\%$, leads to shrinking of DR. Numerical simulations are plotted with lines on top of markers that plotted using the approximate equations.

detection resolution, the capacitive mismatch effect can be hindered. Important points should be considered for the capacitance array design. By utilizing NP0/C0G grade capacitors, the absolute value of the capacitances in the array will be more stable. With the discrete implementation of the bridge using macro-electrodes, the minimum achievable capacitance resolution is on the order of several pF. Therefore, this method is applicable for absolute electrode capacitance on the order of tens of nF and higher. While the condition $R_{el} \ll 1/\omega C_{el}$leads to better sensitivity for transducer's capacitive change, at the same time makes the initial balancing more sensitive to capacitive mismatches.

4.4.2 Resistive Mismatch

The capacitive mismatch mainly shifted the magnitude transfer function horizontally without any effect on the phase transfer function for small fractional change in transducer capacitance. Resistive mismatch, however, affects both the bridge magnitude and phase transfer functions. Transfer functions of the bridge output in the presence of resistive mismatch are shown in equations (4.8)-(4.9), where,$C_{el,Up} = C_{el,Dn} = C_{el} + \Delta C_{el}$, $C_{b,Up} = C_{b,Dn} = C_{el}$ and $R_{b,Up} = R_{el} + \Delta R, R_{el,Up} = R_{el,Dn} = R_{b,Dn} = R_{el}, \frac{\Delta C_{el}}{C_{el}} \ll 1.$

$$|V_a - V_b| \approx \sqrt{\frac{\left(1+\omega^2 R_{el}^2 C_{el}^2\right)\left(\frac{\Delta C_{el}^2}{C_{el}^2}+\frac{\omega^2 \Delta R^2 C_{el}^2}{4}\right)}{4\left(1+\omega^2 R_{el}^2 C_{el}^2\right)^2+\Delta R\omega^2 C_{el}^2\left(\Delta R+\omega^2 R_{el}^2 C_{el}^2(\Delta R+4R_{el})\right)}}\,|V_{AC}| \tag{4.8}$$

$$\angle(V_a - V_b) \approx atan\left(\frac{\omega R_{el}\Delta C_{el}-0.5\omega\Delta R C_{el}}{(\Delta C_{el}/C_{el})+0.5\omega^2 C_{el}^2 R_{el}\Delta R}\right) - atan\left(\frac{\omega C_{el}(4R_{el}+\Delta R)}{\omega^2 C_{el}^2 R_{el}(2R_{el}+\Delta R)-2}\right) - \angle V_{AC} \tag{4.9}$$

Fig. 4.5 shows the magnitude and phase of $V_a - V_b$, with a resistively mismatched bridge, the values of the components are the same as ones used for simulations in Fig. 4.4. The full scale (FS) fractional capacitance change for the simulation in Fig. 4.5 is considered $\frac{\Delta C_{el}}{C_{el}} =$ 1%, and nominal resolution lines (1, 2 and 3 bits) for an 8-bit dynamic range (DR) are drawn

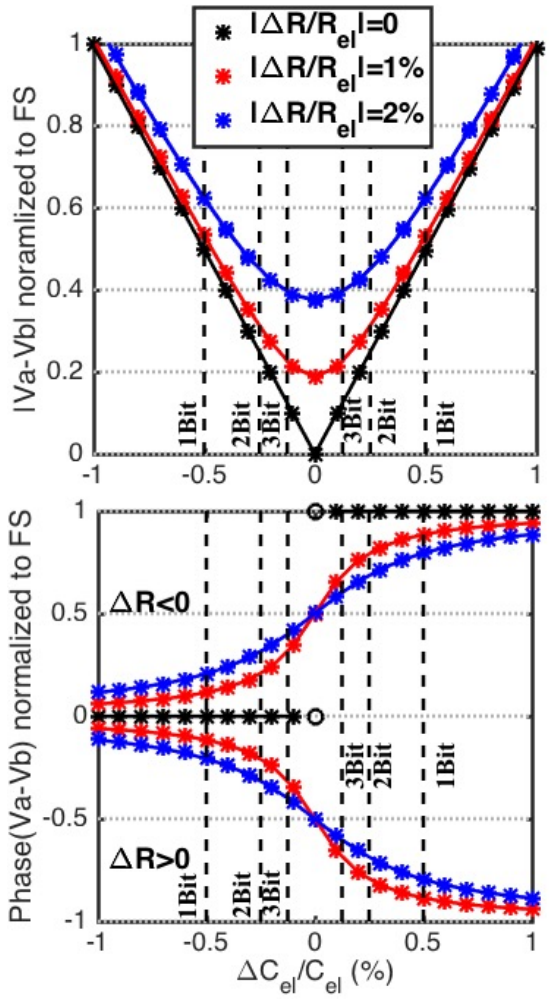

Fig. 4.6 The series RC bridge magnitude response $|V_a - V_b|$, vs fractional capacitance change $\frac{\Delta C_{el}}{C_{el}}$, for an initially perfectly balanced bridge except for resistive mismatch of $\frac{\Delta R}{R_{el}} = 0, 1 \; and \; 2\%$, leads to nonlinearity and worse detection resolution. Numerical simulations are plotted with lines on top of markers that plotted using the approximate equations.

for clarity, the studied resistive mismatch levels are $\frac{\Delta R}{R_{el}} = \pm 1\%$, for an initially perfect balanced bridge. It is apparent from (4.8) that resistive mismatch causes nonlinearity in the bridge output voltage magnitude. Looking at the normalized magnitude plot in Fig. 4.5, this non-linearity manifests itself mainly at lower detection limits (i.e., at smaller $\frac{\Delta C_{el}}{C_{el}}$). Nonlinearity gets stronger if the capacitive reactance of the electrode (i.e., $|1/\omega C_{el}|$) is not

significantly larger than the solution resistance, R_{el}. As the magnitude data get non-linear with a resistive mismatch, the phase of the bridge output changes more linearly with ΔC_{el} for lower detection limits as shown in Fig. 4.5 for the blue and red curves.

This is specifically important to notice that at the range of capacitance change where magnitude goes non-linear, phase data can be used, leading to higher sensitivity and dynamic range. Additionally, with known expected fractional capacitance change and the required minimum resolution, minimum balancing resistance to keep the dynamic range at the linear portion of the magnitude plot can be determined using (4.8). Given the absolute value of the solution resistance, such adjustment might not be feasible, specifically for cases when R_{el} is on the order of hundreds of Ω, where the ON-resistance of switches in the array can affect the balancing resolution. This challenge can be addressed by designing the resistive balancing array in fine- and coarse-tuning sets. In this way, the fine-tuning array has the minimum practical resolution, and the phase data is used along with the magnitude for the case of non-linear response because of resistive mismatch.

4.4.3 Balancing

Given the analysis of non-ideal balancing effects on the response, the balancing method and final capacitance change extraction method needs to be thought of carefully. With the expected very small fractional capacitance change, the amplification readout interface following the bridge needs to provide a high differential gain to achieve a wide dynamic range on the quantifiable response. The fully differential scheme proposed for the design in this work can lead to the common-mode to differential conversion issue if the impedance matching for balancing is not carried out correctly. To avoid the common-mode to differential conversion problem, the overall impedance on the positive bridge end (V_a) should be matched to the total

impedance connected to the negative end (V_b), in other words, $Z_{b,Up}$ should be matched to $Z_{el,Up}$ and $Z_{b,Dn}$ to $Z_{el,Dn}$, respectively.

With the two-unknown impedance in the bridge legs, a two-step balancing algorithm where the bridge is balanced for the unknown electrode impedances one after the other is simpler (e.g., first $R_{b,Dn}$ and $C_{b,Dn}$ are set equal to $R_{el,Dn}$ and $C_{el,Dn}$, then $R_{b,Up}$ and $C_{b,Up}$ are set equal to $R_{el,Up}$ and $C_{el,Up}$). In the two-step method first, one of the electrodes is replaced with a known series RC impedance (R_t and C_t) and after the bridge is balanced with the balancing algorithm shown in Fig. 4.6, then the second electrode is placed back, and the bridge is rebalanced using the same method. In this way, first $R_{b,Dn}$ and $C_{b,Dn}$ are set equal to $R_{el,Dn}$ and $C_{el,Dn}$ then $R_{b,Up}$ and $C_{b,Up}$ are set equal to $R_{el,Up}$ and $C_{el,Up}$.

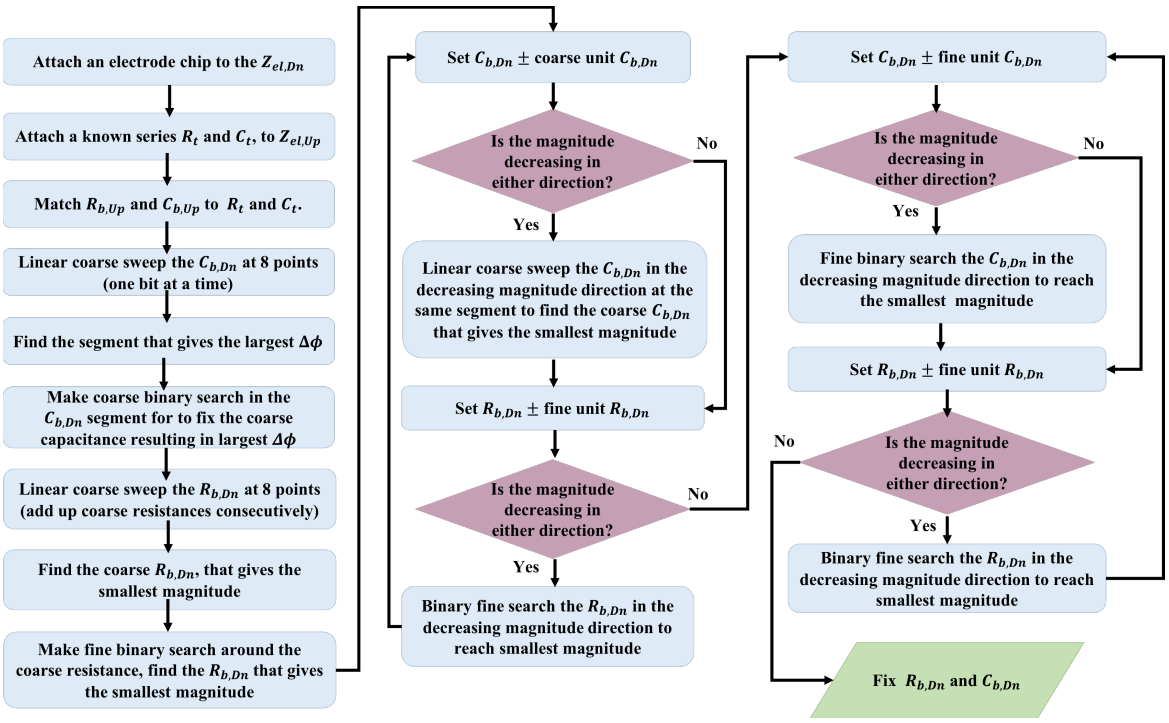

Fig. 4.7 Balancing algorithm

4.4.4 Capacitance Data Extraction

Once the bridge is balanced with the algorithm shown in Fig. 4.6, the common mode to differential conversion effect on the bridge response will be removed. A simple and accurate algebraic relationship using the balanced bridge transfer functions, the changing capacitance and possible change in resistance can be extracted from the collected $V_a - V_b$ magnitude and phase data. The algebraic operations can be easily carried out by the same microcontroller that performs the balancing and sine fitting tasks. Assuming the bridge is initially balanced with the known impedances $Z_{b,Up} = Z_{el,Up}$ and $Z_{b,Dn} = Z_{el,Dn}$, and considering any change in the transducer impedances will be represented by an effective resistance and capacitance change (ΔR_{el} and ΔC_{el}) on one of the electrodes, the approximate transfer functions (4.10) and (4.11) can be derived.

$$\left|\frac{V_a - V_b}{V_{AC}}\right| \left|1 + \frac{Z_{b,Dn}}{Z_{b,Up}}\right| \approx \frac{C_{b,Up}}{C_{b,Dn}} \sqrt{\frac{\frac{C_{b,Dn}^2 \omega^2}{R_{b,Dn}^2}\Delta R_{el}^2 + \frac{1}{R_{b,Dn}^2 C_{b,Dn}^2}\Delta C_{el}^2}{\left(1 + {R_{b,Up}}/{R_{b,Dn}}\right)^2 C_{b,Up}^2 \omega^2 + {1}/{R_{b,Dn}^2}\left(1 + \frac{C_{b,Up}}{C_{b,Dn}}\right)^2}} \tag{4.10}$$

$$tan\left[\angle(V_a - V_b) - \angle V_{AC} - \angle\left(\frac{Z_{b,Up}}{Z_{b,Up} + Z_{b,Dn}}\right) - atan\left(\frac{\left(1 + \frac{C_{b,Up}}{C_{b,Dn}}\right)}{C_{b,Up}\omega\left(R_{b,Up} + R_{b,Dn}\right)}\right)\right] \approx \frac{\Delta C_{el}}{C_{b,Dn}^2 \omega \Delta R_{el}} \tag{4.11}$$

(4.10) and (4.11) are drawn with the approximations considering $\frac{\Delta C_{el}}{C_{el}} \ll 1$ and $\frac{\Delta R_{el}}{R_{el}} \ll 1$.

All the parameters except ΔR_{el} and ΔC_{el} are known in (4.10) and (4.11), by replacing ΔR_{el} with its equivalent peer which is a linear function of ΔC_{el}, using the phase data from (4.11), into (4.10), ΔC_{el} can be easily extracted. Any initial imbalance level in the bridge in this way will cumulatively appear on the computed ΔR_{el} and ΔC_{el}, therefore by characterizing the bridge's initial balance point, this error can be calibrated out from the extracted values for capacitance and resistance. Another similar approach is to use the response of the real (Re) and imaginary (Im) parts to derive algebraic linear relationships directly with ΔR_{el} and ΔC_{el}, shown

in (4.12) and (4.13), using the same approximations. Any initial imbalance level in the bridge in this way will cumulatively appear on the computed ΔR_{el} and ΔC_{el}, therefore by characterizing the bridge's initial balance point, this error can be calibrated out from the extracted values for capacitance and resistance. The capacitive and resistive changes on the electrode are linearly related to each other as apparent in (4.12)-(4.13), therefore using these equations guarantee the linearity of the response data extraction.

$$\Delta R_{el} \approx Re\left(\frac{V_a-V_b}{V_{AC}}.\frac{Z_{b,Up}+Z_{b,Dn}}{Z_{b,Up}}\right)R_{el,Dn}\left(1+\frac{R_{b,Up}}{R_{b,Dn}}\right)+Im\left(\frac{V_a-V_b}{V_{AC}}.\frac{Z_{b,Up}+Z_{b,Dn}}{Z_{b,Up}}\right)\frac{1}{\omega C_{b,Up}}\left(1+\frac{C_{b,Up}}{C_{b,Dn}}\right), \quad (4.12)$$

$$\Delta C_{el} \approx -Re\left(\frac{V_a-V_b}{V_{AC}}.\frac{Z_{b,Up}+Z_{b,Dn}}{Z_{b,Up}}\right)C_{el,Dn}\left(1+\frac{C_{b,Up}}{C_{b,Dn}}\right)+Im\left(\frac{V_a-V_b}{V_{AC}}.\frac{Z_{b,Up}+Z_{b,Dn}}{Z_{b,Up}}\right)\omega C_{el,Dn}^2 R_{el,Dn}\left(1+\frac{R_{b,Up}}{R_{b,Dn}}\right). \quad (4.13)$$

4.5 Series RC Bridge Implementation for 8-bit Sensing Resolution

The design methodology and bridge structure discussed in Section 4.4 can be utilized to implement a hand-held biosensor for specific electrochemical capacitive sensing applications with very small (<1%) full-scale fractional capacitance change at the transducers. An experimental setup is designed for verification of the theory presented in the previous sections, with the target of an 8-bit sensing resolution within 1% full-scale dynamic range for the fractional solution-electrode capacitance change. Given the bridge structure and the interface model in Fig. 4.3, size and geometry of the effective interface surface and the solution ion content, make-up the interface impedance values at the frequency of measurement. For the case of non-faradaic measurement with the bridge structure, two electrodes (one working/functionalized and the other one counter) on each transducer chip is sufficient.

The capacitive transducer chips that are explained in Section 3.3 are measured to find the typical value of the electrode-solution interface impedance in the utilized model. After characterization with the single frequency of excitation set to 1 kHz (frequency at which the sensing element that is the surface capacitance, is dominant) and utilizing PBS 10mM, pH 7.2

as the solution, the equivalent series interface capacitance and solution resistance are typically around $300\,nF$ and $200\,\Omega$, respectively. The parallel leakage resistance R_{leak}, is also characterized to be several hundred $k\Omega$.

4.5.1 Balancing Arrays

With the knowledge of the typical value for the transducer interface model, and a target detection goal of 8-bit resolution for a 1% overall fractional capacitance change, the bridge balancing networks can be designed. Digitally tunable balancing capacitor/resistor arrays $C_{b,Up}, R_{b,Up}$ and $C_{b,Dn}, R_{b,Dn}$ are each designed in fine and coarse sets for the goal of fine balancing. Shown in Fig. 4.7(a) on the left, and Fig. 4.7(b), is the coarse digitally tunable capacitance ($CdC1 - CdC8$) array that is binary weighted with an 8-bit resolution and $1\,nF$ LSB value. In this way, if the target electrode capacitance is occasionally out of the maximum

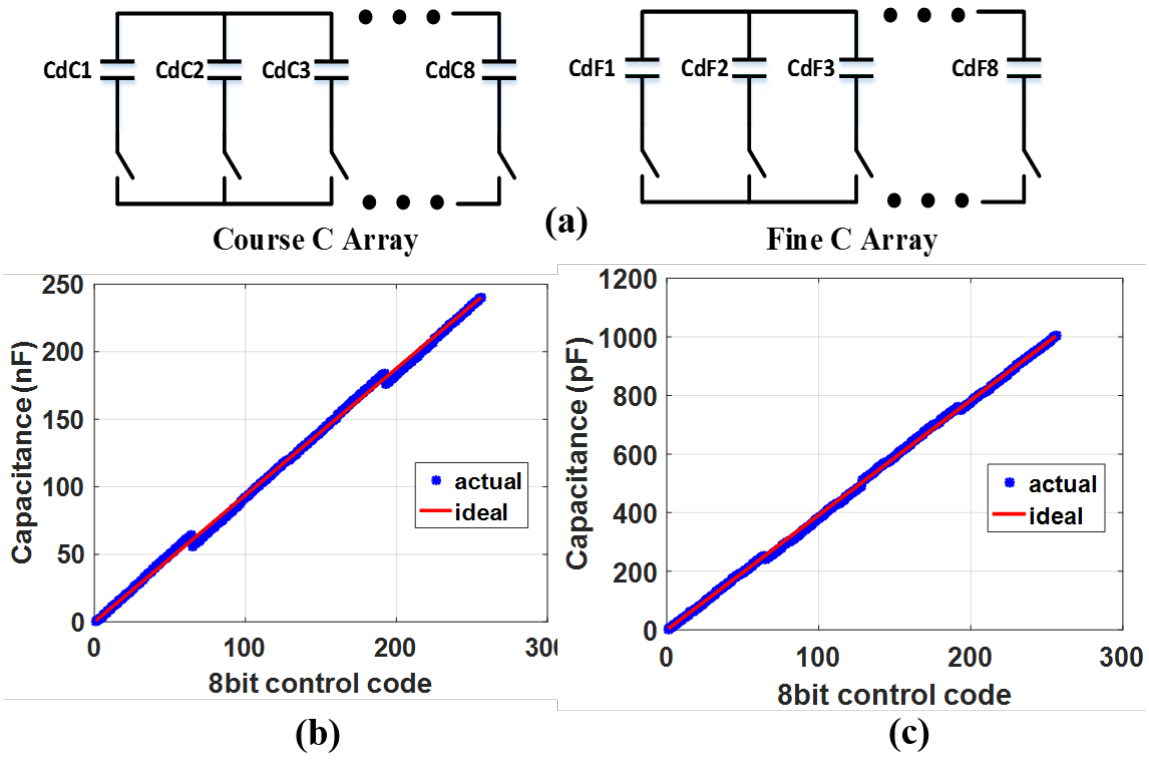

Fig. 4.8 (a) Structure of course and fine capacitance array (b) capacitance vs. 8bit control code course, (c) fine capacitance array

expected range, increasing the capacitance attached to the MSB will shift the larger half of the array by the amount added, and the overall range can be increased without the need for adjusting the whole array. The values of the capacitances attached to each bit of the coarse capacitance array are picked based on the possible commercial values so that no hundreds value is missing. The fine-tuning capacitance array Fig. 4.7(a), on the right $(CdF1 - CdF8)$,, and Fig. 4.7(c), on the right, is formed in 8-bit structure with minimum capacitance value of 4 pF the fine array is adjusted with commercially possible capacitance values so that no tenths capacitor values are missing and maximum achievable capacitance value on the fine array in this way is $1003\ pF$.

The coarse-tuning resistance array, shown in Fig. 4.8(a), left, has eight fixed $RdC = 100\ \Omega$ resistors that add up linearly to the overall value on the fine resistance array and shift the total resistance value by $100\ \Omega$ at a time. The fine balancing resistance array Fig. 4.8(a), on the right, and Fig. 4.8(b) is a binary-weighted 8-bit array, the values of the resistors in this

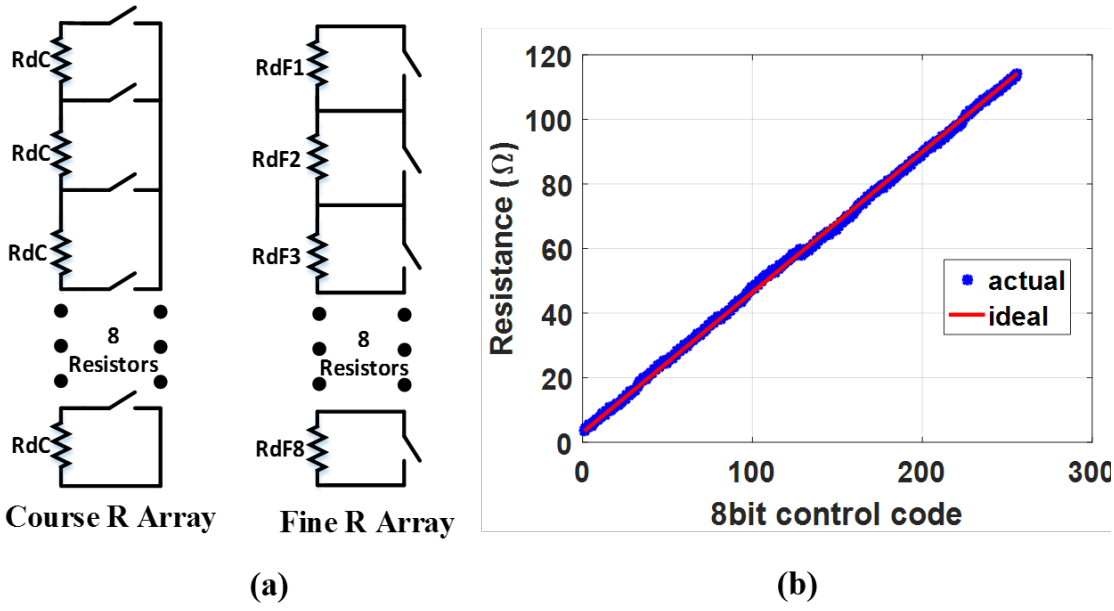

Fig. 4.9 (a) Structure of course and fine resistance array, (b) resistance vs. 8bit control code for fine resistance array

array ($RdF1 - RdF8$) is adjusted with respect to the commercial values and the ON resistance of the utilized switches (ADG811 from Analog device, roughly $0.5\ \Omega$) so that the resolution of the array is approximately $0.5\ \Omega$ and the final maximum resistance at the fine array is $114\ \Omega$. The characterization plots of the capacitance coarse and fine arrays with the available commercial components are shown in Fig. 4.7(b)-(c). Fig. 4.8(b) shows the characterization plot for the fine resistive arrays. These characterizations show that component values are adjusted in such a way that there are no missing codes corresponding to target values.

The offset resistance of the fine array caused by all the switches off state is approximately $3.5\ \Omega$. This offset is compensated at the first resistance of the coarse resistance array changed from $100\ \Omega$ to $96.5\ \Omega$. The digital AC balancing is performed by a microcontroller (TI-MSP432P401R). Each of the 8 balancing arrays is connected to an 8-bit latch (CY74FCT2573TSOC form TI) to control the array switches. The 8-bit array data is

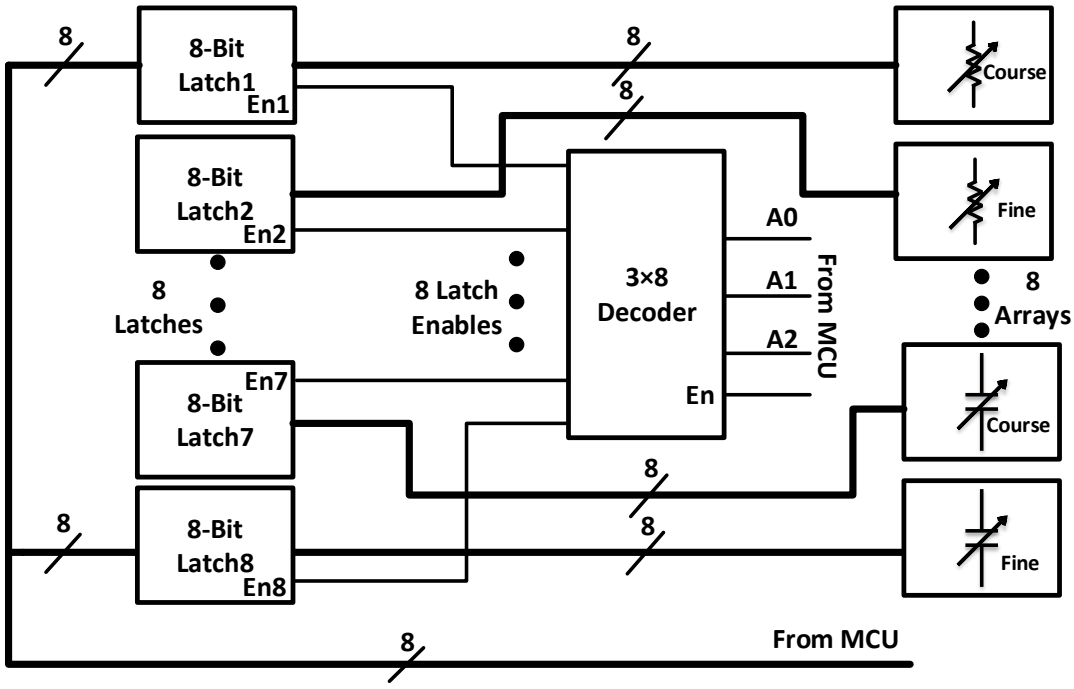

Fig. 4.10 Block diagram of digitally controlled balancing network, the MCU sends the 8-bit code to control the array switches and selects one array out of 8 at a time with the 3-bit enable control code ($A_2A_1A_0$)

written to a mutual data bus connected to the latch inputs, after a 3×8 decoder (CD74HC238 from TI) enables the target latch, data is transferred from the target latch output to the corresponding array switches. DC balancing resistors, R_d, are set to $50\ k\Omega$ which is more than ten times greater than typical electrode absolute impedance magnitude, $730.5\ \Omega$, at the frequency of $1\ kHz$ and still more than ten times smaller than the corresponding R_{leak}. A manually tunable $1\ k\Omega$ resistance is also inserted in the DC path for one time fine adjustment for any mismatch among the DC balancing resistors. The block diagram for the explained bridge design and the experimental setup is shown in Fig. 4.9.

With a $50\ mV_{rms}$ AC excitation and $200\ mV$ DC bias, an amplification and filtering board is costume designed and interfaced with the bridge to amplify the tiny differential response, $V_a - V_b$, to the full-scale voltage of the utilized ADC. The microcontroller's (MCU) first task is balancing the bridge and then carrying out dual-channel 3-parameter sine fitting on the real-time acquired data. Therefore, the final real-time data of the system in Fig. 4.9 would be the amplified bridge output amplitude (response amplitude) and response differential phase with respect to the AC excitation.

4.5.2 Drift Control

As mentioned earlier in real-time measurements for non-faradaic capacitive sensing, the signal drift is one of the major obstacles against fast and accurate data collection. The actual response variation caused by binding might get lost due to the random drift that is faster. Specifically, with the bridge concept, a largely drifting response makes it very difficult or impossible to balance the bridge. Thus, the drift rate of the response should be controlled in such a way that the balancing speed and expected response variation caused by binding is much higher than the drift rate.

Other than random events happening at the electrode surface like the displacement of the thiol chains, one major reason for the drifting solution-electrode interface capacitance is the faradaic leakage current flow from the un-blocked surface pin-holes [42]. Theoretically, by biasing the solution and electrode at the same DC potential, the flow of the faradaic currents should go to zero. A general block diagram showing the setup for interfacing the differential series RC bridge structure with an interface system is provided in Fig. 4.10. The differential placement of the electrodes along with the working and counter electrode placement and solution bias also is demonstrated in the bridge section of Fig. 4.10. By biasing the solution with an external Ag/AgCl reference electrode, the drift rate can be reduced. Fig. 4.11 shows the results of an experiment to validate the explained drift control strategy using the setup shown in Fig. 4.10.

The working electrodes connected to the bridge ends shown in Fig. 4.10 are biased with a 60 mV DC voltage. The experiment is performed once without a solution bias and once with solution biased using the external Ag/AgCl reference connected to a 60 mV DC voltage. The bridge is balanced in both cases, and the output response magnitude is recorded for 15 minutes, Fig. 4.11 shows that biasing the solution reduces the drift rate by approximately 7.3 times. Considering an ADC full scale of 1.2 V, the drift rate controlled by external solution bias is about 11.4 mV/min, if the binding rate and the balancing speed are faster than this value, then drifting will not cause significant problems for experimental validations.

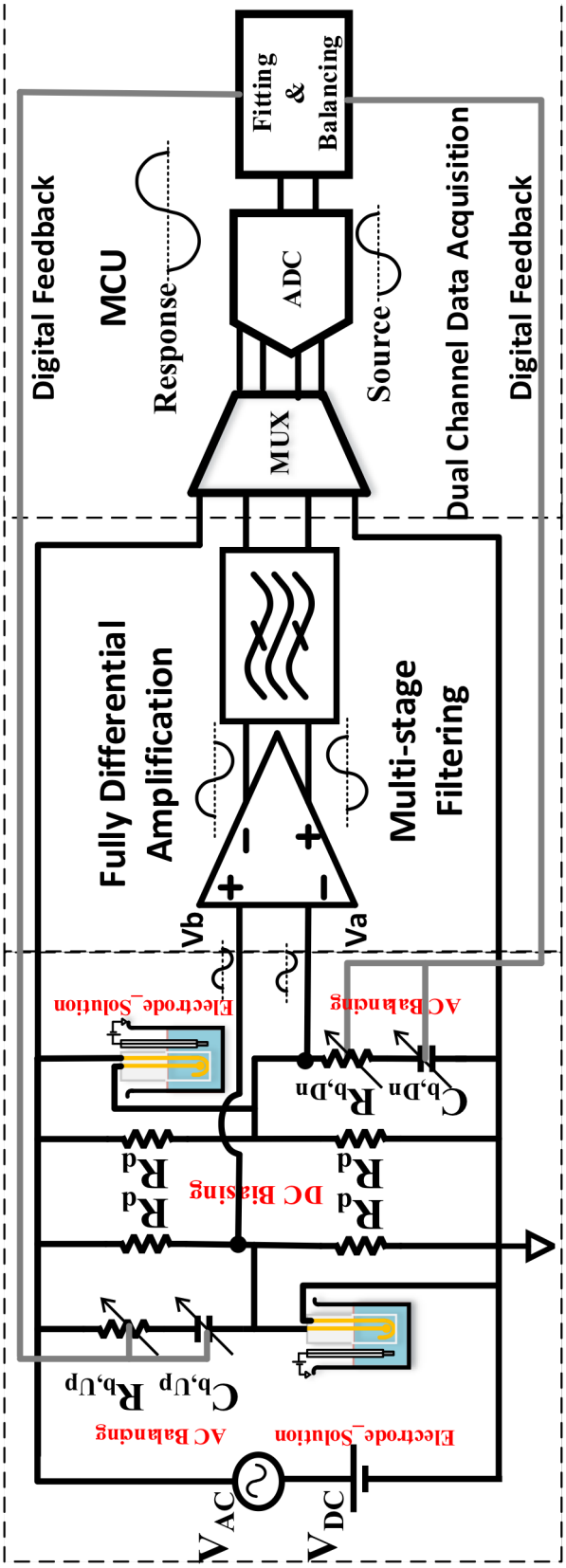

Fig. 4.11 General block diagram showing the setup for interfacing the differential series RC bridge structure with an amplification, filtering and data acquisition system, the placement of the differential measurement scheme and the working and counter electrode connection are shown. The working electrodes are connected to the nodes V_a and V_b. External DC biasing for solution is provided by an Ag/AgCl commercial electrode immersed in the solution.

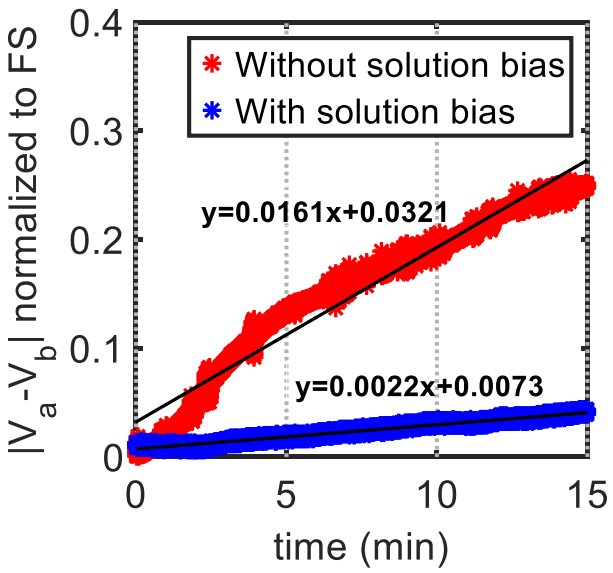

Fig. 4.12 Results of an experiment to validate the explained drift control strategy

4.6 Conclusions

The differential bridge structure with a series RC model for the solution-electrode interface improves the sensing performance before amplification readout at a low cost. With a proper bridge model, the configurable DC biasing for the electrodes and simultaneous but independent AC/DC balancing can be achieved. A differential bridge structure with two functional sensors is effective in reducing the non-random common-mode effects of noise, drift and non-specific binding. The voltage response signal can be related to the capacitance change with algebraic equation and without the need for complicated fitting algorithms, which is an advantage for faster processing of acquired data in real-time. Very common problem with many bridges that might lead to some response non-linearity or less sensitivity is the initial imbalance level of the bridge. With bridge characterized transfer function the bridge initial imbalance reason can be identified, calibrated and behavior with target capacitance change can be predicted.

Parameters like dynamic range, detection resolution and linearity are among the most important biosensor response characteristics that are directly related to bridge structure and balance quality. We propose a differential bridge model for real-time single frequency solution-electrode interfacial capacitive sensing. The impedances in the bridge legs are modeled in such a way that independent AC and DC balancing and configurable DC bias for the transducers are feasible.

A complete characterization of the bridge output differential magnitude and phase transfer functions is carried out in this chapter to observe the ideal bridge output response with target capacitance change. Then, with the goal of achieving an 8-bit detection resolution, the effect of initial bridge imbalance levels and its relevance to the resolution of balancing network arrays are studied. Design trade-offs among the absolute value of interface model elements, the amplification gain, the required minimum discrete capacitance or resistance in the balancing network, to achieve certain dynamic range and resolution are discussed. The proper electrode placement in the bridge legs and a suitable bridge balancing algorithm are investigated. In the design process, the balancing algorithm is designed so that a simple and low-cost microcontroller can carry out the balancing task in addition to data acquisition/fitting. Given the complete analysis, a bridge structure is designed and implemented with a target of 8-bit resolution for the sensing of 1% full-scale fractional capacitance change.

After the bridge implementation, the electrode placement and bias method are experimentally tested to find an effective way to control the real-time output drift. Design and implementation of the suitable and sensitive amplification and filtering readout along with the data acquisition and processing unit to interface with the designed bridge are discussed in Chapters 5 and 6.

CHAPTER 5. AMPLIFICATION AND FILTERING INTERFACE FOR CAPACITIVE BRIDGE TRANSDUCTION

5.1 Introduction

For most diagnostic and monitoring applications including capacitive sensing of MCLR, the detection target concentrations of interest are generally small, ranging from ng/L to $\mu g/L$ that gives rise to a total change in impedance of often only a few percent over the entire full range of detection. To complicate matters, for development of a field-deployable read-out board compatible with interfacial capacitive transducers, avoiding physical damage of the functional layer of the transducer and also nonlinear distortion effect on the response, require that the magnitude of the applied AC excitation remain small (typically $< 50\ mV$) [21].

Let's consider that the series RC bridge structure shown in Fig. 4.3 with the transducers inserted. If the bridge impedances are $Z_{b,Up}$, $Z_{b,Dn}$, $Z_{el,Up}$ and $Z_{el,Dn}$ and the change in the transducers impedances are considered as $\Delta Z_{el,Up}$ and $\Delta Z_{el,Dn}$, where $\frac{\Delta Z_{el,Up}}{Z_{el,Up}} + \frac{\Delta Z_{el,Dn}}{Z_{el,Dn}} \approx 1\%$, the differential output voltage can be found using the following equations.

$$V_a - V_b = \frac{(Z_{el,Up}+\Delta Z_{el,Up})(Z_{el,Dn}+\Delta Z_{el,Dn}) - Z_{b,Up}Z_{b,Dn}}{(Z_{el,Up}+\Delta Z_{el,Up}+Z_{b,Dn})(Z_{b,Up}+Z_{el,Dn}+\Delta Z_{el,Dn})} V_{AC}$$

$$\approx \left(\frac{Z_{\mathrm{el,Dn}}\Delta Z_{\mathrm{el,Up}}}{(Z_{\mathrm{el,Up}}+\Delta Z_{\mathrm{el,Up}}+Z_{\mathrm{b,Dn}})(Z_{\mathrm{b,Up}}+Z_{\mathrm{el,Dn}}+\Delta Z_{\mathrm{el,Dn}})} + \frac{Z_{\mathrm{el,Up}}\Delta Z_{\mathrm{el,Dn}}}{(Z_{\mathrm{el,Up}}+\Delta Z_{\mathrm{el,Up}}+Z_{\mathrm{b,Dn}})(Z_{\mathrm{b,Up}}+Z_{\mathrm{el,Dn}}+\Delta Z_{\mathrm{el,Dn}})} \right) V_{AC}. \quad (5.1)$$

If $\frac{Z_{el,Up}}{Z_{el,Up}+Z_{b,Dn}} = \frac{Z_{b,Up}}{Z_{b,Up}+Z_{el,Dn}} = \alpha$ $(0 < \alpha < 1,\ real\ )$ and $Z_{el,Up} \gg \alpha \times \Delta Z_{el,Up}$, $Z_{el,Dn} \gg (1-\alpha) \times \Delta Z_{el,Dn}$:

$$V_a - V_b \approx \left(\frac{1}{\left(\frac{Z_{el,Up}}{\alpha \Delta Z_{el,Up}}+1\right)\left(\frac{1}{1-\alpha}+\frac{\Delta Z_{el,Dn}}{Z_{el,Dn}}\right)} + \frac{1}{\left(\frac{Z_{el,Dn}}{(1-\alpha)\Delta Z_{el,Dn}}+1\right)\left(\frac{1}{\alpha}+\frac{\Delta Z_{el,Up}}{Z_{el,Up}}\right)} \right) V_{AC}. \quad (5.2)$$

$$V_a - V_b \approx \alpha(1-\alpha)\left(\frac{\Delta Z_{el,Up}}{Z_{el,Up}} + \frac{\Delta Z_{el,Dn}}{Z_{el,Dn}}\right) V_{AC}. \quad (5.3)$$

A typical excitation sine signal for this application has an AC amplitude on the order of $1 - 100\ mV$. Assuming the case where both fractional changes in (5.3) are less than 1% and the bridge is balanced perfectly, i.e. $\alpha = 1/2$, the maximum change in the amplitude of the bridge output will be less than $1\ mV$. Now with the target sensor resolution set to a modest 8-bits value, the LSB of the response to be detected will be several microvolts. An AC signal of $50\ mV_{rms}$ is utilized in our current design, therefore, with $\alpha = 1/2$, the maximum change at the bridge output will be $0.35\ mV$, if the target resolution for the sensor is 8-bits, then the LSB of the response will be equal to, $1.367\ \mu V$. Due to these small changes, extreme care must be taken in the design and implementation of the sensor interface circuit.

Some small, inexpensive, and low-power sensor interface circuits are proposed in the past like the ones in [50-52]. These systems are specifically designed for capacitive sensing and accelerometer applications. Other than AC excitation that is different for interfacial capacitance sensing, these systems also do not have the transducer DC bias requirement. Therefore, the performance of these types of interface circuits for real-time operation with interfacial capacitive transducers is not validated. On the other hand, if a discrete implementation is required, unfortunately, some factors limit the performance of field-deployable sensor interface circuits. For example, the frequency response analyzer introduced in [16], which is among the famous AC interface impedance measurement methods, may lead to unwanted drifting and sensitivity degradation when implemented with discrete blocks such as multipliers and phase shifters.

Typical precision opamps that would be used in this application have input-referred noise voltages that are on the order of tens of $nV/\sqrt{Hz}$. To maintain a practical input signal-to-noise ratio (SNR) greater than 1, with microvolt-level transducer output voltages, the

effective noise bandwidth of the sensor interface circuit could be limited to only a few tens of hertz. Moreover, a voltage gain of approximately 60–80 dB will be required to make effective use of the ADC. Such extreme amplification and filtering require highly accurate component matching, extensive shielding, and careful circuit design. Considering the abovementioned challenges, differential measurement technique is used here to reduce the effects of common-mode noise, drift, and temperature variation.

A comprehensive study of the design tradeoffs between overall sensor system complexity and performance in low-cost (< \$10), real-time electrode-solution interfacial capacitance sensing applications, particularly with small fractional detection capacitance change signals (< 1%) is given in this chapter. It is shown here that, at the same time, the careful design of the two-channel digital acquisition and processing (sine fitting) utilizing a single microcontroller can relax the requirements specifically for the amplification and filtering unit. A complete theoretical design procedure along with a practical discrete implementation example is presented here targeting real-time, low-cost, and field-deployable capacitive biosensor with less than 1% full-scale change in the transducer output voltage and 8-bit characteristic change resolution. The detailed structure of the proposed interface architecture suitable for bridge transduction is shown in Fig. 5.1

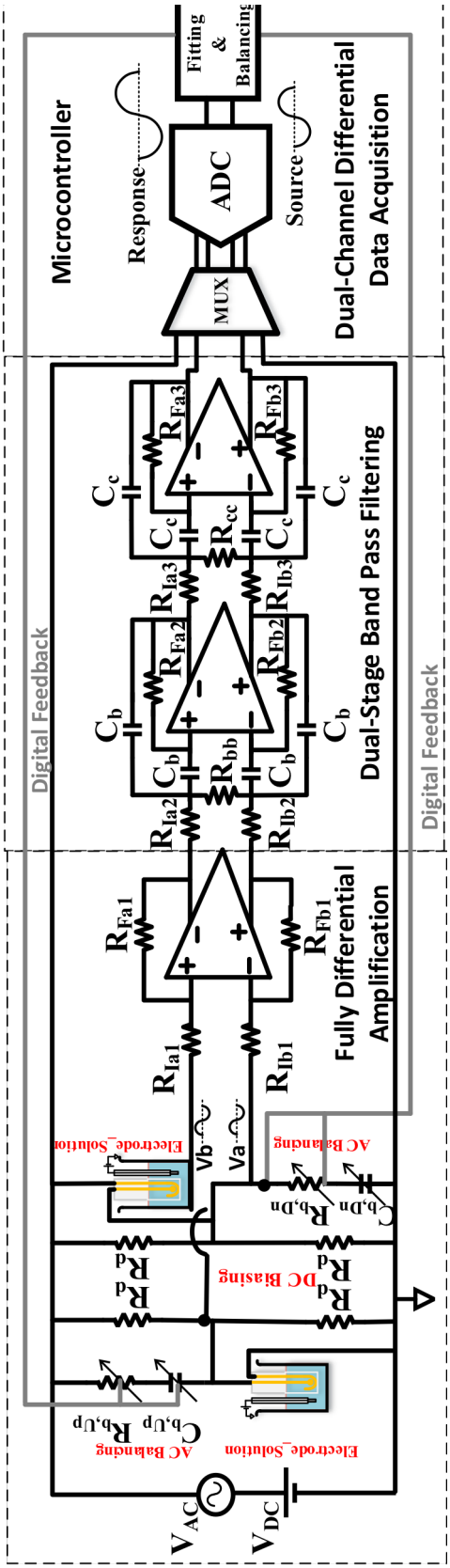

Fig. 5.1 Proposed capacitive bridge based transduction interface system, fully differential signal path, an amplification and two stage band pass filtering unit.

In the proposed system of Fig. 5.1 bridge transducing, amplification, filtering, and dual-channel digital data acquisition is done fully differential mainly to achieve better noise and common mode interference cancellation and expand the overall sensor dynamic range. To maintain symmetry along all signal paths, fully differential amplification and filtering with a fixed gain is designed using differential precision opamps (LTC6363) instead of single-ended instrumentation amplifiers. The total required gain for 8-bit detection resolution is distributed among three stages, one mainly amplification and two amplification and filtering. Multiple feedback active band-pass filter architecture is adopted both for its lower cost, fully differential implementation and flexibility for tuning parameters like gain, A_{filter}, bandwidth, BW, and center frequency, f_{center}. If $R_{F_a} = R_{F_b} = R_F$, $R_{I_a} = R_{I_b} = R_I$, for each filter gain, bandwidth and center frequency are set by (5.4)-(5.6).

$$A_{filter} = \frac{R_F}{2R_I}. \tag{5.4}$$

$$BW = \frac{1}{2\pi C_b R_F}. \tag{5.5}$$

$$f_{center} = \frac{1}{2\pi C_b \sqrt{(R_I||R_b)R_F}}. \tag{5.6}$$

Considering the required large differential amplification gain and detection resolution, the design of the readout interface for the bridge output requires careful analysis based on several important parameters such as overall noise and common-mode to differential conversion. The effective noise bandwidth and CMRR mainly affect the best possible minimum detection limit, while common-mode to differential conversion due to mismatches and imbalance leads to degraded sensitivity and nonlinearity. The abovementioned issues are discussed in the design of the amplification and filtering unit in this chapter.

Dual-channel differential data acquisition, sin fitting, and bridge balancing are all done employing single MCU. Response signal frequency known a priori makes the sine fitting

algorithm simpler. However, to achieve the target 8-bit resolution with simpler real-time processing, the most important parameters to consider while developing the fitting algorithm are SNR, number of samples taken per cycle and sensitivity to potential excitation frequency shifts, the design tradeoffs for coherent real-time 3 parameter sine fitting are also given in the data acquisition and processing design in Chapter 6.

5.2 Amplification and Filtering Design

The primary role of the single-frequency amplification and filtering unit shown in Fig. 5.1, is to amplify the detection signal and filter the unwanted out of band interference. On the other hand, the amplification unit is interfaced to the data acquisition unit for real-time processing. Thus, design parameters like gain and specifications like CMRR, output, and input common-mode voltage, filter bandwidth, etc. are set both by the bridge response range, resolution, and ADC full-scale range.

CMRR or the amplification and filtering interface's ability to reject the common-mode bridge output voltage (initial balance case) and amplify the differential voltage change at the bridge output (case of impedance change with detection) is one of the most critical design parameters. Failing to reject the common-mode at the bridge output considering the high required differential gain will lead to unpleasant common-mode to differential conversion that not only gives rise to false detection signal but also limits the dynamic range. Additionally, common-mode to differential conversion will affect the bridge balance and make it more challenging.

The ADC's full-scale range, A_{FS}, determines the total required amplification gain, the higher A_{FS}, the more amplification required. The typical full-scale ADC voltages available are on the order of $(1 - 5\ V)$, three-stage amplification, and filtering interface is proposed here to

provide the total differential gain in the order of $70-80$ dB. To have an estimation of how much common-mode rejection is required, consider the case with the bridge initially balanced in the middle so that $\alpha = 1/2$ and $|V_a| = |V_b|$ equal to tens of millivolts and if the differential LSB change at the bridge output, $|(V_a - V_b)_{LSB}|$, is only several microvolts. These values will be amplified by the common-mode to differential gain $A_{v,CMdiff}$, and interface differential gain, $A_{v,diff}$, respectively. To maintain the 8-bit resolution capability in this case, the following criteria should be met:

$$\frac{A_{v,diff} \cdot |(V_a - V_b)_{LSB}|}{A_{v,CMdiff} \cdot |V_{ab,CM}|} > 2. \tag{5.7}$$

For the interface utilized in our current design, $A_{FS} = 1.2\ V$, with the maximum differential voltage at the bridge output equal to $0.35\ mV$, a gain of $3428.6\ V/V$ or 70.7 dB is required to map the full-scale change at the bridge output to the full scale at the ADC. The abovementioned criteria set the minimum for the $CMRR_{Total} = \frac{A_{v,diff}}{A_{v,CMdiff}} = 94.19\ dB$ which with $A_{v,diff} = 70.7\ dB$, requires the $A_{v,CMdiff}$ to be at least $-23.49\ dB$.

Other than common-mode to differential conversion, noise, is one other critical issue, degrading the lower detection limit and shrinking the dynamic range. However, proper filtering of the response signal will greatly improve the signal to noise ratio at the ADC input. Various sources causing common mode to differential conversion and SNR degradation at the output of interface before ADC, are analyzed in the following. In light of this analysis, parameters like gain of each stage, effective noise bandwidth (ENB) and matching order can be determined and based on the best achievable SNR at the board output, sin fitting algorithm in the data acquisition unit can be picked and designed.

5.2.1 Common-Mode to Differential Conversion

Typical fully differential amplifiers for precision measurements provide relatively high CMRR values of around $100\ dB$. However, when configured as a differential amplification stage, as shown in Fig. 5.1 the total CMRR of the stage, $CMRR_{Stage}$, is determined not only by the CMRR of the opamp, $CMRR_{Opamp}$, but also the matching between the two symmetrical feedback ratios β_a and β_b, which are defined as follows:

$$\beta_b = \frac{R_{Fb1}}{R_{Fb1}+R_{Ib1}}, \quad \beta_a = \frac{R_{Fa1}}{R_{Fa1}+R_{Ia1}}. \tag{5.8}$$

If $\beta_b = \beta + \frac{\Delta\beta}{2}$ and $\beta_a = \beta - \frac{\Delta\beta}{2}$, therefore, $\beta_b - \beta_a = \Delta\beta$ and $\beta_b + \beta_a = 2\beta$. $CMRR_{Stage}$ is derived as [53]:

$$CMRR_{Stage} \approx \frac{1}{\frac{1}{CMRR_{Opamp}}+\frac{\Delta\beta}{\beta}}. \tag{5.9}$$

Fig. 5.2 shows the percent degradation in $CMRR_{Stage}/CMRR_{Opamp}$ the ratio for various $CMRR_{Opamp}$, versus the percent feedback matching ratio. As expected from (5.9), for higher values of $CMRR_{Opamp}$, a tighter feedback ratio matching is required. Now given a typical amount of $CMRR_{Opamp} = 100\ dB$, feedback matching ratios better than 0.001% and 0.003% are required to obtain $CMRR_{Stage}$ of $50\ dB$ and $25\ dB$ respectively.

With discrete implementation, one main challenge for feedback ratio matching is the component tolerances. For a given stage with a differential voltage gain, $A_{v,dd}$, $R_{Fb} = A_{v,dd}R_{Ib}$, if the resistance, R's tolerance ΔR, is included as following:

$$R_{Ib} = R \pm \Delta R,\ R_{Fb} = A_{v,dd}R \pm \Delta R. \tag{5.10}$$

Feedback ratio matching is related to the component tolerance using the following derivations:

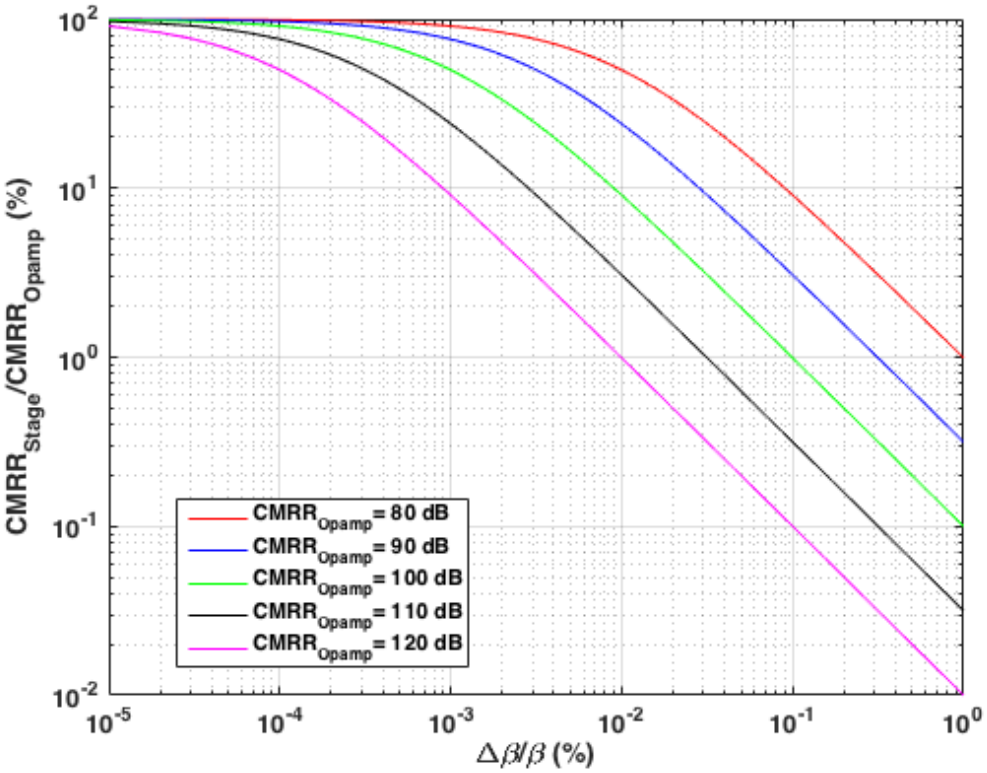

Fig. 5.2 Percent degradation in CMRR of each stage over the Opamp CMRR ($CMRR_{Stage}/CMRR_{Opamp}$) ratio, versus the percent feedback matching ratio for various $CMRR_{Opamp}$

$$\frac{\Delta\beta}{\beta} = \frac{\beta_b - \beta_a}{\beta} = \frac{\frac{A_{v,dd}R \pm \Delta R}{(A_{v,dd}+1)R \pm 2\Delta R} - \frac{A_{v,dd}R \pm \Delta R}{(A_{v,dd}+1)R \pm 2\Delta R}}{\frac{A_{v,dd}R \pm \Delta R}{(A_{v,dd}+1)R \pm 2\Delta R}} = \frac{\pm 2\frac{\Delta R}{R}}{(A_{v,dd}+1) \pm 2\frac{\Delta R}{R}}. \tag{5.11}$$

For $\frac{\Delta\beta}{\beta} \ll 1$,

$$\pm\frac{\Delta R}{R} = \frac{\Delta\beta}{\beta}\frac{A_{v,dd}+1)}{2(1-\frac{\Delta\beta}{\beta})} \approx \frac{\Delta\beta}{\beta}\frac{(A_{v,dd}+1)}{2}. \tag{5.12}$$

The plots of required percent component tolerance for various stage gain, $A_{v,dd}$, versus percent feedback ratio mismatch is shown in Fig. 5.3. Lower component tolerance is required to get the same feedback matching ratio as the stage gain gets higher.

Other than the amplification stage symmetrical feedback ratio mismatch, another important source of common-mode to differential conversion, is the misbalanced bridge interfacing the amplification stage. In other words, misbalance of equivalent impedances

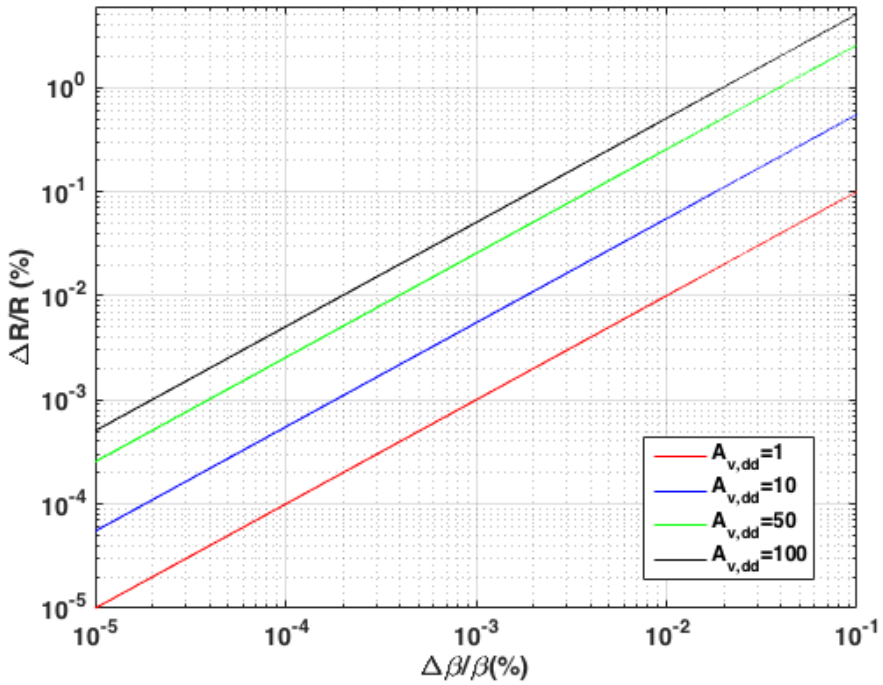

Fig. 5.3 percent component tolerance for various stage differential gain, $A_{v,dd}$, versus percent feedback ratio mismatch

connecting to nodes V_a and V_b, as shown in Fig. 5.1 also translates into a feedback ratio mismatch and introduces common-mode to differential conversion. To avoid this effect, the balancing of the bridge should be done based on the following criteria:

$$Z_{b,Up} \| Z_{el,Dn} = Z_{el,Up} \| Z_{b,Dn}. \tag{5.13}$$

Also, to balance the Whetstone based bridge of Fig. 5.1 the nulling condition is:

$$Z_{b,Up} Z_{b,Dn} = Z_{el,Up} Z_{el,Dn} \tag{5.14}$$

From (5.13) and (5.14) it can be inferred that balancing the bridge by setting $Z_{\mathrm{b,Up}} = Z_{\mathrm{el,Up}}$ and $Z_{\mathrm{el,Dn}} = Z_{\mathrm{b,Dn}}$, sets $V_a - V_b = 0$, while common-mode to differential conversion is avoided. Note that although setting $Z_{\mathrm{b,Up}} = Z_{\mathrm{el,Dn}}$ and $Z_{\mathrm{el,Up}} = Z_{\mathrm{b,Dn}}$, meets bridge output null condition but depending on the functional electrodes mismatch, strong common mode to differential conversion effect might take place.

The bridge, differential amplification, and dual-stage filtering are cascaded stages in the interface readout. In [54] the contribution of each stage, $CMRR_{Stage_i}$, on the total CMRR, $CMRR_{Total}$, of a cascade of 3 differential stages is investigated and derived in (5.15). Where A_{v,dd_i}, and A_{v,cc_i} are the differential to differential and common-mode to common-mode gains of the i[th] stage, respectively.

$$\frac{1}{CMRR_{Total}} \approx \frac{1}{CMRR_{Stage_1}} + \frac{1}{\frac{A_{v,dd_2}}{A_{v,cc_2}} CMRR_{Satge_2}} + \frac{1}{\frac{A_{v,dd_2}}{A_{v,cc_2}} \frac{Av,dd_3}{Av,cc_3} CMRR_{Satge_3}}. \quad (5.15)$$

The output common-mode (DC) voltage, V_{OCM}, of the fully differential amplifiers, used in this design, is set at $A_{FS}/2$, to cover the full ADC dynamic range equally. For this purpose, precision opamps with internal common-mode feedback are utilized that set the output common-mode voltage to a specific value defined by the user. This external voltage is supplied from a voltage regulator to be more stable and properly bypassed with a capacitor to reduce the potential associated noise [55]. However, if the specified V_{OCM}, is not at the mid rail of the precision differential opamp supply voltages, the external voltage source should have enough current drive capability to supply the extra required drive current. With the internal common-mode feedback utilized, A_{v,cc_i}, is equal to $1\ V/V$. Thus, if the two filtering stages are identical, with same gains and characteristics, the effect of the CMRR of the first stage on the $CMRR_{Total}$ is dominant compared to higher stages. Therefore, bridge balancing and component matching on the first amplification stage has the most significant effect on the total CMRR and common-mode to differential conversion effect.

5.2.2 Noise Analysis

Electronic circuits and components in the read-out interface, as well as the bridge itself including the electrodes, are contributing with different degrees to the overall noise at the amplification and filtering output before the ADC. The narrow bandpass filtering is proposed

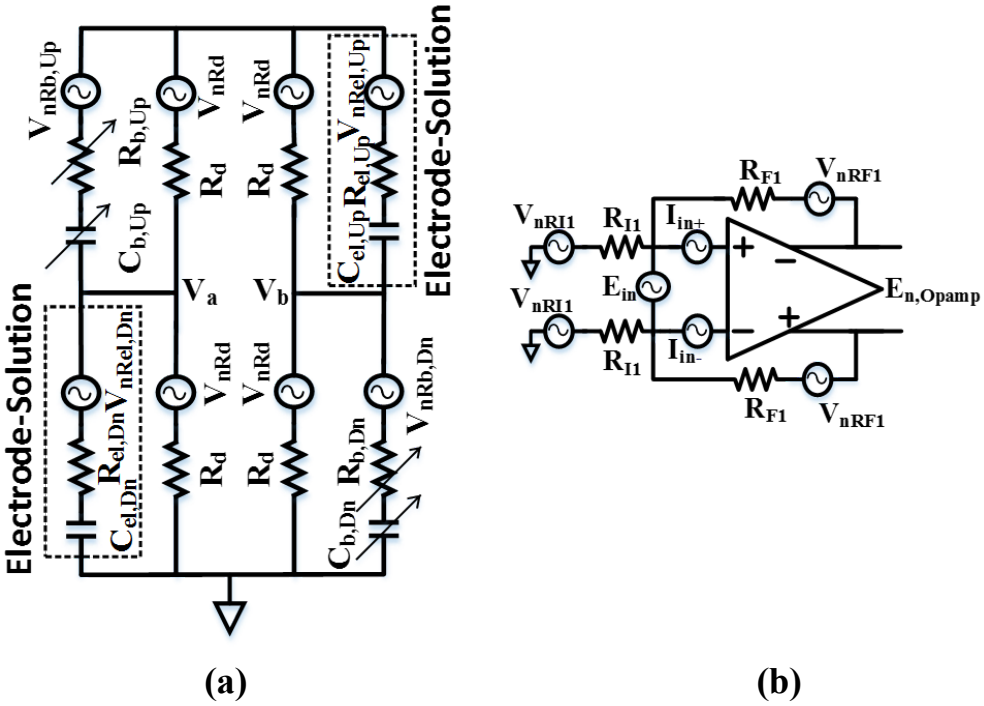

Fig. 5.4 . Noise model for (a) capacitive series RC bridge and (b) fully differential amplifier incorporating the resistance noise sources and amplifier input voltage and current noise

in the system shown in Fig. 5.1 to improve the SNR at the ADC input, the two identical multiple feedback [56] bandpass filters are mainly cascaded to obtain higher order (4th) and also even gain distribution. The effective noise bandwidth (ENB) of the cascaded filter stage is the main parameter affecting the final SNR, and more importantly, the minimum detection limit. The filter center frequency, f_{in}, is determined by application and set to the typical value 1 kHz in this paper. Noise analysis of the bridge and amplification interface however, is required to be able to define the necessary ENB for an 8-bit detection resolution.

Consider the capacitive bridge with noise sources included shown in Fig. 5.4(a) The functional electrodes in this study are assumed as planar ones for non-faradaic measurement (no charge transfer across the interface). The electrode-solution interface is modeled as a series RC, the resistive part ($R_{el,Up}$and $R_{el,Dn}$) are solution resistance, and the capacitive part

($C_{el,Up}$ and $C_{el,Dn}$) are the interface capacitance. The electrodes makeup and solution conductivity are set so that at the frequency of operation, $\omega_{in} = 2\pi f_{in}$, $R_{el} < |1/jC_{el}\omega_{in}| \rightarrow R_{el}C_{el}\omega_{in} < 1$, because the capacitance of the functional layer mainly changes with binding and dominant capacitive part leads to higher sensitivity. Gesteland et al. show in [57] that noise of a metal microelectrode can be modeled as thermal noise of resistance in a narrow band of frequency, where the corresponding resistance is real part of the electrode-solution interface impedance. In the bridge noise model shown in Fig. 5.4(a) $R_{b,Up}, C_{b,Up}, R_{b,Dn}$ and $C_{b,Dn}$ are RC balancing networks made with arrays of digitally controlled capacitors and resistors to balance the bridge for AC. R_ds are DC balancing resistive paths that provide a stable DC bias to the electrodes and equal DC voltage at V_a and V_b.

The value of the DC balancing resistors are set much larger than the magnitude of the electrode impedance not to load the electrodes and decrease sensitivity, therefore, knowing that $R_{el}^2 C_{el}^2 \omega_{in}^2 \ll 1$ leads to ${R_d}^2 C_{el}^2 \omega_{in}^2 \gg 1$. The associated noise sources with the electrodes and balancing resistors are in series with the corresponding resistance in Fig. 5.4(a), and are all representing thermal noise model for the resistance with units of $V/\sqrt{Hz}$:

$$V_{n_R} = \sqrt{4kTR}. \tag{5.16}$$

k is the Boltzmann's constant, T is the absolute temperature, and R is the corresponding resistance value. The noise model for a fully differential opamp with the associated amplification feedback resistors [58] is shown in Fig. 5.4(b) Again the resistors have the thermal noise voltage model in series and the noise sources E_{in}, $I_{in+}$and $I_{in-}$are the opamp input referred voltage and current noises, respectively. If the excitation source, V_{AC}, is assumed to be noiseless, and the output common mode voltage setting external source is properly

filtered, the total rms noise at the output of the amplification and filtering board, $\overline{E_{n,Total}}$, is obtained from (5.17).

$$\overline{E_{n,Total}} = \sqrt{\int_{f_L}^{f_H} \begin{matrix}(G_{N_1}^2 G_{N_2}^2 G_{N_3}^2 E_{n,Bridge}^2 + \\ G_{N_2}^2 G_{N_3}^2 E_{n,Stage_1}^2 + G_{N_3}^2 E_{n,Stage_2}^2 + E_{n,Stage_3}^2)\end{matrix} df}\,. \tag{5.17}$$

The output referred noise power of the bridge, $E_{n,Bridge}^2$, and output referred noise power of each amplification and filtering stage, $E_{n,Stage_i}^2$, is multiplied by the square of the noise gain, $G_{N_i}^2$, of the proceeding stages then summed and integrated over the bandwidth of the interface (lower, f_L, to higher, f_H, $3\ dB$ cut off frequency). The noise gain and output referred noise of each differential amplification, and filtering stage and output referred noise of the bridge are obtained from (5.18), (5.19).

$$G_{N_i} = 1 + \frac{R_{F_i}}{R_{I_i}}. \tag{5.18}$$

$$E_{n,Stage_i}^2 = G_{N_i}^2 E_{in_i}^2 + R_{F_i}^2\left(I_{in_i-}^2 + I_{in_i+}^2\right) + 2\,V_{n_{R_{F_i}}}^2 + 2\left(\frac{R_{F_i}}{R_{I_i}}\right)^2 V_{n_{R_{I_i}}}^2. \tag{5.19}$$

For a perfectly matched and balanced bridge, with $C_{el,Dn} = C_{el,Up} = C_{\mathrm{b,Up}} = C_{\mathrm{b,Dn}} = C_{el}$, $R_{el,Dn} = R_{el,Up} = R_{b,Dn} = R_{el,Up} = R_{el}$:

$$E_{n,Bridge}^2 = V_{a,n}^2 + V_{b,n}^2 = \frac{R_d^2 C_{el}^2 \omega_{in}^2}{1+(R_{el}+R_d)^2 C_{el}^2 \omega_{in}^2} V_{n_{R_{el}}}^2 + \frac{1+R_{el}^2 C_{el}^2 \omega_{in}^2}{1+(R_{el}+R_d)^2 C_{el}^2 \omega_{in}^2} V_{n_{R_d}}^2\,. \tag{5.20}$$

The power density of the noise sources in units of V^2/Hz are given in (5.21)-(5.24).

$$E_{in_i}^2 = e_w^2\left(1 + \frac{f_{enc}}{f}\right). \tag{5.21}$$

$$I_{in_i-}^2 = I_{in_i+}^2 = i_w^2\left(1 + \frac{f_{inc}}{f}\right). \tag{5.22}$$

$$V_{n_{R_{el}}}^2 = 4kTR_{el}. \tag{5.23}$$

$$V_{n_{R_d}}^2 = 4kTR_d. \tag{5.24}$$

e_w^2 and i_w^2, are the opamp input-referred voltage and current white noise powers. f_{enc} and f_{inc} are the voltage and current noise power density corner frequencies. Replacing (5.18)-(5.24) in (5.17) and assuming $\frac{f_H - f_L}{f_L} < 1$, $\frac{1}{f_{in}^2} \ll 1$, $\frac{f_{enc}}{f_L} \ll 1$ and $\frac{f_{inc}}{f_L} \ll 1$, yields (5.25).

$$\overline{E_{n,Total}} \approx \sqrt{ENB}\sqrt{\begin{matrix} G_{N_1}^2 G_{N_2}^2 G_{N_3}^2 (V_{n_{R_{el}}}^2 \left(\frac{R_d}{R_d+R_{el}}\right)^2 + V_{n_{R_d}}^2 \left(\frac{R_X}{R_D+R_X}\right)^2) + 2G_{N_2}^2 G_{N_3}^2 V_{n_{R_{F_1}}}^2 + 2G_{N_2}^2 G_{N_3}^2 \left(\frac{R_{F_1}}{R_{I_1}}\right)^2 V_{n_{R_{I1}}}^2 \\ +e_w^2 \left(G_{N_1}^2 G_{N_2}^2 G_{N_3}^2 + G_{N_2}^2 G_{N_3}^2 + G_{N_3}^2\right) + i_w^2 \left(2G_{N_2}^2 G_{N_3}^2 R_{F_1}^2 + 2G_{N_3}^2 R_{F_2}^2 + 2R_{F_3}^2\right) + 2G_{N_3}^2 V_{n_{R_{F_2}}}^2 \\ +2G_{N_3}^2 \left(\frac{R_{F_2}}{R_{I_2}}\right)^2 V_{n_{R_{I2}}}^2 + 2V_{n_{R_{F_3}}}^2 + 2\left(\frac{R_{F_3}}{R_{I_3}}\right)^2 V_{n_{R_{I3}}}^2 \end{matrix}} \quad (5.25)$$

$f_H - f_L$, is replaced with ENB, in (5.25), for a 4th order band-pass filter $ENB = 1.025(f_H - f_L)$ [58, 59]. Note that if $f_{enc} > f_L$ and $f_{inc} > f_L$, the effect of flicker noise cannot be neglected.

Based on (5.25), the ENB, of the required overall filtering to obtain 8-bit resolution can be determined using the typical application values for the bridge components, $R_{el} = 1\ k\Omega, R_d = 50\ k\Omega, C_{el} = 100\ nF$ and a gain distribution of $30 \times 10.6 \times 10.6$ for the amplification and filtering stages, respectively. The values for the resistors in the amplification and filtering stage are set as, $R_{F_1} = 300\ k\Omega, R_{I_1} = 10\ k\Omega, R_{F_2} = R_{F_3} = 16\ k\Omega, R_{I_2} = R_{I_3} = 750\ \Omega$. With the given component values for the current design, the RMS value of noise at the ADC input is $75.231\ \mu V/\sqrt{Hz}$. For SNR of $10\ dB$ and $5\ dB$, the bandwidth of $14.94\ Hz$ and $149.5\ Hz$ are required, respectively. In practice, however, for low frequency ($< 10\ kHz$) measurements, the effect of flicker noise cannot be neglected entirely and other sources of non-ideality like different component random variations may also add to the estimated total output referred RMS noise. There are also practical limitations on realizing filter bandwidth on the order of 10s of hertz, very small bandwidth leads to longer settling time of the interface response for step type input variations. Too narrow bandwidth is an important issue because the dynamics of analyte binding is fast and the readout interface should be able to follow the rapid changes in the response signal. Therefore the bandwidth value should be set both considering the amount of allowable noise and fast settling requirement. Although a higher filter bandwidth leads to worse SNR, proper digital signal processing technique, can effectively act as an additional filter and even extract the signal information buried in noise.

5.3 Amplification/Filtering ReadOut Characterization

The designed amplification and filtering board is implemented and characterized using the Audio precision lab instrument (Fig. 5.5) set up to generate 100 $\mu Vrms$ differential input sine signal. With the full-scale range of ADC set to 1.2 V, the differential gain of 3000 V/V or 70 dB is nominally required for full-scale amplification of 1% fractional change. To maintain the 8-bit resolution with the fully differential amplification and filtering it is necessary that the differentially amplified LSB signal becomes at least twice the common-mode induced

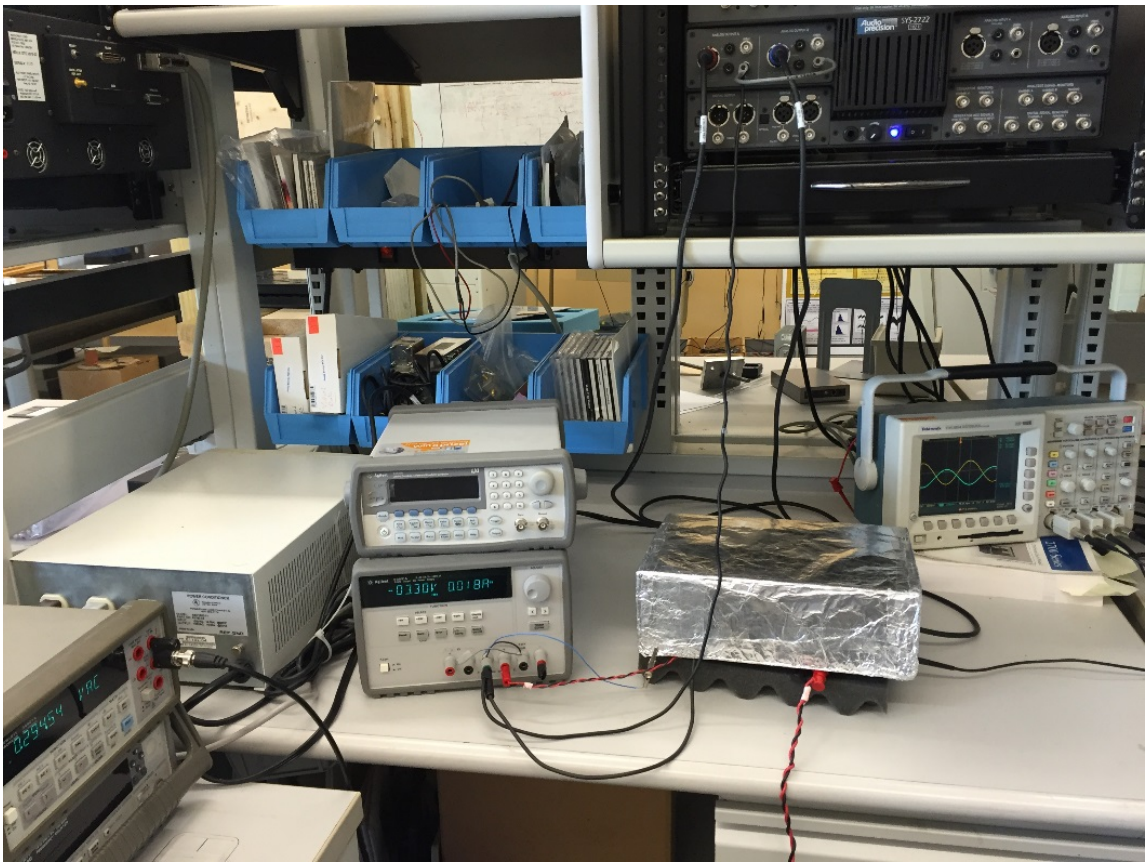

Fig. 5.5 Amplification and filtering board characterization using Audio precision

differential signal at the board output. This means a common-mode induced differential gain of less than -24 dB, yielding CMRR of 94 dB.

Noise coming from the bridge and amplification and filtering unit is analyzed and roughly estimated to be $75.231\ \mu V/\sqrt{Hz}$. To achieve an SNR of 10 dB or 5 dB at LSB detection limit, filter bandwidth of 14.94 Hz and 149.5 Hz is required, respectively. Considering the fast settling requirements as well, a bandwidth of 270 Hz is picked for filter design, and given the available commercial components the center frequency of the filter is expected to be 1.03 kHz. Fig. 5.6 shows the measured results of differential gain transfer

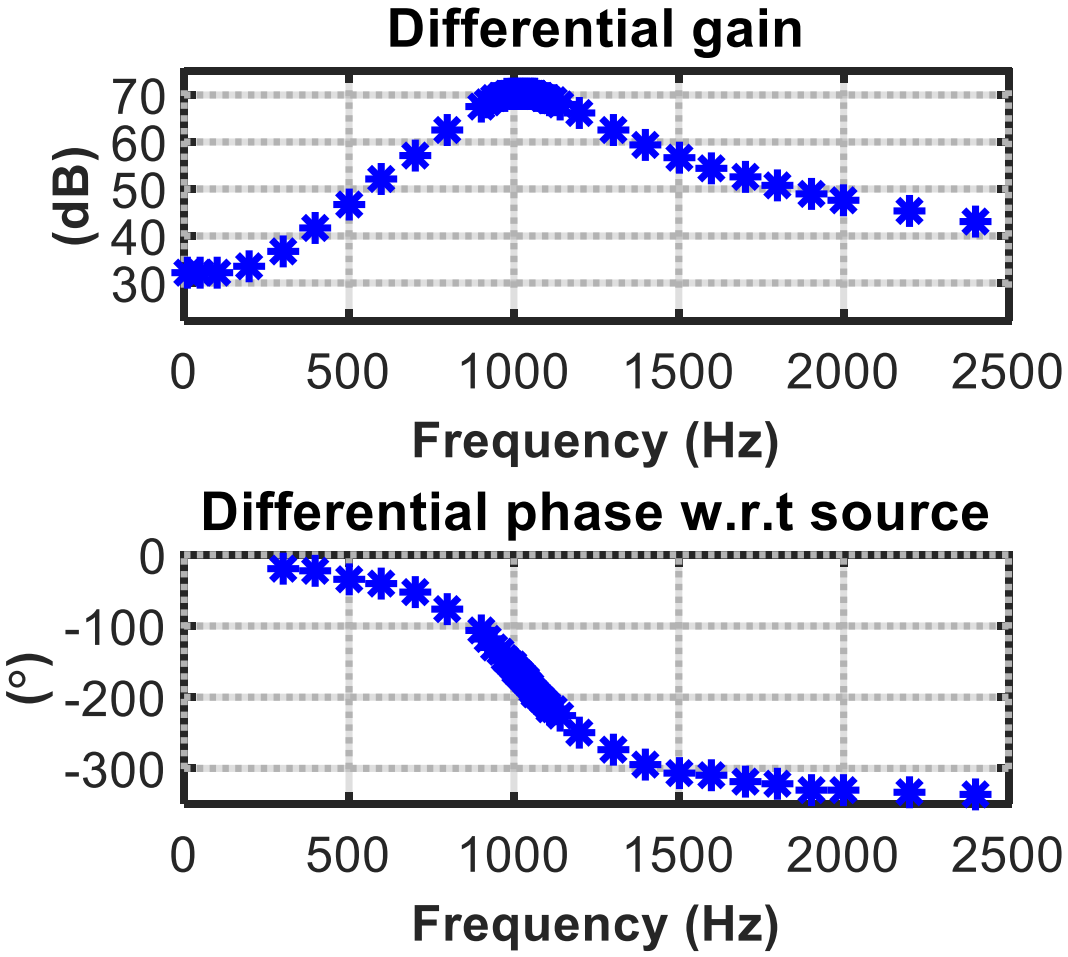

Fig. 5.6 Differential gain transfer function characterization

function characterization. The measured center frequency is at 1.02 Hz, maximum gain is 3330.33 V/V corresponding to 70.44 dB, the bandwidth is measured to be 265 Hz.

Common mode induced differential gain transfer function is also characterized and shown in Fig. 5.7. The maximum common-mode induced differential gain is -25.7 dB, which yields to a CMRR of 96.14 dB. For the practical characterization, stable common-mode voltage is provided for each differential difference amplifier (LTC6363) using a voltage regulator the value of the common-mode voltage is equal to half of the ADC full-scale reference voltage (0.6 V).

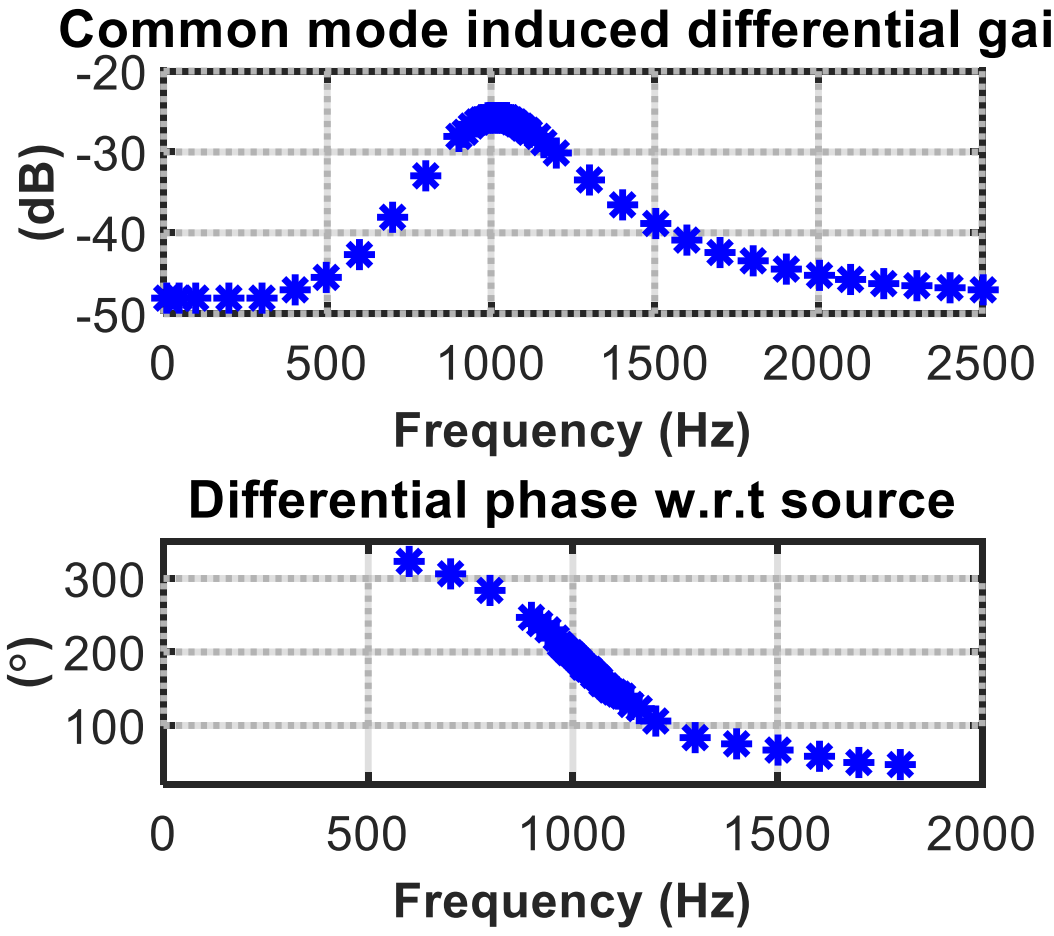

Fig. 5.7 Common mode induced differential gain transfer function characterization

5.4 Conclusions

Considering the tight accuracy requirements, while designing an interface to achieve modest 8-bit resolution for a 1% full-scale fractional transducer capacitance, many challenges arise. The differential bridge structure proposed in Chapter 4, although improving the performance, will not be effective if the differential tiny response signal at the bridge output is not acquired with sufficient accuracy. Noise is one of the most significant difficulties while amplifying such small voltages, but due to single-frequency operation, bandpass filtering effectively reduced the undesired noise. However, the required effective noise bandwidth of the filter should be decided based on both the bridge and amplification/filtering noise analysis, signal processing and binding rate considerations. Other than filtering, when dealing with a considerable differential gain after a symmetrical bridge, any mismatch effect will lead to common-mode to differential conversion, the overall system CMRR should be able to reject the common-mode interference at the smallest expected signal (8-bit) to be detected. Maintaining the symmetry of the bridge legs also is an important point while interfacing the bridge to a very high differential gain stage, while balancing the bridge common-mode to differential conversion can be avoided by matching the bridge upper legs with each other and lower legs with each other, respectively. With given design details in this chapter, an amplification and filtering board are designed, implemented and characterized. The designed board reaches a gain of 70.44 dB and a bandwidth of 265 Hz with 96.14 dB of CMRR. With this given board, an SNR level of 5 dB or less is expected at the minimum detection level.

With the very low SNR, at minimum detection limits, the data acquisition and filtering unit play an important role in resolving the tiny response signal buried in noise. The design steps for effective data acquisition and real-time processing units are given in the next chapter.

CHAPTER 6. REAL-TIME DATA ACQUISITION AND SIGNAL PROCESSING FOR BRIDGE BASED TRANSDUCTION INTERFACE

6.1 Introduction

For solution-electrode interfacial capacitance sensing, the characteristic change in the transducer impedance should ultimately be quantified. This complex impedance can be measured in real-time by extracting the amplitude and phase data from the amplified transducer's response signal. While amplitude information can be obtained using just the response signal, the phase should be measured differentially with respect to some reference signal. The excitation source signal is utilized in the current design for the differential phase measurement. This is accomplished, in the two-channel acquisition system, shown in Fig. 6.1, the ADC alternatively samples the excitation voltage (i.e., the source signal) and the output of the amplification/filtering block (i.e., the response signal).

To automate this, the digital system must be able to extract these quantities from the digitized signal. sine-fitting algorithms are traditionally seen in ADC testing and characterization [60] as well as in impedance/frequency response measurements [61], and

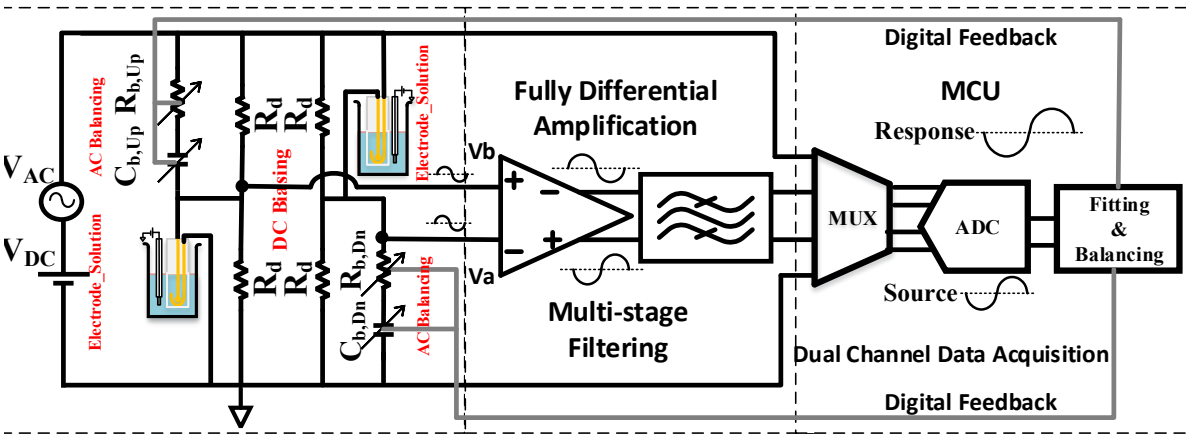

Fig. 6.1 General block diagram of differential bridge transduction based real-time amplification and filtering interface with single MCU for balancing and data acquisition/processing.

researchers have recently recognized the utility of sine-fitting algorithms for real-time processing of the transducer output voltage [33, 62].

There are many different approaches to sine-fitting, each with varying degrees of suitability in low-cost, real-time sensing applications. Sine fitting algorithms are widely used as effective methods to extract a digitized sine signal's information like amplitude, initial phase, frequency, and DC offset. As seen, for the design of an accurate sine fitting, many different parameters must be set by the designer, such as sampling rate, SNR, ADC resolution, the record length, etc… All of these parameters will affect the design parameters of the sensor interface circuitry and the overall precision and accuracy of the sensor itself. Unfortunately, these effects are often not clear, and thus, the designer must study these tradeoffs for each design.

This chapter will present a detailed analysis of the various tradeoffs for sensing requirements, and the results will help the designer pick the proper algorithm based on available budget, expected noise floor, required dynamic range, and accuracy with specific DSP hardware capabilities.

6.2 Real-Time Non-Iterative Sine-Fitting Algorithms with Non-Idealities

In general, sine fitting algorithms can be classified as either iterative or non-iterative. The iterative algorithms like the IEEE standard 4 parameter sine fitting [63], although providing better accuracy in some applications, are not the best candidates for real-time implementation, as, by nature, the convergence might require multiple iterations and data storage requirement brings about additional memory usage. Non-iterative algorithms, on the other hand, offer a better solution for real-time considering their relatively simpler implementation requirements. However, the accuracy of non-iterative approach with small and

noisy signal and compatibility of them with low-cost general-purpose microcontroller implementation needs to be considered for real-time and field-deployable applications.

With the assumption that the excitation source frequency (f_{in}) is known, and only the amplitude and differential phase extraction is targeted, two non-iterative sin parameter extraction algorithms; IEEE standard 3 parameter sine fit (3PSF) [63, 64] and ellipse fit (EF) [65] are reviewed and compared in this paper. 3PFS is performed on single-channel sine signal data for the estimation of amplitude, initial phase and the DC offset. EF algorithm requires 2 channel sine signal data for the estimation of amplitude ratio and differential phase of the channels, eliminating the need for the frequency to be known or estimated as the two channels share the same frequency. A brief introductory review of 2 non-iterative algorithms 3PFS with coherent sampling, and EF is given here.

6.2.1 3 Parameter Sine Fit

In the two-channel acquisition system, shown in Fig. 6.1, the ADC alternatively samples the excitation voltage (i.e., the source signal) and the output of the amplification/filtering block (i.e., the response signal). Consider a sequence of N samples ($k = 0, 1, .. N-1$) of a sine wave sampled at the rate of f_s for both channels. If the sine wave has a frequency f_{in}, an amplitude A_i (i, denoting response or source respectively) , an initial phase φ_i, and offset DC_i, it can be generally represented as:

$$y_i[k] = A_i \cos(2\pi \frac{f_{in}}{f_s} k + \varphi_i) + DC_i. \quad (6.1)$$

Source and response signals are derived from the same generator; therefore, they share the same frequency. The fitting algorithm is then responsible for estimates, in real-time, the amplitude of the signals, and the phase of the response signal with respect to the source signal.

If the ratio of f_{in}/f_s is known, the 3 parameters A_i, φ_i, and DC_i can be estimated for each channel, in the least-squares sense, using 3PFS [63]:

$$\begin{bmatrix} \hat{A}_{c,i} \\ \hat{A}_{s,i} \\ \widehat{DC}_i \end{bmatrix} = (D^T D)^{-1} D^T \begin{bmatrix} y_i[0] \\ y_i[1] \\ \vdots \\ y_i[N-1] \end{bmatrix} \tag{6.2}$$

where D for both channels is given to be:

$$D = \begin{bmatrix} cos(2\pi \frac{f_{in}}{f_s} 0) & sin(2\pi \frac{f_{in}}{f_s} 0) & 1 \\ cos(2\pi \frac{f_{in}}{f_s} 1) & sin(2\pi \frac{f_{in}}{f_s} 1) & 1 \\ \vdots & \vdots & \vdots \\ cos(2\pi \frac{f_{in}}{f_s} N-1) & sin(2\pi \frac{f_{in}}{f_s} N-1) & 1 \end{bmatrix}. \tag{6.3}$$

If the estimated signal, $\hat{y}_i[k]$, is expressed as:

$$\hat{y}_i[k] = \hat{A}_{c,i}\, cos(2\pi \frac{f_{in}}{f_s} k) + \hat{A}_{s,i}\, sin(2\pi \frac{f_{in}}{f_s} k) + \widehat{DC}_i \tag{6.4}$$

With some simple algebra using the coefficients $\hat{A}_{c,i}$ and $\hat{A}_{s,i}$ for each channel the amplitude and phase of y_i are estimated as [63]:

$$\hat{A}_i = \sqrt{\hat{A}_{c,i}^2 + \hat{A}_{s,i}^2} \tag{6.5}$$

$$\hat{\varphi}_i = tan^{-1}(\tfrac{-\hat{A}_{s,i}}{\hat{A}_{c,i}}). \tag{6.6}$$

6.2.2 Ellipse Fit

The ellipse fit takes advantage of two acquisition channels with mutual frequency, and by eliminating the time dependence of the sampled data from each channel, the algebraic representation of the resultant curve is [65]:

$$\left(\tfrac{y_1[k]-DC_1}{A_1}\right)^2 + \left(\tfrac{y_2[k]-DC_2}{A_2}\right)^2 - 2\tfrac{(y_1[k]-DC_1)(y_2[k]-DC_2)}{A_1 A_2} \times cos(\varphi_{diff}) - sin^2(\varphi_{diff}) = 0 \tag{6.7}$$

Where $y_1[k]$, $y_2[k]$ are the samples and A_1, A_2 are amplitude, DC_1, DC_2 are the offset for source and response and φ_{diff} is the phase difference between the channels ($\varphi_{diff} = \varphi_2 -$

φ_1) here, subscripts 1 and 2 are used for source and response respectively. If (6.7) is further simplified and written in terms of sampled data, the curve forms an ellipse as [65]:

$$ay^2{}_1[k] + by_1[k]y_2[k] + cy^2{}_2[k] + dy_1[k] + ey_2[k] + g = 0. \quad (6.8)$$

For which the ellipse constraint condition to be verified is $b^2 - 4ac < 0$. With a scaling constant the condition is forced to $b^2 - 4ac = -1$, other conditions to be met for valid ellipse fitting are non-zero amplitudes and $\varphi_{diff} \neq 0, n\pi$ where n is an integer. Solving for the coefficients in (6.8) with improved matrix-based method introduced in [66] the estimated amplitude ratio and differential phase can be obtained as:

$$\frac{\hat{A}_{response}}{\hat{A}_{source}} = \sqrt{\frac{a}{c}} \quad (6.9)$$

$$cos(\hat{\varphi}_{diff}) = -\frac{sign(a)\times b}{2\sqrt{ac}} \quad (6.10)$$

The remaining parameter to be estimated is the sign of the differential phase which can be determined based on the clockwise φ_{diff} >0) or counterclockwise (φ_{diff}<0) orientation of the constructed ellipse. Detailed equations for the voting algorithm to find the sign of φ_{diff} is given in [65].

To have a quantitative comparison of the two introduced algorithms for each algorithm, we will study the effects of the oversampling ratio of the ADC and the SNR of the signal, as well as clock jitter and computational resource requirements. The investigated performance parameters are the percent amplitude error, and percent differential phase (φ_{diff}= $\varphi_{response} - \varphi_{source}$) error. The resultant error for each algorithm is then compared to find better noise immune estimation with various sampling frequency scaling. For the subsequent analysis, we assume two sine signals with an equal frequency of 1 kHz, the amplitude of 1 V, the relative phase difference of 45°, and the same DC offset of 0.6 V, which are generated using MATLAB.

Real-time matrix implementation of 3PSF is not easily implemented in low-cost microcontrollers. The approach can be greatly simplified, however, by using coherent sampling. Coherent sampling is achieved when $f_{in}/f_s = M/N$, where M and N are relatively prime integers and represent the total number of input periods in the record and the full record length, respectively. Under the assumption of coherent sampling ($\frac{f_{in}}{f_s} = \frac{M}{N}$), the matrix $D^T D$ is diagonal, and its inverse is:

$$(D^T D)^{-1} = \begin{bmatrix} 2/N & 0 & 0 \\ 0 & 2/N & 0 \\ 0 & 0 & 1/N \end{bmatrix}. \tag{6.11}$$

Therefore, with coherent sampling, (6.2) will simplify to:

$$\begin{bmatrix} \hat{A}_{c,i} \\ \hat{A}_{s,i} \\ \widehat{DC}_i \end{bmatrix} = \begin{bmatrix} 2/N \sum_{k=0}^{N-1} y_i[k] cos\ (2\pi \frac{M}{N} k) \\ 2/N \sum_{k=0}^{N-1} y_i[k] sin\ (2\pi \frac{M}{N} k) \\ 1/N \sum_{k=0}^{N-1} y_i[k] \end{bmatrix}. \tag{6.12}$$

For a given ratio of f_{in}/f_s, the ratio of M/N remains fixed. Hence a lookup table can be used to compute the sinusoidal values associated with (6.12), dramatically reducing the required processing time. A primary concern, however, remains the effect of uncertainty in f_{in}/f_s as well as jitter in the sampling clock, f_s in the presence of very low SNR signals.

The important metric of interest in the current design is the resolution of the resulting sensor, so the pointed non-idealities and their effect on 3PSF and EF estimation are examined under this context here. The resolution of the sensor output is defined, considering a full-scale voltage at the input of the ADC, A_{FS}, and full-scale target phase difference, φ_{FS}. Therefore, if a target of 8-bit resolution is assumed to be achieved, then the estimation mean error and standard deviation should be within $\pm A_{FS}/2^8$ and $\pm \varphi_{FS}/2^8$ range. Moreover, to demonstrate a more generic reference plot, the estimation errors and resolution lines are normalized to full-

scale values. For each non-ideality effect, the normalized estimation parameters of interest with their percent mean error and percent standard deviation are shown, and normalized resolution lines are drawn on the plots as an indicator of best achievable resolution with different levels of additive noise, jitter and shift in the excitation frequency. In this way, the designer can evaluate the reasonable, achievable dynamic range for the sensor with the expected level of noise, jitter and frequency accuracy with an optimized record length for a known M/N.

The theoretical derivations of amplitude and differential phase estimation mean and standard deviation for simplified 3PSF with coherent sampling in the presence of the abovementioned non-idealities are given in the following.

6.2.3 Additive White Gaussian Noise

3PSF algorithm can effectively reduce the effect of noise on the acquired data because it behaves like an additional averaging filter if the ratio of M/N is chosen considering the effect of SNR at the lower limits of detection [67].

To see the effect of noise on the resolution of the sensor, let's assume the noise, $n_k$is additive white Gaussian noise. For a noisy coherently sampled signal,

$$y_{noisy_i}[k] = A_i cos\left(2\pi \frac{f_{in}}{f_s} k + \varphi_i\right) + DC_i + n_k, \tag{6.13}$$

the estimation parameters in (6.12) are independent and unbiased in the presence of white Gaussian noise. In this case, the expected values of the estimation parameters are: $E\left[\hat{A}_{c,i}\right] = \tilde{A}_{c,i} = A_i \cos\varphi_i$, $E\left[\hat{A}_{s,i}\right] = \tilde{A}_{s,i} = A_i \sin\varphi_i$, and $E\left[\widehat{DC_i}\right] = \widetilde{DC_i} = DC_i$. The covariance matrix, C_{noise_i}, of the 3PSF with coherent sampling and an additive white Gaussian noise with variance $\sigma_{n_i}^2$ is [67]

$$C_{noise_i} = \begin{bmatrix} \frac{2}{N}\sigma_{n_i}^2 & 0 & 0 \\ 0 & \frac{2}{N}\sigma_{n_i}^2 & 0 \\ 0 & 0 & \frac{1}{N}\sigma_{n_i}^2 \end{bmatrix}. \quad (6.14)$$

The estimated amplitude parameters, $\hat{A}_{c,i}$ and $\hat{A}_{s,i}$, in the presence of noise, are statistically analyzed and defined [48,49] with their expected values of $\tilde{A}_{c,i}$ and $\tilde{A}_{s,i}$, and equal variance $2\sigma_{n_i}^2/N$. The amplitude and initial phase $\hat{A}_i$ and $\hat{\varphi}_i$, are functions of the statistically defined random variables $\hat{A}_{c,i}$ and $\hat{A}_{s,i}$. The mean and variance of a function of two random variables $f(\hat{A}_{c,i}, \hat{A}_{s,i})$, can be approximately derived based on Taylor series expansion of the function about the expected values of associated random variables $\tilde{A}_{c,i}, \tilde{A}_{s,i}$, as shown in [66-68]

$$E\left[f\left(\hat{A}_{c,i}, \hat{A}_{s,i}\right)\right] \approx f\left(\tilde{A}_{c,i}, \tilde{A}_{s,i}\right) + \frac{1}{2}\left(\frac{\partial^2 f}{\partial \hat{A}_{c,i}{}^2} C_{11} + 2\frac{\partial^2 f}{\partial \hat{A}_{c,i}\partial \hat{A}_{s,i}} C_{12} + \frac{\partial^2 f}{\partial \hat{A}_{S,i}{}^2} C_{22}\right) \quad (6.15)$$

$$var\left[f\left(\hat{A}_{c,i}, \hat{A}_{s,i}\right)\right] \approx \left(\frac{\partial f}{\partial \hat{A}_{c,i}}\right)^2 C_{11} + 2\frac{\partial f}{\partial \hat{A}_{c,i}}\frac{\partial f}{\partial \hat{A}_{s,i}} C_{12} + \left(\frac{\partial f}{\partial \hat{A}_{s,i}}\right)^2 C_{22} \quad (6.16)$$

Using (6.15) and (6.16) the mean and variance of the estimated amplitude and initial phase can be derived in the presence of noise:

$$E\left[\hat{A}_i\right] \approx \tilde{A}_i + \frac{1}{N}\frac{\sigma_{ni}^2}{\tilde{A}_i} \approx \tilde{A}_i\left(1 + \frac{1}{2N \cdot SNR_i}\right) \quad (6.17)$$

$$var\left(\hat{A}_i\right) \approx \frac{2}{N}\sigma_{n_i}^2 \quad (6.18)$$

$$E[\hat{\varphi}_i] \approx \tilde{\varphi}_i \, , var(\hat{\varphi}_i) \approx \frac{1}{N \cdot SNR_i} \quad (6.19)$$

Based on (6.17), the amplitude estimation is biased with noise present. When alternate sampling is used, as shown in Fig. 6.1, the initial phase of the response signal is measured with reference to the source signal. Therefore, the variance of the differential phase can be derived as:

$$var\left[\hat{\varphi}_{diff}\right] = var\left[\hat{\varphi}_{response}\right] + var\left[\hat{\varphi}_{source}\right] - 2cov\left(\hat{\varphi}_{response}, \hat{\varphi}_{source}\right) \quad (6.20)$$

When the source and response signal are corrupted by additive noise, the initial phase estimations are independent (i.e., $cov(\hat{\varphi}_{response}, \hat{\varphi}_{source})$=0). From (6.19) and (6.20), if the same record length is assumed for both channels, the variance of the differential phase can be derived as:

$$var[\hat{\varphi}_{diff}] \approx \frac{1}{N}\left(\frac{1}{SNR_{response}} + \frac{1}{SNR_{source}}\right) \tag{6.21}$$

Theoretical simulations with MATLAB are carried out for the EF algorithm in the presence of additive white Gaussian noise. For 3PSF (3PSF is the coherent sampling type), simulations are carried out both numerical and based on the derived theory. For these simulations, the sampling rate, f_s, and input frequency, f_{in}, are constant and equal to 55 KS/s and 1 kHz, respectively. The values M and N, are changed providing record lengths of 256, 512 and 1024 samples with 5, 9, and 19 cycles, respectively to maintain the fixed M/N ratio.

Fig. 6.2 and Fig. 6.3 show the normalized mean amplitude and differential phase estimation error along with the associated standard deviation for response SNR ranging from -5 to 30 dB and 1000 simulations at each point for the 3PSF and EF algorithms, respectively. The SNR at the source is fixed and set to 30 dB for the simulations in Fig. 6.2 and Fig. 6.3. Apparently, with a larger record length, lower uncertainty in the estimation is achievable even for SNR values less than 0 dB. The best achievable resolution shown in Fig. 6.2 for 3PFS, is between 4 to 5 bits for both amplitude and differential phase estimation in SNR values less than 0 dB with $N = 1024$. Amplitude and phase estimations are both biased for SNRs less than 25 dB. The mean estimation error increases and leads to a lower resolution as the SNR gets worse. This shows that the EF algorithm is not at all reliable if the final sensor response at the lower detection limit is expected to have SNR even less than 0 dB.

Both algorithms were also numerically studied with varying sampling rates and low SNRs to confirm if a higher sample rate leads to better estimation performance in a noisy environment. For these numerical simulations oversampling ratios ranging from 4 to 256 and the input, SNR is assumed to range from -5 to 35 dB. Simulations for the 3PSF produce an average percent error within 1% both for the amplitude ratio and the differential phase for the 256 samples in the record.

The produced estimation results show that with lower sampling to excitation frequency ratio, 3PSF can produce reliable results at very low SNRs with even 4 samples taken per period. The more number of samples within a record generates more accurate results with worse SNR levels. However, this might place a limit on how fast result production could be at very low (sub-Hz) excitation frequencies. In [69] sit is shown that utilizing 3PSF for a sub-Hz sensor response, can produce an impedance estimation variance of 1% while the record covers only

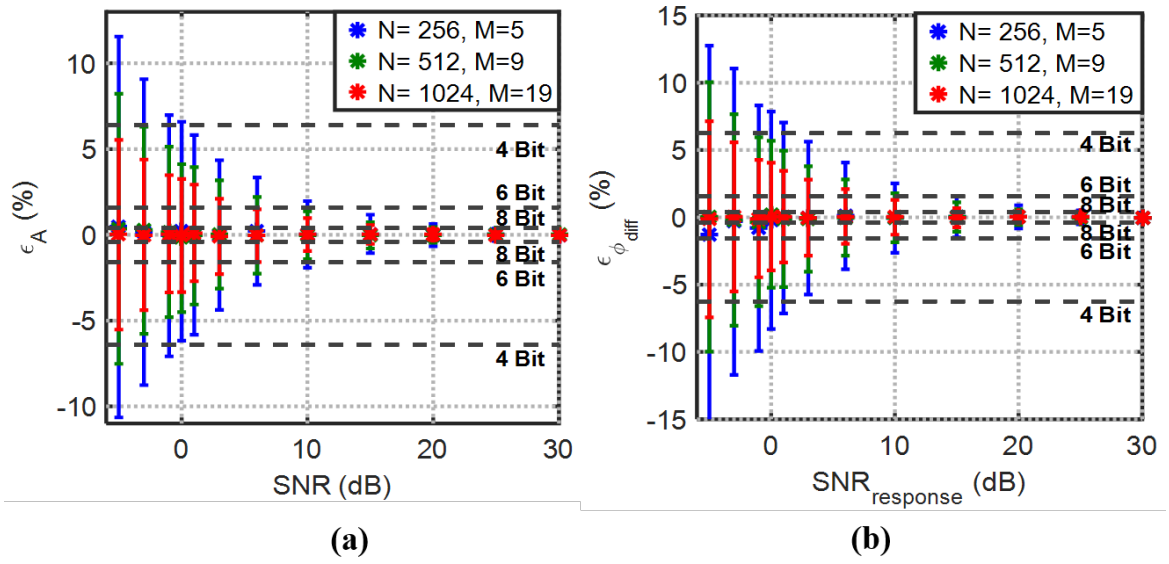

Fig. 6.2 3PSF (a) percent mean amplitude and (b) differential phase estimation errors with their normalized standard deviations (error-bars) vs. SNR

11% of the whole period. This makes 3PSF design flexible for various excitation frequencies and signal to noise ratios.

EF behavior is largely affected by decreasing SNR, the average amplitude and phase errors are still strongly biased for SNR values less than 30 dB, because the ratio of the amplitudes is directly being estimated with EF algorithm, the relative SNR of the two channels would affect the average amplitude ratio error, but the differential phase average error is constantly degrading with lower SNR values. EF requires at least 6 samples per period to produce more accurate results at even moderate SNRs. A change is observed in the polarity of differential phase estimation error for the EF at higher sampling rates and low SNR values (also addressed in [65]), which stems from the voting algorithm failure in determination of ellipse orientation ([64]located samples at low SNR increase the probability of incorrect voting). Therefore, 3PSF with coherent sampling provides more accurate results without requiring higher sample rates at low SNRs compared to EF.

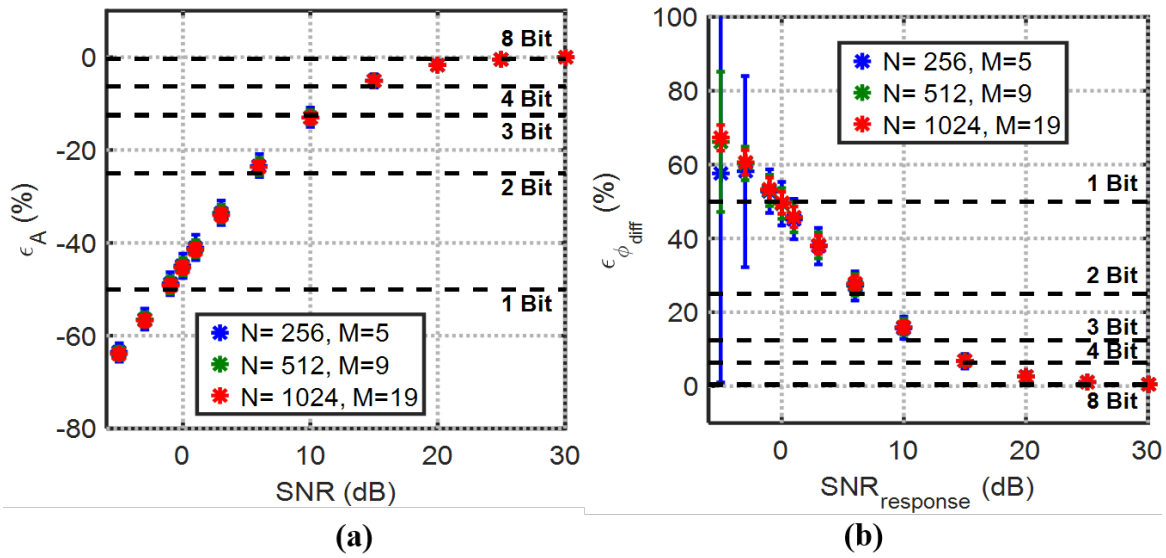

Fig. 6.3 EF (a) percent mean amplitude and (b) differential phase estimation errors with their normalized standard deviations (error-bars) vs. SNR

6.2.4 Sampling Clock Jitter

Sampling clock jitter causes uncertainty in 3PFS and EF estimation results. The uncertainty caused by sampling clock jitter can be modeled as a normally distributed random variable $\alpha_{i,k}$ with zero mean and standard deviation equal to σ_{α_i} . A coherently sampled signal with jitter is modeled as,

$$y_{jitter_i}[k] = A_i cos\big(2\pi f_{in}\big(t_k + \alpha_{i,k}\big) + \varphi_i\big) + DC_i = A_i cos\big(2\pi f_{in} t_k + \theta_{i,k} + \varphi_i\big) + DC_i \quad (6.22)$$

where $\theta_{i,k}$ is a normally distributed random variable with zero mean and standard deviation $2\pi f_{in}\sigma_{\alpha_i} = \sigma_i$. In the presence of jitter, the 3PSF is no longer an unbiased estimator for $\hat{A}_{c,i}$ and $\hat{A}_{s,i}$, the expected values for the 3 parameters are:

$$E\big[\hat{A}_{c,i}\big] = A_i e^{\frac{-{\sigma_i}^2}{2}} cos\,\varphi_i, \quad (6.23)$$

$$E\big[\hat{A}_{s,i}\big] = -A_i e^{\frac{-{\sigma_i}^2}{2}} sin\,\varphi_i, \quad (6.24)$$

$$E\big[\widehat{DC}_i\big] = DC_i. \quad (6.25)$$

If the initial phase, φ_i, is assumed to be constant, the covariance matrix of the estimator in the presence of jitter, C_{jitter_i}, is derived (6.26).

$$C_{jitter_i} = \begin{bmatrix} \frac{{A_i}^2}{N}(1 - e^{-{\sigma_i}^2})(1 - \frac{1}{2}e^{-{\sigma_i}^2}\cos 2\varphi_i) & 0 & 0 \\ 0 & \frac{{A_i}^2}{N}\big(1 - e^{-{\sigma_i}^2}\big)\big(1 + \frac{1}{2}e^{-{\sigma_i}^2}\cos 2\varphi_i\big) & 0 \\ 0 & 0 & \frac{{A_i}^2}{N}\big(1 - \frac{1}{2}e^{-{\sigma_i}^2}\big) \end{bmatrix} \quad (6.26)$$

The approximate mean and variance of amplitude and initial phase estimation with jitter present, using (6.15) and (6.16) are:

$$E\big[\hat{A}_i\big] \approx A_i e^{\frac{-{\sigma_i}^2}{2}} + \frac{A_i}{2N}(1 - e^{-{\sigma_i}^2})(e^{\frac{{\sigma_i}^2}{2}} + \frac{1}{2}e^{\frac{-{\sigma_i}^2}{2}}) \quad (6.27)$$

$$var\big(\hat{A}_i\big) \approx \frac{{A_i}^2}{N}(1 - e^{-{\sigma_i}^2})(1 - \frac{1}{2}e^{\frac{-{\sigma_i}^2}{2}}) \quad (6.28)$$

$$E[\hat{\varphi}_i] \approx \tilde{\varphi}_i \ , \ var(\hat{\varphi}_i) \approx \frac{1}{N}(1 - e^{-{\sigma_i}^2})(e^{{\sigma_i}^2} + \frac{1}{2}). \quad (6.29)$$

In the presence of jitter, the estimations for source and output initial phases are independent, i.e., $cov(\hat{\varphi}_{response}, \hat{\varphi}_{source}) = 0$. The differential phase variance is derived using (6.20) and (6.30):

$$var[\hat{\varphi}_{diff}] \approx \frac{1}{N}\{(1 - e^{-{\sigma_{source}}^2})(e^{{\sigma_{source}}^2} + \frac{1}{2}) + (1 - e^{-{\sigma_{response}}^2})(e^{{\sigma_{response}}^2} + \frac{1}{2})\} \quad (6.30)$$

The approximate expression for the differential phase variance given in (6.30) is the sum of the source and response initial phase variances.

Based on derivations and numerical simulations, the mean of the amplitude and differential phase errors with their normalized standard deviations for 1000 simulations at each point is plotted in Fig. 6.4 and Fig. 6.5 as a function of jitter standard deviation up to 2π for 3PSF and EF, respectively. If we examine the mean error in the estimated amplitude using (6.27):

$$\lim_{N\to\infty} \varepsilon_{A_i} = e^{\frac{-{\sigma_i}^2}{2}} - 1 \quad (6.31)$$

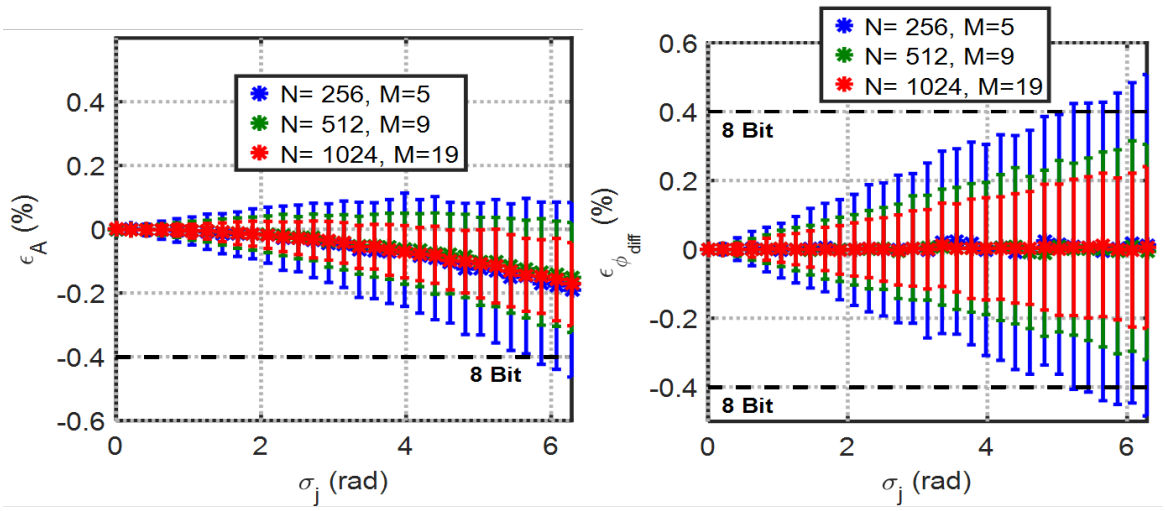

Fig. 6.4 3PSF (a) percent mean amplitude and (b) differential phase estimation errors with their normalized standard deviations (error-bars) vs. jitter standard deviation

Although it is seen in (6.31) that the amplitude mean error will never go to zero for 3PSF which is also claimed in [70], but with a record length of 1024, 8-bit detection resolution for both amplitude and phase is achievable even at non-realistically high jitter standard deviation of around π radians. Fig. 6.5 shows a similar numerical simulation with sampling clock jitter for EF. While amplitude estimation error is within target 8-bit resolution for the EF, even at large jitter standard deviations, the differential phase estimation is strongly biased and affected by jitter. Based on obtained results, 3PSF can maintain the target 8-bit resolution at even jitter standard deviations close to 2π radians, by controlling the record length.

It is worth mentioning here that the obtained results for this analysis are dependent on the source and sampling frequency. The maximum allowable jitter using an ADC with a resolution of R bits, and a sine wave input with an amplitude equal to the ADC full-scale and frequency of f_{in}, to have a jitter induced error of less than half LSB is inversely proportional

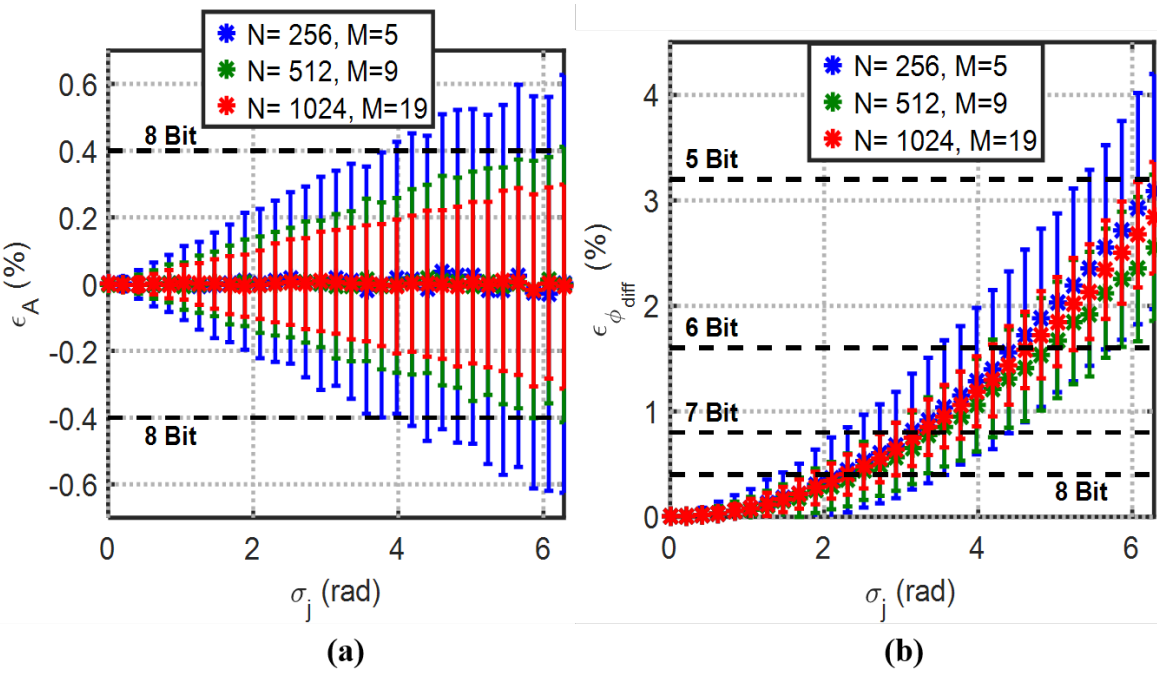

Fig. 6.5 EF (a) percent mean amplitude and (b) differential phase estimation errors with their normalized standard deviations (error-bars) vs. jitter standard deviation

to $(2\pi f_{in}2^R)$. The maximum allowable jitter, therefore, gets smaller if the sine wave has an amplitude lower than full scale, higher frequency, and higher resolution for the ADC. As an example, jitter considerations gain more importance for sensors with hundreds of MHz or GHz level excitation frequencies or when the response signal is not sufficiently amplified to the full-scale range of the ADC, which is specifically the case at lower detection limits using fixed overall amplification gain.

6.2.5 Non-Coherency

A fundamental assumption while simplifying the implementation of the real-time 3PSF algorithm is that the data belongs to a coherently sampled sine wave. Depending on the accuracy level of the source sine wave generator, however, the desired source frequency may deviate from its actual value. The result will be that the record will not contain exactly M cycles of the input signal, and the look-up table for computing (6.12) will no longer represent correct samples leading to errors in the estimated amplitude and initial phase.

The effect of the shift in the source frequency can be modeled by assuming a shift in the f_{in} such that [67]:

$$\Delta f = f - f_{in} = \frac{(Q.\delta)f_s}{N} \tag{6.32}$$

Where Q is the integer part, and δ is the fractional part of the residue. The result is a shift in the number of periods sampled. Now, $M' = M + Q.\delta$ and the actual waveform can be expressed as:

$$y_{dev_i}[k] = A_i\, cos(2\pi \frac{M+Q.\delta}{N} k + \varphi_i). \tag{6.33}$$

Using (6.9) and (6.12) the amplitude is estimated as:

$$\hat{A}_i(Q.\delta) = \{[2/N\sum_{k=0}^{N-1} A_i\, cos(2\pi\frac{M+Q.\delta}{N}k + \varphi_i)\, cos(2\pi\frac{M}{N}k)]^2 + [2/N\sum_{k=0}^{N-1} A_i\, cos(2\pi\frac{M+Q.\delta}{N}k + \varphi_i)\, sin(2\pi\frac{M}{N}k)]^2\}^{1/2} \quad (6.34)$$

which can be further simplified as a function of Δf to be:

$$\hat{A}_i(\Delta f) = A_i[sinc^2(N\frac{\Delta f}{f_s} + 2M) + sinc^2(N\frac{\Delta f}{f_s}) + 2sinc(N\frac{\Delta f}{f_s} + 2M)sinc(N\frac{\Delta f}{f_s})\, cos(2\varphi_i + 2\pi N\frac{\Delta f}{f_s})]^{1/2}. \quad (6.35)$$

The initial phase estimation, as a function of $Q.\delta$, can be derived using (6.10) and (6.6):

$$\hat{\varphi}_i(Q.\delta) = tan^{-1}(\frac{-2/N\sum_{k=0}^{N-1} A_i\, cos(2\pi\frac{M+Q.\delta}{N}k + \varphi_i)\, sin(2\pi\frac{M}{N}k)}{2/N\sum_{k=0}^{N-1} A_i\, cos(2\pi\frac{M+Q.\delta}{N}k + \varphi_i)\, cos(2\pi\frac{M}{N}k)}) \quad (6.36)$$

which can be further simplified and written as a function of frequency deviation, Δf:

$$\hat{\varphi}_i(\Delta f) = tan^{-1}[tan(\varphi_i + \pi N\frac{\Delta f}{f_s})\frac{tan(\pi\frac{f_{in}}{f_s})}{tan(\pi\frac{\Delta f}{f_s} + \pi\frac{f_{in}}{f_s})}]. \quad (6.37)$$

Fig. 6.6(a) shows the normalized amplitude estimation with deviation in source frequency. For higher numbers of samples, with approximately equal input frequencies and a constant sampling rate, the system becomes much more sensitive to uncertainty in the ratio of f_{in}/f_s. Fig. 6.6(b) shows the zoomed-in plot of amplitude error with non-coherency, for $N = 1024, M = 19$. It is seen that for 8-bit detection resolution, a shift of approximately 5 Hz can be tolerated, and if the resolution is relaxed to 4 bit, a shift of 22 Hz can be tolerated. With the typical accuracy level of on-chip sine wave generators utilizing PLLs or DDS for discrete implementation, at kHz range this amount of non-coherency is not a concern for amplitude

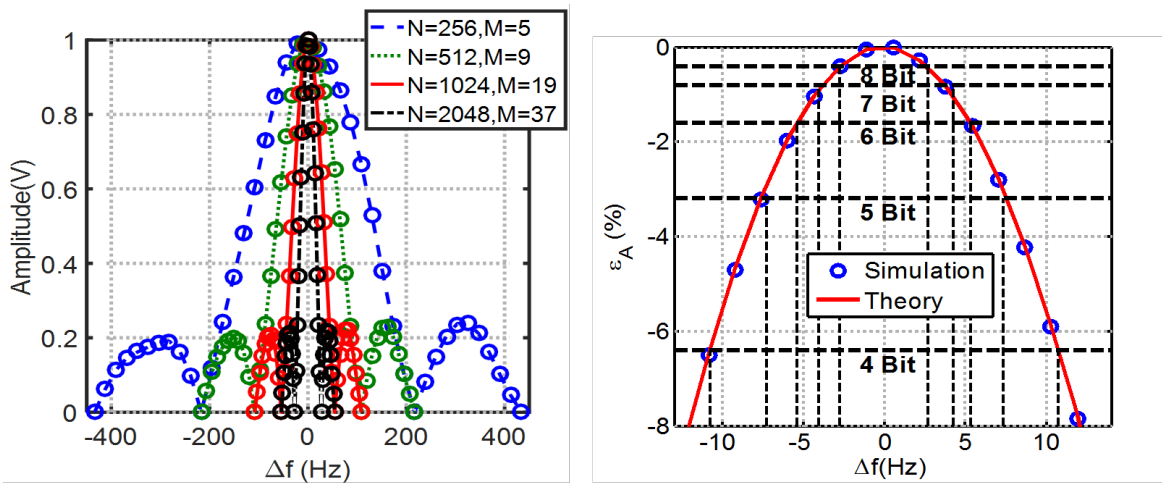

(a) (b)

Fig. 6.6 3PSF (a) amplitude estimation (b) zoomed-in Mean amplitude percent error and normalized percent detection resolutions, vs. source frequency deviation

estimation. However, at MHz or GHz range, the accuracy of the generated sine wave is more of a limiting factor while picking the record length.

As also discussed in earlier sections, the differential phase is measured in the two-channel system of Fig. 6.1. The theoretical and numerically simulated initial phase estimation of source and response with non-coherency are shown in Fig. 6.7. A deviation in the source

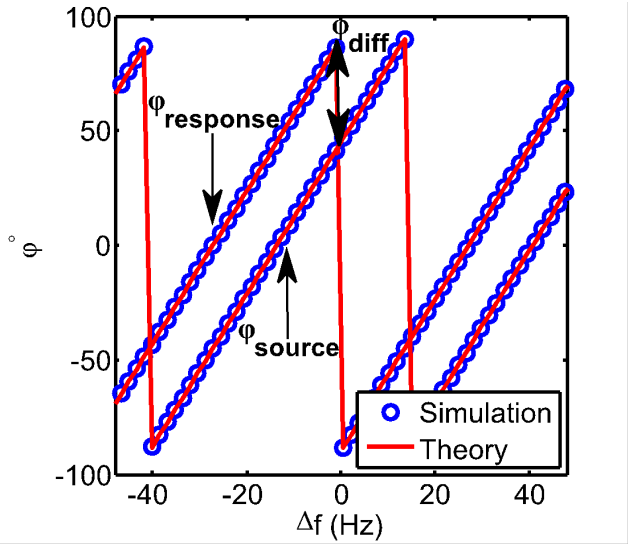

Fig. 6.7 3PSF initial phase estimation vs. source frequency deviation for $\varphi_{source} = 45°$, $\varphi_{response} = 90°$

frequency will result in a linear increase in the initial phase, but the slope of this change, as derived in (6.37), is equal for both source and response signals, as they are sharing a mutual source frequency.

Therefore, the resultant differential phase will not be affected by frequency deviation for any record length. It should be pointed out that, as seen in Fig. 6.6(a), the estimated amplitude will go to zero when $\delta = 0$ (i.e., when $\Delta f = \frac{Q}{N} f_s$), causing a discontinuity in the initial phase estimation at the same points. The shift in frequency effect is not considered for EF performance evaluation here because the two channels are supposed to share a mutual frequency; therefore, any shift appears in both channels leaving the results unaffected.

6.2.6 Real-Time Processing Requirements

Real-time dual-channel implementation requirements of the introduced algorithms are compared in Table I. For real-time implementation. Each algorithm needs to perform some mathematical operations on the taken individual samples from each channel and store the results in specific variables and update it by each incoming sample. The related implementation cost is, therefore, compared in the context of the required number of mathematical operations, functions, lookup tables, and the number of memory positions needed to hold the variables, per fixed number of data within a record. Final amplitude and differential phase calculation based on the updated variables, after real-time acquisition and processing of the samples within one record is not included for any of the algorithms in Table 6.1.

While the trigonometric function and square root calculations to produce final results could be implemented with lookup tables for lower computational time for all the algorithms, the EF algorithm requires additional matrix operations to solve the coefficients equation (6.8). According to Table 6.1, one can estimate the execution time of each record within the real-

time loop in the algorithm code based on the number of clock cycles required for each specific math operation. Based on the known excitation frequency assumption, values of $\sin(2\pi f_{in} t_k)$ and $\cos(2\pi f_{in} t_k)$ can be pre-computed, and a singular look-up table would produce both sin and cos values for the 3PSF.

The "arg" and "sign" functions are required for the EF. However, a look-up table would make it faster to execute the "arg" function. Based on the numerical simulations and also information from Table. 6.1, 3PSF maintains better accuracy compared to EF at low SNRs and with lower samples taken per cycle. Table. 6.1 also suggests that 3PSF can be implemented with lower computational cost in comparison. Therefore 3PSF offers a better solution in dealing with accuracy and complexity challenges discussed earlier.

Tabel 6.1 Real-time dual-channel implementation requirements of the 2 introduced algorithms

Algorithm	Variable count	Mathematical operation count		Function	Required look-up table count
3PSF	6	×	4	sin, cos	1
		+	6		
EF	17	×	14	arg, sign	1
		+	19		

6.2.7 Discussion

At the lower limits of detection for most of the sensors that with very small full-scale target change, the resolution is mainly affected by the noise level. Additionally, when the sensor response is still small and comparable to the noise level even after amplification, clock jitter will also induce some noise and degrade the SNR. Therefore, for better performance in expected low SNRs (even SNR < 0 dB), higher record length for coherent sine fitting is

suggested while keeping an eye on the sensitivity to the ratio of f_{in}/f_s. It is also shown here that a shift in the source frequency and sampling clock jitter will affect the estimated amplitude at any detection resolution while the differential phase is not degraded by the non-coherency effect using the alternate sampling method. However, with typical accuracy levels of sine generation and the fact that both sampling clock and source signals are driven by a single sinusoidal source in most cases, jitter and source frequency shift will have a minor effect on the detection resolution both in terms of amplitude and differential phase.

Real-time processing of the data obtained from the sensor will eliminate the need for data storage and memory requirements and lead to lower cost of the overall system. A less complex data processing algorithm with lower memory requirements, such as 3PSF, facilitates the use of the same microcontroller for bridge digital balancing and calibration algorithms.

6.3 Board Sensitivity Test for Capacitance Change

The bridge based transduction and interface readout system shown in Fig. 6.1 is designed with the guidelines given in Chapters 4-5. Fig. 6.8 shows the implemented board with the bridge transduction and first differential amplification stage, 2 stage amplification, and filtering, and the digital data acquisition and sin fitting with the TI MSP-EXP432P401R responsible for the balancing too.

Record length of 1024, is picked for the design, both considering the expected SNR of approximately $8\ dB$ or less, with a filter $ENB \approx 250\ Hz$, and the maximum microcontroller master clock rate of $48\ MHz$. The $14\ bit$, $1.2\ V$ full scale, differential ADC samples the $1.03\ kHz$ source and response signals at $55\ KS/s$ sampling rate. The ADC alternatively samples the response and source channels, and writes the data to dedicated ring buffers while the processor continuously reads the ring buffers and applies coherent 3PSF, to every 19 cycles

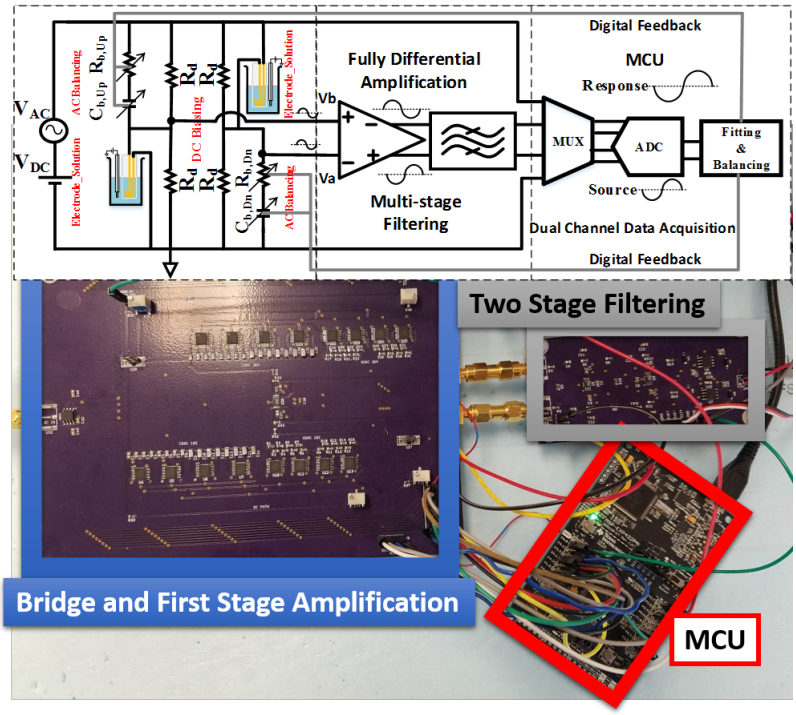

Fig. 6.8 implemented board with the bridge transduction and first differential amplification stage, 2 stage amplification and filtering and the digital data acquisition and sin fitting with the TI MSP-EXP432P401R

of the signals. In this way, the resultant magnitude and differential phase of the two channels are available in real-time for series RC electrode-solution interface characterization.

Sensitivity and capacitive change measurement accuracy of the series-RC balancing is validated using the same setup shown in Fig. 6.9. After balancing the bridge for DC and with solutions bias adjusted to the DC potential at the balanced DC voltage of the working electrodes, AC balancing is performed. The capacitance array $C_{b,Dn}$ is then changed in binary-weighted steps (8-bit) up to the total of 1% fractional change in the capacitance value at the initial balance point (this is done with an additional MCU manually for the experiment). For the $200\,nF$ initial capacitance value, the capacitance change steps are nominal,$16\,pF, 32\,pF, 64\,pF, 128\,pF,\ 32\,pF, 64\,pF, 128\,pF,\ 256\,pF,\ 512\,pF,\ 1024\,pF,$

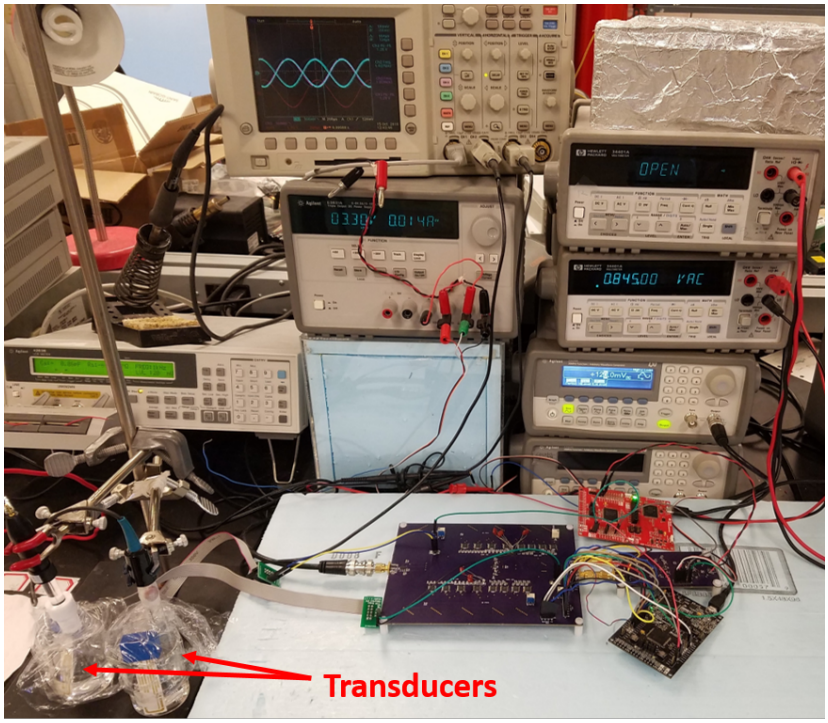

Fig. 6.9 Sensitivity and capacitive change measurement accuracy, experimental setup

and 2048 pF, this is supposed to mimic the change in working electrode-solution capacitance $C_{el,Dn}$, with target binding.

Phase behavior with capacitance change can be indicative of the type of initial imbalance. For example, if there is initially a phase change with $C_{b,Dn}$, changing, then there is an initial resistive imbalance in the bridge based on (4.9). With the known balancing array values at the initial balance point, the initial possible resistance and/or capacitance mismatch can be calculated using (4.10) and (4.11). Fig. 6.10, shows the sensitivity analysis for a 1% fractional capacitive change on $C_{b,Dn}$, where the measured capacitance $\Delta C_{measured}$ change is plotted vs. each corresponding manually adjusted binary-weighted capacitance change $\Delta C_{nominal}$.

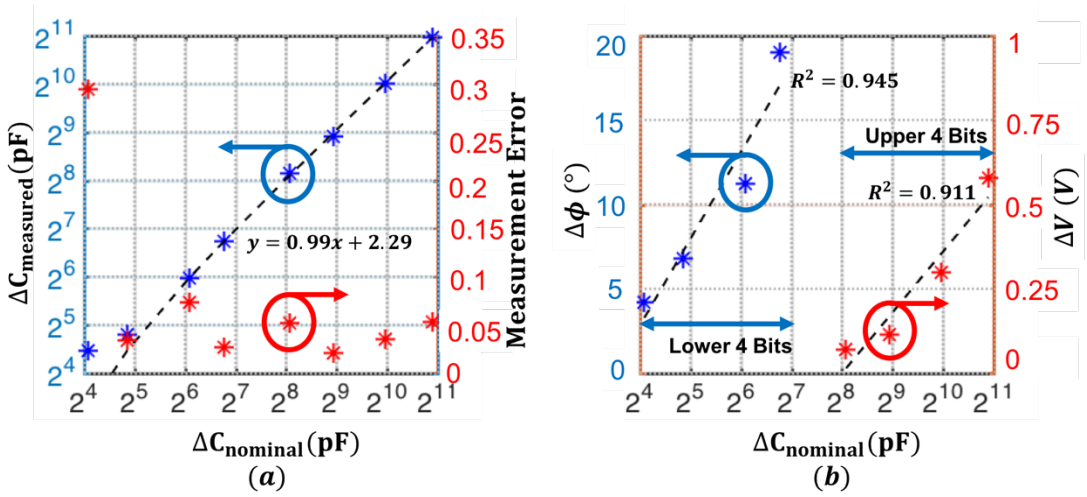

Fig. 6.10 (a) 8-bit $\Delta C_{measured}$ vs. $\Delta C_{nominal}$, calculated using magnitude and phase change transfer functions, (b) phase $\Delta\phi$ and magnitude ΔV change vs. $\Delta C_{nominal}$, phase is linear at lower 4 Bits and magnitude is linear at higher 4

The measured magnitude and phase change at each $\Delta C_{nominal}$, is mapped to a corresponding $\Delta C_{measured}$, the bridge transfer functions (4.10) and (4.11). Given the initial bridge imbalance and the fact that mainly the capacitance is changing manually, the initial resistance mismatch is calculated using the changing phase information and assumed to stay constant during the experiment. As shown in Fig. 6.10(b), the lower 4-bits of detection range is quantified more clearly using the differential phase from (4.11) and upper 4-bits with the apparent magnitude change using (4.10). The linear fit to $\Delta C_{measured}$ vs. $\Delta C_{nominal}$ shown in Fig. 6.10(a) has linearity with a slope of 0.99 and the coefficient of determination $R^2 = 0.999$. The measurement error is the absolute difference between $\Delta C_{measured}$ and $\Delta C_{nominal}$ divided by $\Delta C_{nominal}$ as shown in (6.38) and remains below 0.5 at each point. The characterization result indicates that by utilizing fine-tuning arrays and both magnitude and phase data, the differential setup shown in Fig. 6.1 can successfully detect a 1% fractional capacitance change at the interface, with an 8-bit resolution.

$$\text{Measurment Error} = \frac{|\Delta C_{measured} - \Delta C_{nominal}|}{\Delta C_{nominal}} \tag{6.38}$$

6.4 Conclusions

Other than the careful design requirements for the amplification/filtering read-out interface after bridge transduction, the very small detection signals that are expected to have SNR values less than 1 to 5 dB even after filtering, brings about the necessity to think of an effective signal acquisition and processing method that is capable of extracting data from a signal even buried in noise. To make it more challenging by the application demands, the acquisition and processing need to be done in real-time!

Here, coherent 3PSF as a powerful non-iterative algorithm is adopted for implementation within a simple microcontroller to both satisfy the low cost and real-time requirements. The detailed design assumptions and practical considerations in the presence of non-idealities are given for the design of coherent 3PSF that can be effective in very low SNR levels. Design, implementation and performance verification of the acquisition and processing unit is the last stage before making sure that the system is potentially sufficient to detect MCLR. In the next chapter, the experimental measurement results with MCLR using the designed biosensor are demonstrated.

CHAPTER 7. SYSTEM FABRICATION AND MEASUREMENT

7.1 Experimental Measurements with the Bridge Transduction Based Biosensor for Detecting MCLR

The experimental setup for actual MCLR toxin detection with the designed portable biosensor is shown in Fig. 7.1(a). The bridge is configured the same as the block diagram shown in Fig. 4.1, the transducer under test is an MCLR-antibody factionalized electrode with the steps explained in Chapter 3. The transducer under test is placed in a costume designed flow chamber Fig. 7.1(b) with approximately 1.6 cm^3 volume. The flow chamber has an inlet and an outlet for injecting solution and waste exit, and two spacing on the sides for the transducer chip and external Ag/AgCl reference electrode to slide into the chamber. The chamber is carefully sealed after inserting the electrodes so that the waste only gets out through the outlet.

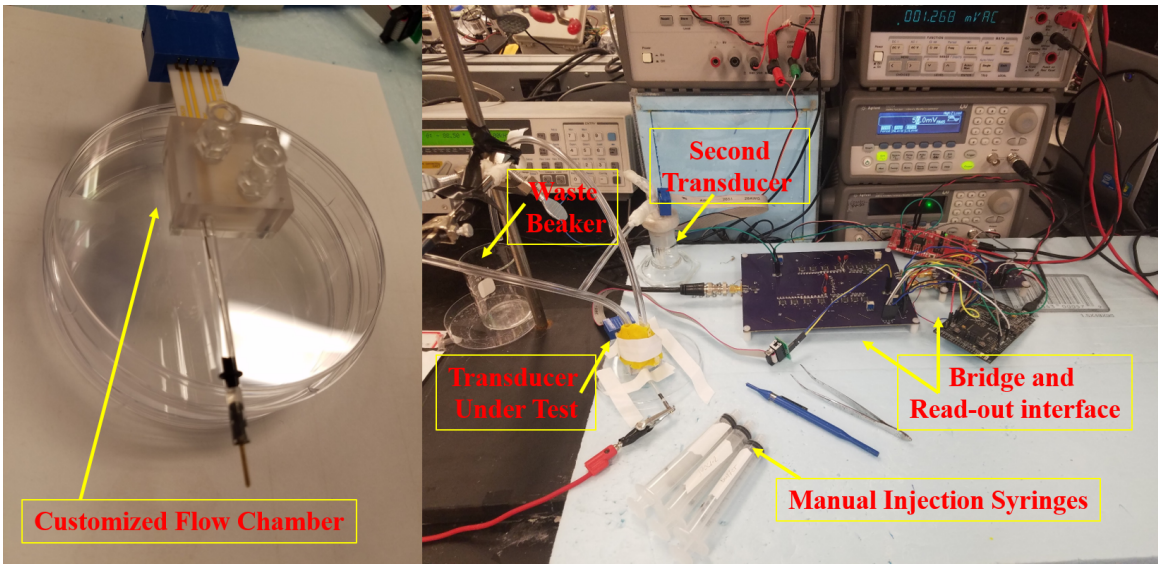

(a) **(b)**

Fig. 7.1 (a) Customized flow chamber compatible with the purchased gold patterned transducers (b) The experimental setup for actual MCLR toxin detection with the designed portable biosensor.

For these measurements, the toxin will only be injected into the flow chamber, and the secondary functionalized transducer at the upper bridge leg is placed inside a biased solution for maintaining differential measurement strategy and help reduce the common-mode interference effects mutual between the transducers. Both solutions at the upper and lower bridge legs are biased at the same level as the working electrodes DC bias levels ($60\ mV$) for drift suppression.

The transducers are both placed in the PBS buffer solution and wait connected to the setup for approximately one hour before balancing; this is required for the solutions to equilibrate. The more stable the transducers in the solution, the less challenging the balancing will be. The bridge balance is carried out with the balancing algorithm introduced in Chapter 4 (Fig. 4.6). After obtaining a balance condition for the bridge, the interface output is observed for any required rebalance, and once a stable and low drift signal is observed, the actual experiment starts.

MCLR diluted solutions are prepared using PBS 1X as the base solution; the target toxin concentrations for experimentation are $0.1\ \mu g/L$, $1\ \mu g/L$ and $10\ \mu g/L$. The experiment will start by injecting $10\ ml$ of, $0.1\ \mu g/L$ MCLR solution with a flow rate of roughly $3\ ml/min$, through the inlet. The injection process causes spikes in the response; therefore, the next experiment step will start after the response signal gets to a settled state. Once a stable signal is observed, the second and third MCLR concentration is injected with a similar procedure.

During the experiment, the MCU acquires the response signal, and after coherent sine fitting, the amplitude and phase data are available for solution-electrode interface capacitance

and resistance parameter extraction. Table 7.1 shows the calculated percent fractional interface capacitance, and resistance change values at the initial PBS buffer start step and with increasing MCLR concentrations. The values reported in Table 7.1 are obtained from the final settled state data. The results show that as a proof of concept, the bridge transduction based capacitive biosensor with a very sensitive read-out interface is capable of detecting MCLR concentrations with distinct detection levels for capacitance and resistance values.

Interestingly, the change observed in both capacitance and resistance of the interface reveals that the difference in the interface resistance values is detected as the solutions are changed during the experiment. A statistical evaluation of the collected results is not provided here because the data is collected from separate electrodes at each experiment.

Table 7. 1 The transducers final settled overall fractional capacitance and resistance change values for the initial buffer and set of 3 MCLR solutions with increasing concentration levels

Transducer: Fractional change		**PBS**	**0.1 µg/L**	**1 µg/L**	**10 µg/L**
Tr.1	**Tr. 1:** $\frac{\Delta C_{el,Dn}}{C_{el,Dn}}$ (%)	0.07	0.39	0.7	0.61
	Tr. 1: $\frac{\Delta R_{el,Dn}}{R_{el,Dn}}$ (%)	0.1	1.5	2.35	2.75
Tr.2	**Tr. 2:** $\frac{\Delta C_{el,Dn}}{C_{el,Dn}}$ (%)	0.03	0.15	0.58	1.34
	Tr. 2: $\frac{\Delta R_{el,Dn}}{R_{el,Dn}}$ (%)	0.02	0.96	2.37	4.7
Tr.3	**Tr. 3:** $\frac{\Delta C_{el,Dn}}{C_{el,Dn}}$ (%)	0.046	0.1	0.52	0.63
	Tr. 3: $\frac{\Delta R_{el,Dn}}{R_{el,Dn}}$ (%)	0.0075	0.7	0.16	-0.27
Tr.4	**Tr. 4:** $\frac{\Delta C_{el,Dn}}{C_{el,Dn}}$ (%)	0.044	1.08	1.22	1.86
	Tr. 4: $\frac{\Delta R_{el,Dn}}{R_{el,Dn}}$ (%)	0.12	-1	-1.2	-1.82

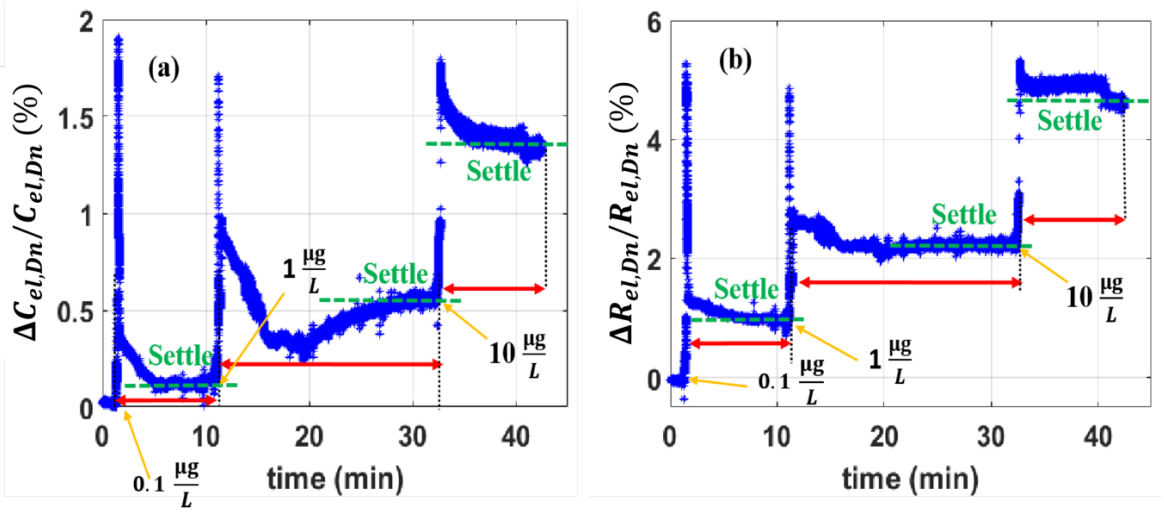

Fig. 7. 2 Raw real-time extracted fractional transducer (a) capacitance and (b) resistance percent change, showing the settled states after injection at each MCLR concentration for the experiment with the transducer Tr.2

Fig. 7.2 shows the raw real-time extracted fractional transducer capacitance and resistance percent change ($\frac{\Delta C_{el,Dn}}{C_{el,Dn}}, \frac{\Delta R_{el,Dn}}{R_{el,Dn}}$) utilizing the known balanced state parameters with equations (4.10) and (4.11) for transducer Tr.2. The results show that settled state values of the resistance and capacitance change, give distinct detection levels at each MCLR concentration and this is a proof of concept, even with the maximum full-scale change of capacitance in the experiment remaining below 1.5%.

Fig. 7.3 shows the raw extracted real-time capacitance and resistance fractional change amounts plotted for the set of 4 transducers Tr.1-Tr.4. The increase or decrease in the resistance and capacitance for all the transducers follows a uniform trend. The capacitance or resistance fractional change either shows an increasing or decreasing trend with the consecutive concentrations.

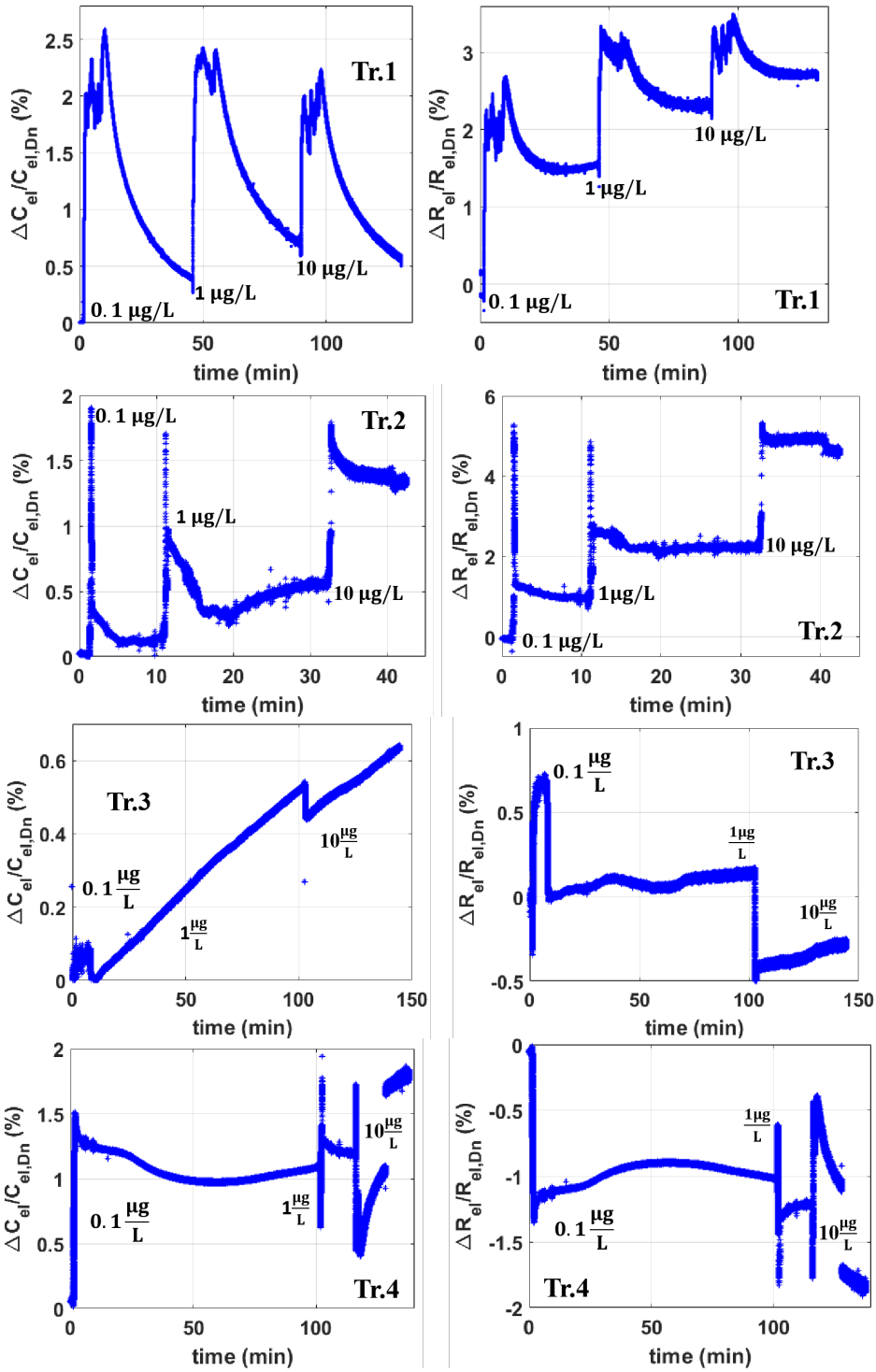

Fig. 7.3 Raw real-time extracted fractional transducer capacitance and resistance percent change ($\frac{\Delta C_{el,Dn}}{C_{el,Dn}}, \frac{\Delta R_{el,Dn}}{R_{el,Dn}}$) for experimental measurements with 4 set of electrodes Tr.1-Tr.4.

7.2 Conclusions

The experimental setup design for differential sensing of MCLR with the developed bridge-based capacitive read-out interface is shown in this chapter. The drift rate is effectively controlled with the DC bias application both to the working electrodes and solution. With the controlled drift rate the real-time detection of MCLR and exploring the binding dynamics is made possible. The obtained real-time interface capacitance and resistance change are both on the order of couple percent in general for the total range of utilized concentrations. The primary advantages of this setup is that distinct detection levels with settled values are achievable at most of the experiments. The experimental results reveal that both resistance and capacitance change values can used for detection. The solution resistance shows a higher change compared to the percent change in the interface capacitance. This change can be studied in more detail to find out the potential factors impacting the solution resistance during experiment, for example the slight difference in the pH values of different solutions. This experimental validation shows that using the capacitance change levels obtained after injecting the MCLR into the flow chamber, concentrations as low as 0.01 $\mu g/l$ can be detected.

CHAPTER 8. GENERAL CONCLUSIONS

As part of the biosensor development process, a low-cost, simple, fully differential capacitive bridge based readout interface is designed, implemented and characterized in this work. The design goal is to achieve an 8-bit resolution for sensing a fractional capacitance change of roughly 1%. Differential bridge structure with two transducers is employed, and digitally controlled series RC networks are utilized for balancing. Fully differential amplification along with bandpass filtering is carried out to fight against noise and common mode interference and amplify the response signal to meet the ADC reference voltage at the expected full scale. Characterization results show that the readout interface achieves the target 8-bit resolution.

The data acquisition unit is designed based on the dual-channel operation to acquire amplitude and differential phase of the response and source signals. Data acquisition and sine fitting are both proposed to be carried out using a single microcontroller. The main criteria to fulfill while designing the data acquisition and processing unit are low-cost (< 10$), real-time and no need for complicated post-processing of the data.

Optimized setup and bias and experiment conditions are investigated and an effective method specifically for drift control while acquiring real-time data is shown. Amplification/filtering board and the data acquisition and processing units are carefully characterized. In this way, the data obtained from the actual experiment can be interpreted more reliably knowing that the read-out unit performance is as expected.

Actual experiments with MCLR results are promising proof of concept for the effectiveness of the proposed read-out method. The utilized electrodes for the measurements presented in this thesis are patterned gold electrodes available to purchase commercially. The

advantage of the structure introduced in this thesis is that the designed interface can be configured to be interfaced with any range of capacitive transducer impedance, given the design method and the balancing array values.

The design details provided here, provide the firsthand knowledge for users from different areas than electrical engineering to make their own custom-designed data acquisition unit for their sensors or test the performance of a designed and fabricated transducer in a bridge scheme.

REFERENCES

[1] https://en.wikipedia.org/wiki/Algal_bloom

[2] G.A. Codd, Cyanobacterial toxins: Occurrence, properties and biological significance, Water Sci. Technol. vol. 32, pp. 149–156, 1995.

[3] G. A. Codd, L. F. Morrison, and J. S. Metcalf, "Cyanobacterial toxins: risk management for health protection," Toxicol. Appl. Pharmacol., vol. 203, no. 3, pp. 264–272, Mar. 2005.

[4] https://en.wikipedia.org/wiki/Microcystin-LR

[5] "Microcystis aeruginosa and the Effects of Microcystin-LR on Ecosystems and Human Health - microbewiki."[Online].Available:https://microbewiki.kenyon.edu/index.php/Microcystis_aeruginosa_and_the_Effects_of_Microcystin-LR_on_Ecosystems_and_Human_Health. [Accessed: 30-Jan-2018].

[6] B. G. Kotak, R. W. Zurawell, E. E. Prepas, and C. F. B. Holmes, "Microcystin-LR concentration in aquatic food web compartments from lakes of varying trophic status." Can. J. Fish. Aquat. Sci., 1996.

[7] "Cyanobacterial toxins: Microcystin-LR in Drinking-water." World Health Organization, 2003.

[8] Y. M. Kim, S. W. Oh, S. Y. Jeong, D. J. Pyo, and E. Y. Choi, "Development of an ultrarapid one-step fluorescence immunochromatographic assay system for the quantification of microcystins," *Environ. Sci. Technol.*, vol. 37, no. 9, pp. 1899–1904, May 2003.

[9] F. M. dos Anjos *et al.*, "Detection of harmful cyanobacteria and their toxins by both PCR amplification and LC-MS during a bloom event," *Toxicon*, vol. 48, no. 3, pp. 239–245, Sep. 2006.

[10] S. D. Soelberga, R. C. Stevensa, A. P. Limayeb, and C. E. Furlonga, "Surface Plasmon Resonance (SPR) Detection Using AntibodyLinked Magnetic Nanoparticles for Analyte Capture, Purification, Concentration and Signal Amplification," Anal Chem., vol. 81, no. 6, pp. 2357–2363

[11] G. Ertürk, B. Mattiasson, "Capacitive Biosensors and Molecularly Imprinted Electrodes," Sensors, vol. 17, pp. 390-411, 2017.

[12] S. Loyprasert, P. Thavarungkul, P. Asawatreratanakul, B. Wongkittisuksa, C. Limsakul, and P. Kanatharana, "Label-free capacitive immunosensor for microcystin-LR using self-assembled

thiourea monolayer incorporated with Ag nanoparticles on gold electrode," *Biosens. Bioelectron.*, vol. 24, no. 1, pp. 78–86, Sep. 2008.

[13] H. Jung, Y. W. Chang, G. Lee, S. Cho, M. Kang, J. Pyun, "A capacitive biosensor based on an interdigitated electrode with nanoislands," Analytica Chimica Acta, vol. 844, pp. 27–34, 2014.

[14] Z. Zou, J. Kai, M. J. Rust, J. Han, C. H. Ahn, "Functionalized nano interdigitated electrodes arrays on polymer with integrated microfluidics for direct bio-affinity sensing using impedimetric measurement," Sensors and Actuators A, vol. 136, pp. 518–526, 2007.

[15] K. V. Singh, A. M. Whited, Y. Ragineni, T. W. Barrett, J. King, R. Solanki, "3D nanogap interdigitated electrode array biosensors," Anal Bioanal Chem, vol. 397, pp. 1493–1502, 2010.

[16] H. Li, X. Liu, L. Li, X. Mu, R. Genov, A. J. Mason, " CMOS electrochemical instrumentation for biosensor microsystems: A review," *Sensors*, vol. 17, 2017.

[17] L.N. Sangolkar, S.S. Maske, T. Chakrabarti. "Methods for determining microcystins (peptide hepatotoxins) and microcystin-producing cyanobacteria," Water Res., vol. 40, pp. 3485–3496, 2006.

[18] Shen, P.P., Shi, Q., Hua, Z.C., Kong, F.X., Wang, Z.G., Zhuang, S.X., Chen, D.C., "Analysis of microcystins in cyanobacteria blooms and surface water samples from Meiliang bey, Taihu lake, China," Environ. Int., vol. 29, no. 5, pp. 641–647, 2003.

[19] Zhang, F., Yang, S.H., Kang, T.Y., Cha, G.S., Nam, H., Meyerhoff, M.E., "A rapid competative binding nonseperation enzyme immunoassay (NEEIA) test strip for microcystin-LR (MCLR) determination," Biosens. Bioelectron., vol. 22, no. 7, pp. 1419–1425, 2007.

[20] H.-C. Shi *et al.*, "Automated Online Optical Biosensing System for Continuous Real-Time Determination of Microcystin-LR with High Sensitivity and Specificity: Early Warning for Cyanotoxin Risk in Drinking Water Sources," *Environ. Sci. Technol.*, vol. 47, no. 9, pp. 4434–4441, May 2013.

[21] J. S. Daniels and N. Pourmand, "Label-Free Impedance Biosensors: Opportunities and Challenges," *Electroanalysis*, vol. 19, no. 12, pp. 1239–1257, May 2007.

[22] M. Labib, M. Hedström, M. Amin, B. Mattiasson, " A novel competitive glucose biosensor based on concanavalin A-labeled nanogold collids assembeled on polytyramine-modified gold electrode," Analytica Chimia Acta, vol. 659, pp.194-200, 2010.

[23] J. Rickert, W. Göpel, W. Beck, G. Jung, and P. Heiduschka, "A 'mixed' self-assembled monolayer for an impedimetric immunosensor," *Biosens. Bioelectron.*, vol. 11, no. 8, pp. 757–768, Jan. 1996.

[24] E. Katz and I. Willner, "Probing Biomolecular Interactions at Conductive and Semiconductive Surfaces by Impedance Spectroscopy: Routes to Impedimetric Immunosensors, DNA-Sensors, and Enzyme Biosensors," *Electroanalysis*, vol. 15, no. 11, pp. 913–947, Jul. 2003.

[25] A. J. Bard and L. R. Faulkner, Electrochemical Methods: Fundamentals and Applications. Wiley, 2000.

[26] C. Berggren, B. Bjarnason, and G. Johansson, "Capacitive Biosensors," *Electroanalysis*, vol. 13, no. 3, pp. 173–180, Mar. 2001.

[27] "Basic overview of the working principle of a potentiostat/galvanostat (PGSTAT) – Electrochemical cell setup," Autolab application note EC08, Dec. 2011.

[28] S. Loyprasert, M. Hedström, P. Thavarungkul, P. Kanatharana, B. Mattiasson " Sub-attomolar detection of cholera toxin using a label-free capacitive immunosensor," Biosensors and Bioelectronics, vol. 25, pp.1977-1983, 2010.

[29] M. Labib, M. Hedström, M. Amin, B. Mattiasson, " A novel competitive glucose biosensor based on concanavalin A-labeled nanogold collids assembeled on polytyramine-modified gold electrode," Analytica Chimia Acta, vol. 659, pp.194-200, 2010.

[30] C. Berggren, P. Stålhandske, J. Brundell, G. Johansson, A feasibility study of a capacitive biosensor for direct detection of DNA hybridization, Electroanalysis., vol. 11, pp. 156–160, 1999.

[31] R. Pradhan, A. Mitra, S. Das, Characterization of electrode/electrolyte interface of ECIS devices, Electroanalysis.vol. 24, pp. 2405–2414, 2012.

[32] W. Franks, I. Schenker, P. Schmutz, A. Hierlemann, "Impedance characterization and modeling of electrodes for biomedical applications," IEEE Trans. Biomed. Eng., vol. 52, pp. 1295–1302, 2005.

[33] X. Huang, R.W. Pascal, K. Chamberlain, C.J. Banks, M. Mowlem, H. Morgan, A miniature, high precision conductivity and temperature sensor system for ocean monitoring, IEEE Sens. J., vol. 11, pp. 3246–3252, 2011.

[34] C. Sontimuang, R. Suedee, F. Dickert, "Interdigitated capacitive biosensor based on molecularly imprinted polymer for rapid detection of Hev b1 latex allergen," Analytical Biochemistry, vol. 410, pp. 224–233, 2011.

[35] F. C. Carvalho, D. C. Martins, A. Santos, M. Roque-Barreira, P. R. Bueno, "Evaluating the equilibrium association constant between artinm lectin and myeloid leukemia cells by impedimetric and piezoelectric label free approaches," Biosensors, vol. 4, pp. 358-369, 2014.

[36] R. F. Taylor, I. G. Marenchic, and R. H. Spencer, "Antibody- and receptor-based biosensors for detection and process control," *Anal. Chim. Acta*, vol. 249, no. 1, pp. 67–70, Jan. 1991.

[37] K. Lee, S. Choi, J. O. Lee, J. Yoon, G. Cho, "CMOS capacitive biosensor with enhanced sensitivity for label-free dna detection," IEEE Int. Solid-State Circuts Conf. (ISSCC), pp. 120-122, Feb. 2012.

[38] J. Liu, M. M. Chisti, and X. Zeng, "General Signal Amplification Strategy for Nonfaradic Impedimetric Sensing: Trastuzumab Detection Employing a Peptide Immunosensor," *Anal. Chem.*, vol. 89, no. 7, pp. 4013–4020, Apr. 2017.

[39] A. Manickam, A. Chevalier, M. McDermott, A. D. Ellington, and A. Hassibi, "A CMOS Electrochemical Impedance Spectroscopy (EIS) Biosensor Array," *IEEE Trans. Biomed. Circuits Syst.*, vol. 4, no. 6, pp. 379–390, Dec. 2010.

[40] D. Huang, H. Leung, Reconstruction of drifting sensor responses based on papoulis–gerchberg method, IEEE Sens. J. 9 (2009) 595–604.

[41] K. C. Nguyen, " Quantitative analysis of COOH-terminated alkanethiol SAMs on gold nanoparticle surfaces," Adv. Nat. Sci.: Nanosci. Nanotechnol. Vol. 3, 045008 (5pp), 2012.

[42] M. l Riepla, V. M. Mirskya, I. Novotnyb,V. Tvarozekb, V. Rehacekb, O. S. Wolfbeis, "Optimization of capacitive affnity sensors: drift suppression and signal amplification," Analytica Chimica Acta, vol. 392, pp.77-84, 1999.

[43] O. Ceylan, G. K. Mishra, M. Yazici, R. C. Cakmakci, J. H. Niazi, A. Qureshi, Y. Gurbuz, "Development of hand-held point-of-care diagnostic device for detection of multiple cancer and cardiac disease biomarkers," IEEE Int. Symp. Circuits & Syestems (ISCAS), 2018.

[44] BL Theraja & AK Theraja, A text Book of "Electrical Technology." 2002.

[45] R. Downs, Bridge Measurement Systems, Precision Analog Applications Seminar, Section 5, Texas Instruments, 2006.

[46] S. C. Bera, S. Chattopadhyay, "A modified Schering bridge for measurement of dielectric parameters of a material and capacitance of a capacitive transducer," Measurement, vol. 33, pp. 3-7, 2003.

[47] M. Fonseca da Silva, A. Cruz Sera, "Study of the sensitivity in an automatic capacitance measurement system," IEEE Instrum. and Meas. Conf., pp. 329-334, 1997.

[48] P. Holmberg, "Automatic balancing of AC bridge circuits for capacitive sensor elements," IEEE Trans. on Instrum. and Meas., pp. 803-805, 1995.

[49] W. Q. Yang, "Aself balancing circuit to measure capacitance and loss conductance for industrial transducer aplications," IEEE Trans. on Instrum. and Meas., vol.45, No, 6, pp. 955-958, 1996.

[50] M. Tavakoli, R. Sarpeshkar, "An offset-canceling low-noise lock-in architechture for capacitive sensing," *IEEE J. Solid-State Circuits*., vol. 38, no. 2, pp. 244-253, Feb. 2003.

[51] B. Maundy, S. J. G. Gift, "Strain Guage Amplifier Circuits," *IEEE Trans. Instrum. Meas.*, vol. 62, no. 4, pp. 693–700, Apr. 2013.

[52] H. Sun, D. Fang, K. Jia, F. Maarouf, H. Qu, H. Xie, "A low-power low-noise dual-chopper amplifier for capacitive CMOS-MEMS accelerometers," IEEE Sensors J., vol. 11, no. 4, pp. 925-933, April. 2011.

[53] "DN1023 - Precision Matched Resistors Automatically Improve." [Online]. Available: http://studylib.net/doc/18055731/dn1023---precision-matched-resistors-automatically-improve. [Accessed: 30-Jan-2018].

[54] R. Pallas-Areny and J. G. Webster, "Common mode rejection ratio for cascaded differential amplifier stages," *IEEE Trans. Instrum. Meas.*, vol. 40, no. 4, pp. 677–681, Aug. 1991.

[55] J. Karki, "Fully-Differential Amplifiers." Texas Instruments, 2016.

[56] H. Zumbahlen, *Basic Linear Design*. Analog Devices, Incorporated, 2005.

[57] R. C. Gesteland, B. Howland, J. Y. Lettvin, and W. H. Pitts, "Comments on Microelectrodes," *Proc. IRE*, vol. 47, no. 11, pp. 1856–1862, Nov. 1959.

[58] "Noise Analysis In Operational Amplifier Circuits (Rev. B), slva043b - TI.com." [Online]. Available: http://www.ti.com/general/docs/litabsmultiplefilelist.tsp?literatureNumber=slva043b. [Accessed: 30-Jan-2018].

[59] T. J. Sobering, "Equivalent Noise Bandwidth," *Kans. State Univ. May*, 1991.

[60] R. Pintelon and J. Schoukens, "An improved sine-wave fitting procedure for characterizing data acquisition channels," IEEE Trans. Instrum. Meas., vol. 45, no. 2, pp. 588–593, Apr. 1996.

[61] P. M. Ramos, A. C. Serra, "A new sine-fitting algorithm for accurate amplitude and phase measurements in two channel acquisition systems," Measurement, vol. 41, pp. 135-143, 2008.

[62] A. Masi, A. Danisi, M. D. Castro, R. Losito, "Real-time high precision reading algorithm for the ironless inductive position sensor, " IEEE Trans. Nucl. Sci., vol. 60, no. 5, pp. 3661-3668, Oct. 2013.

[63] Standard for Digitizing Waveform Records, IEEE Std. 1057-1994, Dec. 1994.

[64] P. M. Ramos, F. M. Janeiro, M. Tlemçani, A. C. Serra, "Recent developments on impedance measurements with DSP-based ellipse-fitting algorithms,"IEEE Trans. Instrum. Meas., vol. 58, no.5, pp. 1680–1689, May. 2009.

[65] P. M. Ramos, F. M. Janeiro, T. Radil, "Comparison of impedance measurement in a DSP using ellipse-fit and seven-parameter sine-fit algorithms," Measurement, vol. 42, pp. 1370-1379, 2009.

[66] T. Andersson, P. Händel, "IEEE Standard 1057, Cramér-Rao bound and the parsimony principle," IEEE Trans. Instrum. Meas., vol. 55, no.1, pp. 44–53, Feb. 2006.

[67] M. Martino, R. Losito, A. Masi, "Analytical metrological characterization of the three-parameter sine fit algorithm," ISA Transactions, vol. 51, pp. 262-270, 2012.

[68] A. H-S. Ang, W. H. Tang, "Probability Concepts in Engineering: Emphasis on Applications to Civil and Environmental Engineering," 2nd edition, John Wiley & Sons, Inc. 2007.

[69] T. Piasecki, "Fast impedance measurements at very low frequencies using curve fitting algorithms," Meas. Sci. Technol. vol. 26, 2015.

[70] F. Algeria, A. C. Serra, "Gaussian jitter induced bias of sine wave amplitude estimation using three parameter sine fitting,"IEEE Trans. Instrum. Meas., vol. 59, no.9, pp. 2328–2333, Sep. 2010.